Consideration of Wall Reflection and Diffraction in the Room Acoustic Prediction Using the Phased Beam Tracing Method

Jeong, Cheol-Ho; Ih, Jeong-Guon; Rindel, Jens Holger

Publication date:
2007

Document Version
Publisher's PDF, also known as Version of record

Citation (APA):
Jeong, C-H., Ih, J-G., & Rindel, J. H. (2007). *Consideration of Wall Reflection and Diffraction in the Room Acoustic Prediction Using the Phased Beam Tracing Method*.

박사학위논문

Doctoral Thesis

위상 빔 추적법을 이용한 실내 음향 예측에 있어서 벽면 반사와 회절의 고려

Consideration of Wall Reflection and Diffraction in the Room Acoustic Prediction Using the Phased Beam Tracing Method

정 철 호(鄭 哲 浩 Jeong, Cheol-Ho)
기계항공시스템학부 기계공학전공
School of Mechanical, Aerospace & Systems Engineering
Division of Mechanical Engineering

한 국 과 학 기 술 원
Korea Advanced Institute of Science and Technology

2007

위상 빔 추적법을 이용한 실내 음향 예측에 있어서 벽면 반사와 회절의 고려

Consideration of Wall Reflection and Diffraction in the Room Acoustic Prediction Using the Phased Beam Tracing Method

Consideration of Wall Reflection and Diffraction in the Room Acoustic Prediction Using the Phased Beam Tracing Method

Advisor: Professor Jeong–Guon Ih
Co-advisor: Professor Jens H. Rindel

by

Cheol-Ho Jeong

School of Mechanical, Aerospace & Systems Engineering
Division of Mechanical Engineering
Korea Advanced Institute of Science and Technology

A thesis submitted to the faculty of the Korea Advanced Institute of Science and Technology in partial fulfillment of the requirements for the degree of Doctor of Philosophy in the School of Mechanical, Aerospace & Systems Engineering, Division of Mechanical Engineering.

Daejeon, Korea
2007. 5. 21.
Approved by

Professor Jeong–Guon Ih
Major Advisor

위상 빔 추적법을 이용한 실내 음향 예측에 있어서 벽면 반사와 회절의 고려

정철호

위 논문은 한국과학기술원 박사학위논문으로 학위논문심사위원회에서 심사 통과하였음.

2007년 5월 21일

심사위원장 이정권 (인)

심사위원 김양한 (인)

심사위원 박영진 (인)

심사위원 한찬훈 (인)

심사위원 Jens H. Rindel (인)

DME 20025281

정 철 호. Jeong, Cheol-Ho. Consideration of Wall Reflection and Diffraction in the Room Acoustic Prediction Using the Phased Beam Tracing Method. 위상 빔 추적법을 이용한 실내 음향 예측에 있어서 벽면 반사와 회절의 고려. School of Mechanical, Aerospace & Systems Engineering, Division of Mechanical Engineering. 2007. 158p. Advisor Prof. Jeong–Guon Ih. Co-advisor: Prof. Jens H. Rindel.

Text in English

ABSTRACT

The geometrical acoustics methods have been used to simulate the acoustics of rooms at high frequencies whereas the wave based methods have been devoted to calculate the low frequency response. The modified method, so called phased geometrical acoustics technique, was suggested for the extension of the applicability of the geometrical methods to mid frequency. Several studies on this method have demonstrated a good possibility to analyze the sound field in an enclosure at mid frequency. In this study, further considerations on wall reflection and diffraction have been investigated. The main suggestions are the use of approximated reflection coefficient and the integration with the theory of diffraction. This study aimed to improve the precision of the present method in mid frequency range and extend the applicability to the low frequency below Schroeder cutoff frequency. Because this method is originated from the geometrical acoustics, the wave-particle duality can be discussed by comparing with result from modal method.

The calculation parameters were thoroughly investigated. The number of beams and the frequency resolution were proved to be the most important parameters in the analysis and consequently the guidelines were suggested for these parameters. The approximate angle-dependent/independent reflection coefficients were tested. The angle dependent reflection coefficient can take the angle dependence of the incident wave into account as well as the size effect of the surface. Also, the merit of representing the negative real part was discussed. The PBTM result shows a good agreement with the measurement especially in the early part of impulse response and at mid frequency. The new method of binaural simulation for the PBTM was suggested. The peculiar feature of frequency domain calculation of the PBTM gives advantages in the binaural simulation. Particularity in the early part of the impulse response at mid frequency, the binaural simulation result shows an excellent correspondence with the measurement in the application of a conference room.

The diffraction phenomenon was incorporated into the PBTM based on the uniform theory of diffraction for the low to mid frequency simulation. The diffraction of edge, which is the topmost problem in an enclosed space, was tested. The simulated results by combining the PBTM with UTD agreed well with the previous research. Besides, the measurement in an anechoic chamber agreed better with the combined method than the ordinary PBTM in 125 Hz octave band. The simulation of an enclosure having a diffracting edge validates the improvement by comparing with the BEM result. One actual concert hall was tested to simulate the diffraction at receivers under a balcony

According to the result of PBTM, the PBTM can be a mid-frequency method bridging the gap between the low frequency method and high frequency method for the acoustic simulation of an enclosure as a unified approach. Furthermore, when a proper technique such as uniform theory of diffraction is integrated into, the present method can even deal with the low to mid frequency range, which has been considered as the typical territory for the wave based methods for a long time. The capability of calculating a room transfer function enables this method to be used in the analysis, design, diagnosis and refinement of a space. Because the applicable frequency range was extended to low-to-mid frequency, the small-to-medium sized room can be dealt with, vise versa. Therefore a small space like vehicle cabin and aircraft cabin can be dealt with by the present method as well as a large performance spaces.

CONTENTS

NOMENCLATURE

a	travel distance of a beam
c_o	speed of sound in air
D	diffraction coefficient
e	characteristic length
f_c	Schroeder cutoff frequency
j	imaginary number
k	wave number in a lossless medium
m	air attenuation factor
n	angle factor of an edge
$\overrightarrow{N}$	normal vector
N_{beam}	number of beams
N_p	number of poles in a transfer function
N_{refl}	reflection order (number of reflections)
N_z^+, N_z^-,	number of non-minimum/minimum phase zeros
p	acoustic pressure
p^d	diffracted pressure
r, r_i^θ, r_d^θ	reflection coefficient
R	resistance
$\overrightarrow{R_d}$	direction of incidence
$\overrightarrow{R_d'}$	direction of reflection
RT, T_{30}, T_{20}	reverberation time
S	surface area
T_{tot}	total time length of the impulse response
X	reactance
V	volume of an enclosed room
Z_r	radiation impedance of a surface

Z_w, ζ	surface impedance, normalized surface impedance
α_θ	absorption coefficient for the incidence angle of θ
α_{rand}	random incidence absorption coefficient
β	phase of surface impedance
β_o	angle between the incidence ray and the tangent to the edge
$\overline{\delta f_p}$, $\overline{\delta f_z}$	average frequency spacing of poles and zeros
Δf	frequency resolution, frequency spacing
ϕ	angle of receiver location
ϕ'	angle of source location
θ	angle of incidence
ρ	density of air, distance form the receiver to diffraction point
ρ'	distance form the source to diffraction point

LIST OF TABLES

LIST OF FIGURES

Fig. 2.9. Snell's law in two-dimensional case. $\vec{N}$ denotes the outer normal vector of the surface and $\vec{N}_I$ and $\vec{N}_R$ the outer normal vector of the incident ray and reflected ray, respectively. θ_i and θ_r mean the angle of incidence and angle of reflection, respectively. $\vec{R}_d$ and $\vec{R}_d^{'}$ represents the direction of incident and reflected ray, respectively.

Fig. 2.10. Reflection of a beam in two-dimensional case. $\vec{N}_1$ and $\vec{N}_2$ mean the outer normal vectors of the incident two-dimensional beam and $\vec{N}_1^{'}$ and $\vec{N}_2^{'}$ the outer normal vectors of the reflected two-dimensional beam. $\vec{R}_1$ and $\vec{R}_2$ represent the edge vectors of the incident beam and $\vec{R}_1^{'}$ and $\vec{R}_2^{'}$ the edge vectors of the reflected beam.

Fig. 2.11. Arrival of a ray at the observation region. The receiver can be detected when $A^2 - B + R^2 \geq 0$, where $A = \vec{v} \cdot \vec{w}$ and $B = |w|^2$. The $\vec{P}_s$ and $\vec{P}_r$ denote the source and receiver position, respectively. $\vec{v}$ is the ray direction and $\vec{w}$ the vector between the reflection point and the sphere center. R denotes the radius of the curvature of the sphere.

Fig. 2.12. Detection algorithm for triangular beam tracing method. $\vec{R}_1$ and $\vec{R}_2$ denote the vectors between the source image source and the receiver 1 and 2, respectively. The shaded region represents the triangular beam and $\vec{N}_1$ and $\vec{N}_2$ denote the outer normal vectors of the beam. In order to be detected by the beam, angles between $\vec{R}$ and the outer normal vectors should be obtuse. In the case of receiver 1, all the angles are obtuse. In the case of receiver 2, θ_3, the angle between $\vec{R}_2$ and $\vec{N}_2$ becomes acute. Then, the receiver 2 cannot be detected.

Fig. 2.13. Test room model. ●, Source; ▲, observer. Surface properties are listed in Table 2.3.

Fig. 2.14. Number of detected beam as a function of number of beams. —■—, Direct sound; —●—, 1st reflection; —▲—, 2nd reflection; —▼—, 3rd reflection; —◆—, 4th reflection; —◀—, 10th reflection.

Fig. 2.15. Test room geometry. ●, Source; ▼, observer. Wall properties are listed in Table 2.3.

Fig. 2.16. Steady-state transfer functions for two different frequency resolutions, Δf:
——,Δf=1 Hz; ••••,Δf=0.1 Hz.

Fig. 2.17. A comparison of zoomed transfer functions for two different frequency resolutions, Δf: —○—, Δf=1 Hz; – – –,Δf=0.1 Hz. (a) Real and imaginary parts, (b) magnitude and phase.

Fig. 2.18. A comparison of impulse responses varying the frequency resolution: ——, Δf=1 Hz; – – –,Δf=0.1 Hz.

Fig. 2.19. A comparison of decay curves. ———, Δ*f*=1 Hz; - - - -, Δ*f*=0.1 Hz.
Fig. 2.20. Relative error as a function of the normalized time length.
Fig. 2.21. Comparisons of transfer functions: ———, Original Δ*f*=1 Hz; — — —, interpolated. (a) Linear interpolation, (b) cubic spline interpolation.
Fig. 2.22. Comparisons of impulse responses: ———, Original Δ*f*=1 Hz; — — —, interpolated. (a) Linear interpolation, (b) cubic spline interpolation.
Fig. 2.23. Comparisons of transfer functions: ———, Original Δ*f*=2 Hz; ·······, interpolated. (a) Linear interpolation, (b) cubic spline interpolation.
Fig. 2.24. Comparisons of impulse responses: ———, original Δ*f*=2 Hz; ·······, interpolated. (a) Linear interpolation, (b) cubic spline interpolation. In Fig. 2.24(a), two curves are perfectly overlapped.
Fig. 2.25. Convergence check for the steady-state pressure. (a) *f*=90 Hz, (b) *f*=1000 Hz.
Fig. 3.1. Normalized radiation impedance for a panel of 100 m^2 in area. —□—, 125 Hz; —○—, 250 Hz; —△—, 500 Hz; —▽—, 1 kHz; —◁—, 2 kHz; —◇—, 4 kHz.
Fig. 3.2. Angle-dependent reflection coefficient for a panel of 100 m^2 in area. —□—, 125 Hz; —○—, 250 Hz; —△—, 500 Hz; —▽—, 1 kHz; —◇—, 2 kHz; —◁—, 4 kHz.
Fig. 3.3. The values in the parenthesis in Eq. (3.1.9). ———, Total; — — —, first term; — • —, second term; — • • —, third term.
Fig. 3.4. A Comparison of absorption coefficient. ———, Eq. (3.1.9); — — —, Eq. (3.1.10); ••••, Eq. (3.1.11).
Fig. 3.5. A comparison of Angle of zero crossing as a function of frequency. ———, Eq. (3.1.8); — — —, Eq. (3.1.12).
Fig. 3.6. Measured surface impedance and corresponding absorption coefficient. (a) Real part of surface impedance, (b) imaginary part of surface impedance, (c) calculated absorption coefficient.
Fig. 3.7. A comparison of measured and calculated reflection coefficients as a function of incidence angle (200 Hz). — — —, Real part of directly measured *r*; — · · —, imaginary part of directly measured *r*; —■—, r_θ^i; ———, r_θ^d. The test sample was 20 mm thick PU form (Z_w = 511-2881*j*, α_s= 0.15 at 200 Hz).
Fig. 3.8. Geometry and dimensions of the test room. Acoustic properties of surfaces are specified in Table 3.2.
Fig. 3.9. A comparison of measured and calculated pressure impulse responses (R1). — — —, Measurement; ———, calculated by PBTM. (a), (b) 125 Hz; (c), (d) 250 Hz; (e), (f) 500 Hz; (g), (h) 1 kHz. (a), (c), (e), (g) Use of r_θ^i; (b), (d), (f), (h) use of r_θ^d.
Fig. 3.10. A comparison of measured and calculated energy impulse responses at

1. INTRODUCTION

1.1. Motivation and Historical Background

For several decades, the geometrical acoustics techniques, such as ray/beam tracing method (RTM [1-5]/BTM [6,7]) and image source method (ISM) [8-10], have been widely used to predict the acoustic characteristics of enclosed spaces. The first attempt to predict two-dimensional time and space distribution of the early reflected sound using digital computer was performed by Krokstad, et al. [1]. Then, an algorithm for ray tracing in three-dimensional space was presented to economize both calculation time and computer memory space [2,3]. Schroeder simulated the reverberant process in a room and discussed the sound transmission for two dimensional spaces [4]. The averaged energy history for 300 rays was found to calculate the reverberation time. Rindel emphasized the scattering, diffusion and auralization [5] and summarized the room acoustical computer models [11]. The cone tracing, suggested by Maercke and Martin [6], has a problem of overlapping between the cones and inefficient representation of the spherical wavefront. The triangular beam tracing method [7] was firstly introduced to account for the diffusion based on the radiant exchange model.

Allen and Berkley discussed the theoretical and practical use of image technique for simulating on a digital computer by using the image source method [8]. After several years, the image model was extended to arbitrary polyhedra with any number of sides [9]. The image model was used to provide insight into the acoustical properties of different hall geometry. Lee and Lee suggested the effective image source algorithm to save the computer memory space [10]. Subsequently, hybrid methods have been suggested by combining the best features of both methods. The efficient way to find the valid image sources is to trace rays back from the receiver and note the surfaces they hit [12]. Another suggestion for hybrid method is to employ the image/secondary source method and late ray method for early part and late part of the impulse response, respectively [13,14].

These methods are very effective at high frequencies and their computational cost is very low compared to wave based methods such as finite element method (FEM), boundary element method (BEM) and finite difference method (FDM). However, in a practical application of RTM/BTM to the low and medium frequency ranges, big discrepancies between simulation and measurement have been observed. Usually, the low frequency region can be analyzed by using the modal techniques like FEM, BEM, or FDM, but the mid frequency range still needs an appropriate method for the analysis and design.

Returning to the geometrical acoustics methods, it should be noted that they are all high frequency *energy* methods by summing the energies or contributions of the ray/beam/image source. The energy methods such as geometrical acoustics methods, the statistical energy method (SEA) [15,16] and the power flow method (PFA) [17] are reliable mainly in the high frequency range. They have two common features. First, they do not solve the second order partial differential equation of wave equation to simulate the sound field for three-dimensional space or vibration response in one-dimensional and two-dimensional structure. The aforementioned methods adopt the simplified equations such as power balance equation (energy conservation equation) in SEA and power flow formulation (heat conduction equation) in PFA. In the geometrical acoustics, it is principally assumed that the wave propagation can be described by the travel of a particle along the ray paths, which can be determined entirely by the geometrical shape of an enclosure. The sound field of a room is viewed in terms of particle property of sound at high frequency by the geometrical acoustics method. The discussion regarding the relationship between the wave and particle description of the sound can be best summarized by quoting the following extracts from Lyon and DeJong [15]: “we must emphasize that it is always possible, *at least in principle*, to arrive at the same conclusions by either the wave or particle approach”. To this, the following quote from Fahy [18] can be added: “just how pure standing wave field can be created in any elastic system, by reflection of waves from boundaries of arbitrary geometry, is something a mystery” According to those quotes, the geometrical searching technique, which mainly emphasize the principal property of a particle, can estimate a low frequency response. In contrast to the high frequency method, the wave based methods such as BEM, FEM and FDM emphasize the wave property more. The criteria which demarcate the applicability of both methods can be the frequency such as Schroeder cutoff frequency [19] or the ratio between the wavelength and the dimension of a space. Generally speaking, neither a sound field of a small room nor the low frequency prediction is a proper target of the geometrical acoustics method. But still there is a good possibility to analyze the low to mid frequency or small to medium sized room acoustic response by adopting the geometrical acoustics.

The second common feature is that energy quantities are the primary variables of interest. They deal with the energy quantities such as energy density, power flux, and intensity. This feature should be modified, because a reliable prediction of the sound field cannot be achieved by dealing with energy quantity, particularly at low to mid frequency. The diffraction and interference are predominant in the low frequency range, where wave nature of the sound rules strongly. The diffraction, the distortion of wave front or the spread out of sound beyond an aperture cannot be inherently described by the straightly propagating ray/beam. In addition, the interference such as standing wave cannot be recounted without phase information. As frequency gets higher, the phase information becomes of less importance and gets complicated due to the strong overlap between the adjacent modes and increasing uncertainties. Generally, the diffraction becomes negligible when the wavelength is smaller than the dimension of a space. Consequently at high frequencies over the Schroeder cutoff frequency, the sound field can be approached in a statistical manner with random phase. Concerning other wave phenomena such as reflection and scattering, which are of importance for all frequency and relatively high frequency, respectively, they can be quite reasonably represented by the particle property. Another source of the inaccuracy at low-to-mid frequency is the statistically-determined and frequency-averaged material properties of the surfaces, e.g., absorption coefficients. Instead of absorption coefficient, the complex valued pressure reflection coefficient can greatly improve the precision of the simulation. Pressure reflection coefficient can be easily calculated from the measured surface impedance, if the data are available. For a practical purpose, an approximate reflection coefficient can be utilized in the design/refinement stage.

One suggestion to overcome the inherent problems of the geometrical acoustics method is to include the phase information in the ray/beam/image source, because the main faults at low frequency predicted by the geometrical acoustics methods are due to the loss of phase information and wave characteristics. The modified geometrical method can simulate the interference phenomenon. Also, phase information can introduce the concept of mode in the geometrical acoustics. The simulation result with phase can be improved for the frequency range where the modes are distinguishable and phase information is essential, i.e. around Schroeder cutoff frequency. In addition, the other advantage of retaining the phase information can be obtained in terms of the target function of the simulation. Instead of an energy reflectogram, a pressure impulse response or a frequency response function can be primarily calculated.

Accordingly, the complex numbers such as pressure reflection coefficient or complex wave number are needed in the simulation rather than the absorption coefficient and real valued wavenumber. They represent the acoustical properties of the surfaces, and the phase change during the propagation and the attenuation in the air, respectively. Pressure reflection coefficient characterizes not only the magnitude change at the surface, but also the phase shift. When the frequency-dependent reflection coefficient is involved instead of frequency-averaged absorption coefficient in a band, the detailed characteristics in the frequency domain can be also thoroughly examined. The complex wavenumber implies the air attenuation factor as an imaginary part, so as to take the attenuation due to air absorption into account.

There are two types of geometrical acoustics which utilize the phase information. The first method is the phased ray/beam tracing method and the other is the phased image source method. The first attempt to introduce phase in the ray tracing method has been made by Geest and Patzold [20]. They include the phase shift at the wall, but the way how they include the phase information is not explained both literally and mathematically. They compared the calculated frequency response function with BEM results. The simulation results showed excellent agreement with those of BEM even below 50 Hz, which is considered to be quite low frequency range for geometrical acoustics. It is the pioneering work to demonstrate a good possibility of using the modified geometrical acoustics for the low frequency prediction. An extended study on this matter had been carried out by Shin and Ih including a study on the diffraction effect [21]. The precision of the method in the low and high frequency limits was compared with the boundary element method and measurement. Lam has found that the geometrical acoustics method which incorporates the complex sound pressure propagation and reflection can provide accurate prediction [22]. Moreover, he demonstrated the numerical models in terms of volume scattering, disproportionate geometry and the types of reflection coefficient. Wareing and Hodgson suggested the modeling technique for the multilayered surface in the beam tracing with phase [23]. A transfer matrix approach was validated by comparing with measurement. In the calculation of sound pressure, they also investigated the calculation parameters such as number of beams, reflection order and the frequency resolution.

For phased image source method, Dance, et al. attempted to model the interference effect in the factory including phase [24]. The basis of this model is that interference can take place between direct and reflected sound or between two reflected sounds. Although they neglect the phase change upon the reflection at the wall, they simulated the sound pressure distribution in the factory satisfactorily. Suh and Nelson tried to simulate the impulse response and FRF in the room and the result showed remarkable agreement with measured data [25]. Improvement was achieved by applying the measured complex impedance to the reflection at the wall. Also in this result, the overestimation of the conventional energy method can be found. The latest research about phased ISM was made by Zeng, et al. [26]. Although they utilized the absorption coefficient, which means that phase change was not included in the analysis at a reflection, the results showed an appreciable difference with the RTM results. The predicted reverberation time and sound pressure level agree better with measured data than the RTM.

However, the results of the ray/beam tracing method mainly rely greatly on the number of rays (or beams) and receiver size (only for ray tracing). There were some previous works on the determination of receiver size for ray tracing [27-29]. Lenhert suggested the radius of a spherical receiver considering the maximum length of the ray path and the number of emitted rays [27]. Instead of the length of the ray path, the size of the space was taken in to account to determine the receiver volume by Yang and Shield [28]. Recently Zeng, et al.

made a formula for the radius of the receiver in consideration of both source to receiver distance and the space volume [29]. In order to avoid the receiver size dependence, the most sophisticated and well-known commercial software using the geometrical acoustics, ODEON [30], utilizes the hybrid method employing the image source method applied to the early reflections, while it adopts the late ray method for late reflections to get a reliable result.

Instead of ray, beams can densely cover the space to describe the propagation of spherical wave. While infinitesimally thin rays and receivers with finite volume are used to simulate the room in the ray tracing method, the beams with diverging cross section and point receivers are employed. The cone tracing was suggested by Maercke and Martin [6] and the triangular beam tracing method was firstly introduced by Lewers [7]. Further development was performed by many researchers such as Farina [31], Stephenson [32], Shin and Ih [21], Drumm and Lam [33], Campo, et al. [34], and Funkhouser, et al. [35]. The split-up algorithm for the beam was taken up in the recent researches to avoid the scanning error [33-35]. In the conventional beam tracing method, beams carry the energy quantity. Emitted beam possesses some amount of energy at the starting point and during the propagation within the enclosure, it loses a part of initial energy owing to the air attenuation and the absorption at the hitting surfaces. As a result, energy reflectogram (or echogram) for a frequency band (usually for octave band or 1/3 octave band) can be found using the arrival time of a beam and the energy at that time at the observer point.

In this study, the triangular beam tracing method has been employed to avoid the use of complicated weighting functions for resolving the overlapping problem of cone tracing method [6]. By adopting the phased beam tracing method (PBTM), pressure reflectogram can be calculated. From the pressure reflectogram for a frequency, the steady-state response can be obtained simply by the summation of direct sound and successive transient components. If the steady-state pressures are calculated for all frequencies within the frequency range of interest, steady-state transfer function is constructed. Finally, one can use the steady-state transfer function to obtain an impulse response by taking the inverse Fourier transform.

For the extension of the applicable range, the diffraction effect should be accounted for. The diffraction can not be counted in the ordinary PBTM, therefore a proper theory which can be incorporated into the PBTM is needed. The diffraction problem of an infinite wedge irradiated by a point source was studied by Biot and Tolstoy [36] by using normal modes. It was extended by Medwin to apply the Biot-Tolstoy solution to underwater problem and noise barrier by the concept of secondary edge source [37]. The key is the analytical directivity functions for the edge sources. The Kirchhoff diffraction approximation based on Huygen's principle has been introduced to represent the field diffracted through an aperture as an integral over the aperture [38]. However it has been reported by several researchers that it is compute-intensive [39] and leads to large errors at high frequencies [40-42]. The geometrical theory of diffraction (GTD) was initially suggested by Keller [43] to account for the diffraction using in the geometrical optics field. His main idea was to introduce new diffracted ray at the corners, edges, and vertices of surfaces with an appropriate diffraction coefficient. Then the calculated diffraction field is added to the geometrical acoustics field. This concept from geometrical optics has been successfully adopted for geometrical acoustics [41,44]. It has been known that the GTD is generally superior to Kirchhoff diffraction theory in both accuracy [45-47] and efficiency at high frequencies [41,43]. The shortcoming of above mentioned sharp edge problem was corrected by the GTD. However, it fails at near shadow and reflection boundaries due to singularity in the diffraction coefficient. Therefore the uniform theory of diffraction (UTD) [48] was suggested by Kouyoumjian and Pathak to remove the singularity. This theory shows a considerable improvement in both accuracy and efficiency over the earlier methods. In this paper, the UTD integrated into the PBTM was tested for the simulation of step discontinuity and wedge diffraction in an enclosure.

In addition to the simulation of a transfer function, an impulse response and the calculation of several acoustic parameters, the binaural simulation for the PBTM technique was suggested. Binaural simulation is a method of making binaural signals at receiver's both ears in non-existing spaces by means of a computer model. The listening impression related to the psychoacoustics becomes more important for the acoustical design of an enclosed space. In most cases, the geometrical acoustics techniques such as the mirror image source method, the ray racing method and hybrid method have been employed. Although it is not possible to simulate the actual sound field accurately by using the geometrical acoustics methods, the previous works have been successful and some of them have been already commercialized. The great advantage of geometrical acoustics technique compared to modal method is the simple and easy decomposition of each reflection toward the receiver point. Also, the limited spatial resolution of human auditory system can make the binaural simulation successful by means of geometrical acoustics method. Once the distribution of image sources is quantized, the binaural simulation can be carried out by the convolution with the head related transfer function (HRTF) of a listener. The frequency domain calculation of the PBTM facilitates the binaural simulation because the convolution with HRTF is a simple multiplication in the frequency domain. The convolution is carried out for each arriving beam, one by one, and convolved transfer functions are summed into a final transfer function. The binaural signals can be obtained by the inverse Fourier transform for both left/right ear transfer functions convolved with HRTF.

Finally, the PBTM, which is the representative of the particle property, was compared with the BEM, which is the exemplary method of wave property. It can be thought that the geometrical acoustics field can be considered as the leading term of the series expansion of the solution for the wave equation whereas the higher order terms describe the wave phenomena. The high frequency response or the weakly reverberant field can be interpreted by adopting the geometrical acoustics method successfully because the higher order terms become negligible. For the simplest geometry such as rectangular shaped room, the PBTM shows a good agreement with the BEM. For a complicated-shaped room, in which the wave nature of the sound is more distinguished, the PBTM shows a discrepancy with BEM. In this case, the higher order terms such as diffraction and scattering are inevitably needed. The monopole and dipole terms in the Kirchhoff-Helmholtz integral equation were compared separately with the PBTM and it was concluded that the dipole effect is corresponding to the PBTM from the mathematical and physical viewpoints. Usually, the dipole effect overwhelms the monopole radiation in an enclosure.

The ultimate purpose of this study was to develop a unified approach to predict the three-dimensional sound field by using the phased beam tracing method for the whole audible frequency. The suggested method is based on the particle property of the sound and extended to the lower frequency by adding wave nature of the sound. The prediction of the three-dimensional sound field implies the calculation of a transfer function, an impulse response and acoustic parameters as well as the binaural simulation. The applicability can be extended to the medium frequency quite successfully and a possibility to be a low frequency predictor for the simple sound field was validated when the diffraction is properly implemented.

1.2. Overview of the Thesis Structure

The following describes the contents of each chapter briefly. In Chapter 2, the PBTM was explained in detail. In the Chapter 2.1, the necessity of the phase information was revisited for one-dimensional vibrating structure. The phase information in the ray can construct the velocity distribution completely while the RTM without phase shows the spatially averaged distribution. In one-dimensional field, the RTM with phase agrees perfectly with the exact solution even at low frequency, because the ray can completely describe the propagating plane wave in a bar. The summation of propagating components of Ae^{-jkx} and Be^{jkx}, and evanescent wave of Ae^{-kx}, agrees well with the exact solution even though any mathematical description such as wave equation was not employed at all. This one-dimensional phased method demonstrates a hopeful possibility for low frequency simulation. Calculation parameters in the PBTM such as the number of beams, frequency resolution, reflection order, sampling frequency and temporal resolution were investigated in Chapter 2.3. Especially the importance of frequency resolution was accentuated in terms of the number of non-minimum phase zeros.

In Chapter 3, practical considerations on the reflection coefficient and the test examples are discussed. The pressure reflection coefficient, which plays the essential role in the PBTM, was examined in Chapter 3.1. An approximate treatment of reflection coefficient, e.g. angle-dependent/independent reflection coefficient, was tested in the PBTM and showed a good agreement with the measurement especially in the early part of impulse response and at mid frequency. The condition for real part of the angle-dependent reflection coefficient was also studied. The transfer function, the impulse response and the calculated acoustic parameters by the PBTM have been compared with the measurement and other methods in Chapter 3.1. In Chapter 3.3, the new method of binaural simulation for the PBTM was suggested. The PBTM is different from the conventional geometrical acoustics method in some ways. The unusual feature of frequency domain calculation of the PBTM gives advantages in the binaural simulation. The convolution with the HRTF which is essential in the auralization process is a simple multiplication. Particularity in the early part of the impulse response, the PBTM result shows a great correspondence with the measurement in the application of a conference room. As well as the high frequency response, the mid frequency response was acceptable whereas the low frequency response shows a discrepancy with measurement.

In Chapter 4, the diffraction phenomenon was accounted for in the PBTM by the aid of the UTD. The UTD is the simple and effective theory in accounting for the diffraction phenomenon. The UTD started from the hypothesis that the geometrical optics field corresponds to the leading term of Luneberg Kline series for the reduced wave equation or Maxwell's equation. The higher order terms account for diffraction and other wave phenomena. The diffraction of wedge, which is the topmost problem in an enclosed space, was tested. The simulated results by combining the PBTM with UTD agree well with the previous research. Besides, the measurement revealed a good possibility to apply this present method to the low frequency range in considering the diffraction as well as the interference. This integration between the UTD and PBTM can be a fast and efficient low frequency predictor in the architectural acoustics field by considering the single and double diffraction.

In Chapter 5, the overall conclusion was drawn that the PBTM can be a mid-frequency method bridging the gap between the modal method and geometrical acoustics method for the acoustic simulation of an enclosure as a unified approach. Furthermore, when a proper technique such as uniform theory of diffraction is integrated into, the present method can even deal with the low frequency range, which has been considered as the typical territory for the wave based methods for a long time. The capability of calculating the room transfer function enables this method to be used in the analysis, design, diagnosis and refinement of a space. The extension of application to low to mid frequency means that the technique can be adopted for the simulation of a small to medium sized room. As well as the large performance space such as concert hall and theater, the smaller space like vehicle cabin and aircraft cabin can be dealt with by the present method.

1.3. Problem Specification

This study generally deals with the *mid frequency* acoustic simulations in an enclosed space by the phased beam tracing method. The phased beam tracing method, which is originated from the geometrical acoustics method, has been employed in order to explain the wave nature of the sound at mid frequencies. At mid frequencies, where the interference is the strongest wave phenomenon, several approaches have been tried. The modal methods become too expensive due to small discretization of a space. High frequency energy methods are generally not satisfactory due to the neglect of phase information and interference effect. The fuzzy behavior of mid frequency range can not be solved by any one of wave-particle duality of the sound. For this reason, the PBTM, hybrid approach combining the wave nature and particle property, was suggested. The major aim of this study is to improve the precision of the PBTM simulation at mid frequency and to extend the application range to lower frequency. Two main suggestions in this study are the use of a practical reflection coefficient for explaining the interference and incorporation with the theory of diffraction.

Many room models were demonstrated to validate this method as a mid frequency predictor by retaining phase. An appropriate theory of diffraction was selected and incorporated into the present method. The combined method was validated and tested in practice. Finally, the wave-particle duality of the sound, which is viewed by either the phased beam tracing or the boundary element method, was comprehensively discussed from the various viewpoints.

2. A REVIEW OF THE PHASED TRACING METHOD

The geometrical acoustics techniques including phase is referred to as the phased geometrical techniques. One method is the phased ray/beam tracing method and the other is the phased image source method. The first attempt to introduce phase in the ray tracing method has been made by Geest and Patzold [20,49]. They include the phase shift at the wall and compared the calculated frequency response function with BEM results. The simulation results showed excellent agreement with those of BEM even below 50 Hz, which is considered to be quite low frequency range for geometrical acoustics. It is the pioneering work to demonstrate a good possibility of using the modified geometrical acoustics for the low frequency prediction. An extended study on this matter had been carried out by Shin and Ih including a study on the diffraction effect [21]. The precision of the method in the low and high frequency limits was compared with the boundary element method and measurement. Lam has found that the geometrical acoustics method which incorporates the complex sound pressure propagation and reflection can provide accurate prediction [22]. Moreover, he demonstrated the numerical models in terms of volume scattering [50], disproportionate geometry and the types of reflection coefficient. Wareing and Hodgson suggested the modeling technique for the multilayered surface in the beam tracing with phase [23]. A transfer matrix approach was validated by comparing with measurement. In the calculation of sound pressure, they also investigated the calculation parameters such as number of beams, reflection order and the frequency resolution.

For phased image source method, Dance, et al. attempted to model the interference effect in the factory including phase [24]. The basis of this model is that interference can take place between direct and reflected sound or between two reflected sounds. Although they neglect the phase change upon the reflection at the wall, the simulated sound pressure distribution in the factory showed a good correspondence with measurement. Suh and Nelson tried to simulate the impulse response and FRF in the room and the result showed remarkable agreement with measured data [25]. Improvement was achieved by applying the measured complex impedance to the reflection at the wall. Also in this result, the overestimation of the conventional energy method can be found. The latest research about phased ISM was made by Zeng, et al. [26]. Although they utilized the absorption coefficient, which means that phase change was not included in the analysis at a reflection, the results showed an appreciable difference with the RTM results. The predicted reverberation time and sound pressure level agree better with measured data than the RTM. The reverberation time in a rectangular long enclosure was dealt with by the phased image source method [51,52]. In the study, the phased image source model can give a more accurate prediction than the incoherent model, which means the conventional ray tracing.

2.1. Necessity of Phase Information at Mid Frequency

2.1.1. Frequency Characteristics

The conventional geometrical methods to predict the acoustic performance of the concert halls and theaters have been used commonly at high frequencies. Although the applicable frequency range of geometrical acoustics method has been a controversial issue, the following Schroeder cutoff frequency might be used as a demarcation value distinguishing high frequency range from low frequency range [19,46,53]:

$$f_c = \sqrt{\frac{c_o^3}{4\ln 10} \cdot \frac{T_{60}}{V}}. \tag{2.1.1}$$

Here, c_o is the speed of sound in air (m/s), T_{60} the reverberation time (s), V the volume of the space (m^3). At high frequencies, because the resonance peaks are close together, i.e., fully populated within a band, the resonances are not evident. If the average spacing $(\Delta f)_{\mathrm{mode}}$ between peaks is of the order of or less than, say, $1/3(\Delta f)_{\mathrm{res}}$, the cluster of resonance peaks looks smooth and continuous. Schroeder frequency satisfies the relation of $(\Delta f)_{\mathrm{res}}=3(\Delta f)_{\mathrm{mode}}$.

Beyond the Schroeder cutoff frequency, the space can be assumed as a reverberant sound field statistically. Some researchers categorized the frequency range into three parts [21,53], i.e., low, mid, and high frequency, using f_c. Below f_c, the frequency range is presumed as low frequency range. The mid frequency range is defined between f_c and 4 f_c. At high frequencies over 4 f_c, the wavelength is small enough to apply the geometrical acoustics or statistical acoustics technique.

At low frequencies, the wave based method such as the finite element method, the boundary element method, or the finite time difference method can be devoted to predict the acoustic characteristics, mainly used for obtaining the frequency response function. FEM can analyze the sound field very accurately by discretizing the entire interior region of the room into finite acoustic elements with the surface impedance of the wall. The main advantage of the FEM is that the structural coupling to the sound field can be included by modeling the structural wall as an elastic finite element. On the other hand, the BEM requires the discretization of the boundary wall. In practice, the BEM is only applicable at low frequencies up to a few hundred Hz for a typical room size. The wave based methods are generally too expensive to be useful in the architectural environment, for which results are preferred in octave or 1/3 octave bands.

However, the medium frequency range still needs an appropriate method for the analysis and design. The phased beam tracing technique was suggested to overcome the inherent problems of energy method at mid frequencies by retaining the phase information in the geometrical acoustics. Consequently, the accurate simulation of impulse responses can be achieved. Needless to say, the realistic prediction of impulse response in an enclosure is utmost important for the auralization with three-dimensional concept or the virtual acoustic simulation.

2.1.2. One-dimensional Beam Analysis

The phased geometrical methods was applied to the one-dimensional beam for estimating the vibrational distribution [54]. From the excitation point, the left and right going rays are propagating in both directions. Initially, the magnitudes of the propagating rays are determined as if the one dimensional beam is infinitely-extended. When the propagating ray is hit by the actual boundaries, the propagating direction becomes reversed. The vibration energy is diminishing as the ray travels and the calculation stops when the assigned number of reflection is satisfied. The vibration level is calculated by summing all the contributions of the rays. The results were compared with the exact solution obtained by the traveling wave method in which the vibrational fields are modeled as superposition of traveling waves. Governing equations of the beam are given by

$$\begin{aligned}
&\frac{EI_z}{R}\frac{d^2}{dx^2}\left(\frac{u}{R}-\frac{dv}{dx}\right)+ES\frac{d}{dx}\left(\frac{du}{dx}+\frac{v}{R}\right)=-\rho S\omega^2 u;\\
&EI_z\frac{d^3}{dx^3}\left(\frac{u}{R}-\frac{dv}{dx}\right)-\frac{ES}{R}\left(\frac{du}{dx}+\frac{v}{R}\right)=-\rho S\omega^2 v;\\
&-EI_y\frac{d^4w}{dx^4}+\frac{GJ}{R^2}\frac{d^2w}{dx^2}+\frac{EI_y+GJ}{R}\frac{d^2\phi}{dx^2}=-\rho S\omega^2 w;\\
&GJ\frac{d^2\phi}{dx^2}-\frac{EI_y}{R^2}\phi+\frac{EI_y+GJ}{R}\frac{d^2w}{dx^2}=-\rho I_p\omega^2\phi.
\end{aligned} \tag{2.1.2a,b,c,d}$$

Here, u denotes the normal displacement (m) along the axial direction x, v and w are displacements (m) in the direction of y and z axes, respectively, ϕ the rotation about the axial axis x, E and G the complex elastic and shear modulus (Pa), respectively, ρ the mass density (kg/m^3), I_p the polar moment of inertia of the section (m^4), S the cross sectional area (m^2), I_y and I_z principal moment of inertial of the section (m^4), J the torsional constant (m^4), and R the radius of curvature (m). Figure 2.1 shows an application example of a curved beam model with structural loss factor of η=0.05. The radius of curvature was 0.25 m and the beam length was 1 m. The square sectional area is 10^{-4} m^2 and the right end node is excited. 100 Hz pure tone was excited and the excitation forces are given by $\{N, F_y, M_z, T, F_z, M_y\}^T = \{-1,\ 5,\ 0,\ 0,\ 0,\ 0\}$. Here, N is the longitudinal force, F_i the flexural force in the direction of subscript, T the torque, M_i the moment with respect to the subscript axis. The number of reflections was set to 400. As can be seen in Fig. 2.2, the phased RTM shows better agreement than the conventional RTM. It was discussed that the RTM shows the smoothly changing and spatially averaged distribution without oscillations whereas the RTM with phase perfectly agrees with the exact solution for one-dimensional case [55]. In one-dimensional structure, the plane wave can be completely interpreted by the ray and the iterative calculation of reflected sound field starting from the infinitely extended structure corresponds perfectly with the wave based method. At high frequencies, all simulation results from the RTM with/without phase showed a good agreement with the exact solution.

Figure 2.3 shows the convergence of the vibration level with respect to the reflection number at x=0 and x=0.5 m, respectively. At x=0, the longitudinal displacement should be zero, because the left end was clamped. However, the results by RTM converges to a positive number with a monotonic increase. One of the pitfalls of energy method is the overestimation of the response as depicted in Fig. 2.3(a). The addition of energy must increase, because only the energy is expressed in terms of a real positive number in the calculation. But, in the phased RTM, the complex numbers are involved, so the summed displacement/velocity converges to a certain value with fluctuation as the reflection number increases as can be seen in Fig. 2.3. At x=0.5 m, the result of phased RTM shows a fluctuation pattern during the convergence of the response, while the RTM result shows a trend of monotonic increase with rather smaller value. This one dimensional example demonstrated a possibility of phased method in the analysis of low frequency response, so that the same conclusion can be drawn by either the particle or the wave property. It should be mentioned that no wave phenomenon such as the diffraction and scattering happens except for the interference in one-dimensional structure. For three-dimensional space, more studies on the scanning error of the ray/beam tracing and the wave phenomena should be counted to reduce the error of the simulation.

2.2. Phased Ray Tracing Method (PRTM)

The phased ray tracing method is the amended version of the ray tracing method by keeping the phase information during the propagation of rays. The main difference between the phased method and the conventional ray technique is the primary variable of interest; pressure response which is complex-valued and real valued energy response, respectively. Consequently, the engaged variables in the phased RTM should be the complex number instead of real number.

In this regard, the acoustic property of the surface should be represented by the pressure reflection coefficient, which is defined as the ratio of reflection pressure to the incident pressure, in the phased RTM. This reflection coefficient conveys not only the information of phase shift at the wall, but also amplitude change at each reflection. The absorbed portion of sound energy can be easily obtained using the squared absolute value of the reflection coefficient. In addition, complex wavenumber must be utilized during the propagation of the ray. It is noted that the complex wavenumber implies the air attenuation factor as an imaginary part.

In the ray tracing method, rays carry the energy quantity. Emitted ray possesses some amount of energy at the starting point and, during the propagation within an enclosure, it loses a part of initial energy owing to the air attenuation and the absorption at the hitting surfaces in Fig. 2.4(a). As a result, energy reflectogram (or echogram) for a frequency band can be found using the arrival time of a beam and the energy at that time at the observer point.

However, as can be seen in Fig. 2.4(b), the pressure fluctuates as the ray propagates in the phased ray tracing method. From the source surface to the reflection point on the surface, the pressure decreases according to the geometrical divergence. When the ray meets the boundary, the reflected pressure is determined by the pressure reflection coefficient. Again, the ray travels from the surface to the receiver. It should be noted that the geometrical divergence is automatically counted regardless of types of wave. For example the geometrical divergence for spherical wave, known as $1/a_{tot}$, is automatically counted, because the density of the ray gets lowered as the distance between the adjacent rays becomes widen. Then the resulting pressure at the receiver can be expressed as:

$$p = p_o e^{j(k+j0.5m)a_{tot}} \prod_{i=1}^{n} r_i(\theta_i)\,, \tag{2.2.1}$$

where p_o is the initial pressure amplitude (Pa), a_{tot} the total travel distance of a beam (m), k the wave number in the lossless free field (1/m), m the air attenuation factor, $r_i(\theta_i)$ the pressure reflection coefficient of the ith reflection, and θ_i the angle of incidence of the beam, n the total number of reflections. When the pressure impulse response is obtained, various acoustic measures such as reverberation time and definition, etc. can be calculated in order to evaluate the acoustics of an enclosed space.

2.3. Phased Beam Tracing Method (PBTM)

The results of the ray tracing method rely greatly on the number of rays and receiver size. There were some previous works on the determination of receiver size [27-29]. Lenhert suggested the radius of a spherical receiver considering the maximum length of the ray path and the number of emitted rays [27]. Instead of the length of the ray path, the size of the space was taken in to account to determine the receiver volume by Yang and Shield [28]. Recently, Zeng, et al. made a formula for the radius of the receiver in consideration of both source to receiver distance and the space volume [29]. If the receiver volume is very small, any direct sound can not be detected as seen in Fig. 2.5(a). When the receiver size is increased, a direct ray from the source can be discovered (see Fig. 2.5(b)). As the receiver size becomes bigger and bigger, additional rays are detected as a direct sound in Fig. 2.5(c). Consequently, the early parts of the impulse response are overestimated. The results of RTM/PRTM are greatly influenced by the receiver size. In the case of Fig. 2.5(a), one has to increase either the ray number or receiver size. Increase of ray number can be a proper solution of this problem because it enables the distance between two adjacent rays narrowed.

As an alternative to resolve the detection problem, the beam tracing method can be adopted. Beams can densely cover the space to describe the propagation of spherical wave. While infinitesimally thin rays and receivers with finite volume are used to simulate the room in the ray tracing method, the beams with diverging cross section and point receivers are employed. The detection process is a bit complicated, but it can fix the overestimation or underestimation of early arriving sound. The resulting pressure at the receiver can be expressed as:

$$p = \frac{p_o}{a_{tot}} e^{j(k+j0.5m)a_{tot}} \prod_{i=1}^{n} r_i(\theta_i) \,. \tag{2.3.1}$$

Two important techniques of the beam tracing are the cone tracing method and the triangular beam tracing method. The cone tracing was suggested by Maercke and Martin [6], but it has a problem of overlapping between the cones and inefficient representation of the spherical wavefront. The triangular beam tracing method was firstly introduced in conjunction with the diffusion model by Lewers [7] and further developed by many researchers such as Farina [56], Stephenson [57], Shin and Ih [21], Drumm and Lam [33], Campo, et al. [34], and Funkhouser, et al. [35]. The split-up algorithm for the beam was taken up in the recent researches to minimize the scanning error [33-35]. The present beam model is mostly based on the Lewers model and small changes were made.

Once the receiver is detected, all the contributions of beams are saved for each frequency. The calculation is terminated after the assigned number of reflections is reached (or the pressure is converged to a certain value). From the pressure reflectogram for a frequency, the steady-state response can be obtained simply by the summation of direct sound and successive transient components. If the steady-state pressure is computed for all frequencies within the frequency range of interest, steady-state transfer function is constructed. Finally, one can use the steady-state transfer function to obtain an impulse response by taking the inverse Fourier transform.

2.3.1. Modeling of Sound Source

Traditionally the source is divided into a number of tiny pieces, statistically or deterministically. The deterministic method is to divide the source in a mathematical or geometrical manner. The divided sectional area of the beams should be identical or at least more or less the same. The azimuth and elevation angles of the beams can be set by the random number generation in a statistical approach. Randomly selected points on the surface of a source sphere can be represented by three parameters: radius, azimuth and, elevation angle. Kulowski's source division algorithm utilizes the rectangular shaped element and the normal vector at the centre of an element is chosen as the ray direction [2]. Lewers has suggested source division algorithm based on the icosahedron [7]. In the present method, the source division was based on the icosahedron and extension was made by splitting into several small equilateral triangles by a factor of n_s^2 as depicted in Fig. 2.6. The subdivided icosahedron will be projected onto the sphere and the vector from the source point to the projected point will be the edge of the triangular beam in Fig. 2.7. In this way, all the divided triangular beams can have more or less the same area. The division based on the cubic shaped source will be discussed in the Appendix B. Generally for the simulation and evaluation of an enclosed space, the spherical shaped source is enough to generate the uniformly distributed beams.

2.3.2. Trace of Beam Path

The ray is reflected from the surface according to the Snell's law when the scattering effect is neglected. For the smooth surface, the specular reflection is apparently predominant, therefore it is assumed that the scattering can be negligible. From the acoustical point of view, roughness of the surface should be smaller than the wavelength to satisfy the assumption of smooth surface. Usually the diffraction is not taken into account in the calculation, so the accuracy of the simulation with many edges and corners may not be so reliable. This problem will be resolved by the aid of the uniform theory of diffraction later in Chapter 4. In the beam tracing method, heading direction of a beam, reflected plane, and reflection points should be saved in the memory for each reflection and those are later used to detect the receiver. Depending on the flight distance, the phase information of exp($-jka_{tot}$) is easily determined. If one knows the traveling distance, then the time of arrival is automatically determined.

In this study, the central axis tracing, which means the triangular beam is reflected by following the central axis, was adopted. Naturally the beam should diverge, as the beam propagates. However, if any one of three edges of the beam hit another surface, scanning error [7,31,34,58] can be caused as depicted in Fig. 2.8, because the beam must follow the central ray without splitting. This scanning error can be corrected by splitting the beam in an appropriate way [33-35], but splitting technique needs lots of calculation time and additional computer memory.

The algorithm for searching the point of reflections is as follows. First, the surface on which the central ray is reflected can be determined by choosing the minimum distance from the former reflection point. After that, all the edges will follow the axis being reflected form the same plane where it hits. The reflected direction can be found by Snell's law for each edge as follows:

$$\overrightarrow{R_d'} = \overrightarrow{R_d} - 2\left(\overrightarrow{R_d} \cdot \overrightarrow{N}\right)\overrightarrow{N}\,. \tag{2.3.3}$$

where $\overrightarrow{N}$ is the outer normal vector of the surface and $\overrightarrow{R_d}$ and $\overrightarrow{R_d'}$ represent the direction of incident and reflected ray, respectively. Fig. 2.9 illustrates the reflection on the surface. When the direction of reflected ray is decided by the

Snell's law, three normal vectors of the beam for each side wall can be determined as shown in Fig. 2.10. There are two normal vectors perpendicular to the side wall, but only the outward normal vector can be decided by considering the third reflected ray. The angle between the outward normal vector and the third vector should be obtuse.

One of the advantages of the PBTM over the PRTM is that relatively small number of emitted rays is needed [23]. If the pure ray tracing technique is employed, more number of rays should be emitted from the source in order to search a receiver location properly. The distance between the adjacent rays gets widen as the ray propagates, therefore, either the number of rays or the receiver size should be increased. For the medium-sized room (say, the characteristic length of the room is about 5 m), 8000 rays and the receiver radius of 0.1 m are required to get a proper impulse response, while using the beam tracing method, only 1000 beams and point receiver are enough, because the space is quite densely covered by the beams for a directly incident wave.

2.3.3. Detection Algorithm

In the RTM, the detection of the arrived beams at the receiver region was made considering receiver size and ray vector. An infinitesimally thin ray can hit a part of the spatially extended receiver. The well-known method has been suggested by Kulowski [2], which is explained in Fig. 2.11. If the ray vector hits the spherical receiver, the total distance, ray numbering and its contribution are saved at every step. After hitting a receiver, the ray continues to propagate without any energy loss as if the receiver region is absolutely transparent. It can yield somewhat overestimated reflections. In the beam tracing, a point receiver and a beam with finite cross sectional span are engaged. The receiver can be found using the information on three normal vectors of the boundary walls and the receiver position [21]. As shown in Fig. 2.12, the angles between three normal vectors ($\overrightarrow{N_1}, \overrightarrow{N_2}, \overrightarrow{N_3}$) and the vector from the image source to the receiver position ($\vec{R}$) should be obtuse as follows:

$$\vec{R} \cdot \overrightarrow{N_i} < 0 \text{, for } i\text{=1,2,3.} \qquad (2.3.4)$$

The location of an image source can be found as

$$\overrightarrow{P_{IS}} = \overrightarrow{P_S} + d(\overrightarrow{R_i} - \overrightarrow{R_r}), \qquad (2.3.5)$$

where $\overrightarrow{P_{IS}}$ denotes the position of the image source and $\overrightarrow{P_S}$ the position of the real source, d the distance between two reflection points (m), $\overrightarrow{R_i}$ and $\overrightarrow{R_r}$ the directions of incident and reflected ray, respectively. The presence of acute angle means the failure in detection. As the beam diverges, the possibility to detect the receiver becomes higher due to the big span of the beam cross-section. After several reflections for small rooms, most of the beams can detect the receiver. This means that the late part of the reflection does not depend on the locations of the source and receiver, because the beam with wide span can hit the receiver wherever the receiver is located. This is one of the shortcomings of BTM that makes the calculations slow. In other words, the beam with very narrow span can sample the space very scrupulously at the beginning, but, subsequently, the wide beam scan the space roughly as the number of reflections increases. Once the receiver is detected, all the contributions of beams are saved for each frequency. The calculation is terminated after the assigned number of reflections is reached (or the pressure is converged to a certain value). From the pressure reflectogram for a frequency, the steady-state response can be obtained simply by the summation of direct sound and successive transient components. If the steady-state pressure is computed for all frequencies within the frequency range of interest, steady-state transfer function is constructed. Finally, one can use the steady-state transfer function to obtain an impulse response by taking the inverse Fourier transform.

2.3.4. Parameters in Calculation

In estimating a transfer function and an impulse response, great care must be taken to select the calculation parameters. Similar to the conventional geometrical technique, the number of beams is the topmost parameter in the phased beam tracing method. In addition, frequency resolution is of practical importance in the prediction of a transfer function and an impulse response in an enclosed space, which is related to the detectability of non-minimum phase zeros. Correct detection of non-minimum phase zeros is directly connected to the accumulated phase in a transfer function and late reverberation in an impulse response. Also the reflection order, sampling frequency in a transfer function and the temporal resolution in an impulse response will be discussed.

2.3.4.1. Number of Beams

It is well known that the results of the ray or beam tracing method mainly rely on the number of rays/beams and receiver size. The number of beam can influence the quality of the simulation in two ways. First, during the beam tracing process, the beam cross section becomes bigger (no matter how small the beam section was at the beginning), therefore the beam can not elaborately search the receiver. Second, if the reflection is described by the geometrical law of reflections without splitting, it is no longer true that the beam can perfectly cover the enclosed space whenever it hits more than two surfaces, edge, corner, and obstacles. Split of triangular beam needs additional calculation time and computational expenditure, so it will not be implemented in this study. Instead, the proper number of beams will be discussed for a rectangular room. Similar problem arises in the ray tracing method, because the fake detections are reported relying on the number of rays used in the simulation. There is a reasonable high probability that a ray will detect a surface with the area *S* after having traveled the time *t* if the area of the wave front per ray is not larger than *S*/2. This leads to following equation concerning the minimum number of rays, N_{beam} [5]:

$$N_{beam} \geq \frac{8\pi c_o^2}{S} t^2 , \tag{2.3.6}$$

where c_o is the speed of sound in air (m/s). By the definition of Schroeder cutoff frequency, Eq. (2.3.6) can be rewritten as

$$N_{beam} \geq 32\pi t^2 \left(\frac{f_c^2}{RT} \right)^{\frac{2}{3}} . \tag{2.3.7}$$

According to this criterion, the recommended numbers of beams depending on the size of the rooms are listed in Table 2.1. More than 10^4 beams are needed to calculate very accurately, however 2000 beams are practically enough for the accurate calculation of early part of an impulse response.

To investigate the number of detected beams at the arbitrary receiver point by changing the number of beams, a test room was chosen in Fig. 2.13. For rectangular parallelepiped room, there is one direct path and six first reflected paths (assuming no screen and obstacles existing in a room). Comparison of the number of detections by changing the number of beams is shown in Table 2.2. After second order of reflections, it is difficult to generalize the number of correct detections, because the detected number of beams obviously depends on the locations of source and receiver as well as the geometry of the room. In this situation the possible paths for 2nd reflection are eighteen. The number of detected beams at the receiver as a function of number of beams is illustrated in Fig. 2.14. According to the Fig. 2.14, twenty beams can densely cover the space for direct field and 1st reflection, however more beams are needed to simulate late reflection correctly. For 10th order of reflection, 21 paths are missed using 2000 beams compared to 8000 beams. Considering the mean free path of this room, time domain response around 0.18 s (traveling distance/speed of sound; 60/343) would be underestimated.

The reason for the underdetection with small number of beams is mainly due to non-split algorithm. After hitting edges and corners, the beams can not densely cover a space and consequently can not properly search its path. As the reflection order increases, the scanning errors are cumulated. Because the beam cross sectional area increases proportional to the square of distance, the hitting probability of the corner and edge dramatically increases. When the cross sectional area of the beam exceed the surface area of the larges wall, a receiver in a room can be detected by all beams, in principle.

The sectional area of the beam which is 1 m away from the point source is 1.6×10^{-3} m^{2,} when 8000 beams are employed. Provided that the mean free path is 6 m, after 30 reflections the cross sectional area becomes 50 m^2 which exceed the largest area of this room. However in the actual simulation, 3000 beams can hit the observation point owing to the cumulated scanning error.

2.3.4.2. Frequency Resolution

Transfer function (TF) or impulse response (IR) of an enclosed room implies the acoustic characteristics between two specified positions of source and receiver. They include the information of direct and reflected sounds and other related wave phenomena happening in a room. Mathematically, a room transfer function can be modeled by poles and zeros. Poles indicate the inherent acoustic characteristics of a room and zeros are related to the specific locations, which determine the magnitudes and times of multiple reflected sounds. Consequently, in the acoustic modeling of a room, the correct prediction of both position and magnitude of poles and zeros is very important. It is known that a fine frequency resolution is generally required to detect many important peaks and troughs in an actual room transfer function.

The major aim of this chapter is to propose a criterion for the proper frequency resolution to predict the room transfer function between source and receiver. The geometrical acoustic simulations are based on the high frequency assumptions dealing with an energy quantity and generally performed in the time domain. Hence the important criterion in the geometrical acoustics simulation is the length of the energy impulse response. From the energy impulse response, any physical explanations of modes and interference cannot be inferred. Opposite the time domain response, the frequency response function is useful in explaining the physical meaning of the wave behavior. One can see details of spectral nature such as peaks and troughs, of the source-receiver relation. Frequency response enables us to discuss the physical explanations of modes in a room at the resonant peaks and interference of waves at the non-resonant notches, etc. Theoretically, at any position in a room, poles never changes because it represents the room characteristics. In contrast, the zeros can migrate by changing the locations of source and receiver. The acoustic parameters change (sometimes significantly) from one seat to another due to the different locations of zeros in TF. That is why the zero detection is important. If the detection of zeros is conducted correctly, the simulated acoustic response will be very similar to the actual acoustic situation or measurement. For the acoustic prototyping of an enclosure, the auralization is also very important nowadays and the preparation for a very precise and realistic impulse response function is the essential point of such work. It should be mentioned that, although the discussion in this study looks similar to that on the frequency response function (FRF) estimators [59-61], this study is not concerned with the random error which is the main view point of various FRF estimators. The precision of the reverberation time, which is one of the representative temporal acoustic parameters, was taken as the test index. Here, the reverberation time was defined as T_{20}, which corresponds to the time duration for a sound decay by 20 dB (-5 dB ~ -25 dB).

Test room model is shown in Fig. 2.15 and the absorption coefficients of the room surfaces are listed in Table 2.3. The Schroeder's cutoff frequency [19] of the test room was about 310 Hz based on the measured reverberation time of 1.2 s in 500 Hz octave band and the mean free path [62] was 2.4 m. The number of triangular beams used in the PBTM simulation was 2000 and the maximum number of reflections was 200. Maximum number of reflections was selected by considering the reverberation time. About 175 reflections were enough for beams to fly 411 m which is equivalent to 1.2 s in the time of flight. Source and receiver were located at (2.30, 2.36, 1.30) and (5.29, 2.56, 0.65), respectively.

As a first attempt to investigate the effect of frequency resolution, two frequency resolutions, 0.1 Hz and 1 Hz were chosen for the transfer function in an octave band centered at 500 Hz. These correspond to the time length of impulse response of 10 s and 1 s, respectively. Figure 2.16 shows the steady-state transfer function between source and receiver. One can see that very narrow dips become sharper than the wide resolution case while peaks are rarely changed. This suggests that the frequency resolution affects the precision of zero estimation in the transfer function. As can be seen in Fig. 2.16, the finer the resolution is, the more the phase delays. This is because more non-minimum phase zeros can be detected when the frequency resolution becomes fine. The phase delay can be simply estimated from the number of non-minimum phase zeros as [63,64]

$$\Phi = -\pi\left(N_p + N_z^+ - N_z^-\right) = -2\pi N_z^+, \tag{2.3.8}$$

where N_p is the number of poles ($N_p = N_z^+ + N_z^-$), N_z^- the number of minimum phase zeros, and N_z^+ the number of non minimum phase zeros.

Figure 2.17 depicts a zoomed spectrum of room transfer function. In Fig. 2.17(a), zero crossings between 368 Hz and 369 Hz exist simultaneously in both real and imaginary part of transfer function; however, a pronounced dip in the magnitude of transfer function in Fig. 2.17(b) could be detected when the resolution was 0.1 Hz. The phase difference at 369 Hz, which is just above the non-minimum phase zero frequency, was exactly 2π. This zero cannot be detected with a frequency resolution of 1 Hz. Whenever such sparse sampling misses a non-minimum phase zero, a corresponding phase delay of 2π cannot be added to the total cumulative phase delay; then, one will estimate the acoustical characteristics inaccurately. Physically, an acoustical system with non-minimum phase zeros will have an initial response with opposite direction to the applied stimulus. Then, the overall response time will be long and the energy will be spread over the response time. On the other hand, minimum phase zeros serve to reduce the overall response time. As a result, a minimum phase system will have the energy distribution of the impulse response being concentrated on very early times. The number of non-minimum zeros is inversely proportional to the distance between the frequency of interest and the pole line [63-66], δ_0, which satisfies δ_0 =6.9/RT. Consequently, an acoustical system having many non-minimum phase zeros will yield a long reverberation time.

Figure 2.18 illustrates the predicted impulse response obtained by adopting two different frequency resolutions as in Fig. 2.16 for the transfer function. The discrepancy after 0.2 s became evident while two impulse responses before 0.2 s were almost identical. As discussed before, rich reverberant components owing to many non-minimum phase zeros make a long reverberation time. In Fig. 2.19, decay curves obtained by Schroeder's backward integration [67] were compared for two different frequency resolution cases. The rate of decay curve becomes slow as the frequency resolution is set small. For several frequency resolutions varying from 0.01 Hz to 1 Hz, the cumulative phase, the number of non-minimum phase zeros, and the corresponding reverberation time are listed in Table 2.4. One can clearly see that a small frequency resolution yields large phase delay, increased number of non-minimum phase zeros, and long reverberation time.

Figure 2.20 plots the relative error of reverberation time, which is defined by

$$\text{Relative error} = \frac{(\mathrm{RT})_p^c - (\mathrm{RT})_p}{(\mathrm{RT})_p^c} = \frac{1.18 - (\mathrm{RT})_p}{1.18}, \tag{2.3.9}$$

where $(\mathrm{RT})_p$ denotes the predicted reverberation time (s) for 20 dB decay, and

$(\mathrm{RT})_p^c$ signifies the numerically converged value of reverberation time (s), which was 1.18 s in the test case. The normalized time length in the abscissa is defined as the ratio between total time length of the impulse response and correct reverberation time as follows:

$$\text{Normalized time length} = T_{total} / (\mathrm{RT})_p^c . \tag{2.3.10}$$

It was suggested that the just noticeable difference (JND) of reverberation time is about 5% of the true value [68]. Based on this criterion, it can be said that the data length of impulse response must be longer than 3.5 times the reverberation time in Fig. 2.20. However, this conclusion can not be generalized in this stage and further research will be needed. From this simulation, the criterion of $\Delta f < 1/RT$ in ISO 18233 [69] causes about 30% error in the estimation of RT for this case.

A proper frequency resolution is connected to the average spacing of zeros. In the low frequency range, mode shape and modal density depend strongly on the geometry of the system as well as the boundary conditions. However, as frequency goes higher, the modal parameters are not strongly influenced by the geometrical shape, but by the volume of the space. The general result for the average frequency spacing between resonances, $\overline{\delta f}_p$, in a three-dimensional cavity is given by [15]

$$\overline{\delta f}_p = \frac{c_o^3}{4\pi V f^2} , \tag{2.3.11}$$

where c_o is the speed of sound, f the frequency, V the volume, and the subscript p the frequency spacing between poles. The number of zeros is identical to that of poles being proportional to the square of the frequency. Because zeros are randomly distributed, the frequency resolution Δf should be less than half of the average frequency spacing of zeros as follows:

$$\Delta f < \frac{1}{2}\overline{\delta f}_z = \frac{1}{2}\overline{\delta f}_p = \frac{c_o^3}{8\pi V f^2} . \tag{2.3.12}$$

As the frequency of interest becomes high, the frequency resolution should be made small. Accordingly, an additional time is required to calculate the high frequency response. The criterion in Eq. (2.3.12) suggests that the frequency resolution of this example for 500 Hz octave band should be less than 0.1 Hz and it agrees with the result in Table 2.4. It should be noted that this criterion was statistically found under the assumption of rectangular shaped room regardless of boundary conditions. Generally speaking, the less reverberant the room, the smaller the number of non-minimum phase zeros. Therefore, the criterion in Eq. (2.3.12) can be relaxed in dealing with an actual room with absorptive surfaces.

If the sparse data set is initially given, one way to improve the spectral details of a transfer function is the interpolation. As an example, the transfer function with a frequency resolution of 1 Hz was chosen and we attempted to change the frequency resolution to 0.1 Hz by linear or cubic spline interpolation. Interpolated transfer function and impulse response are compared with the original data in Figs. 2.21 and 2.22. One can find that the magnitude around dips and the phase delay are changed and the late parts of the impulse response are enriched by the interpolation. Table 2.5 compares the cumulative phase delay at 750 Hz, the number of non-minimum phase zeros, and the corresponding reverberation time, before and after the interpolation. One can observe that some zeros that were missed in the wide resolution case are newly detected by applying the interpolation and, as a result, the impulse response was also changed in Fig. 2.22.

In comparison with the initially small resolution case (Δf=0.1 Hz), the improvement in the cumulative phase delay, the number of non-minimum phase zeros, and the corresponding reverberation time is very distinct in Table 2.5. Figures 2.23 and 2.24 show the TF and IR, respectively, in which the result with a sparse frequency resolution (Δf= 2 Hz) is compared with the interpolated result. It is observed that the improvement was not noticeable if the linear interpolation was adopted (Fig. 2.24(a)). It is concluded that the precision of TF or IR was clearly enhanced by employing the cubic spline interpolation (Fig. 2.24(b)).

2.3.4.3. Reflection Order or Number of Reflections

Ideally, infinite number of reflection is preferred not to miss any contribution of beams. The finite number of reflections, however, is determined before the calculation and the calculation stops when the assigned number of reflection is reached. Usually before the main calculation, convergence check for one frequency component is conducted to determine the reflection order. Because the convergence rate for the lowest frequency of interest is the slowest, the reflection order which makes the steady-state response stabilized satisfactorily at the lowest frequency is chosen. Figure 2.25 shows the convergence of the steady-state pressure as a function of cumulative number of arrived beam. The convergence rates at low frequency and high frequency components are clearly shown in Fig. 2.25. At high frequency, the pressure converges monotonically while the low frequency steady-state pressure is converged with fluctuating. The convergence rate of the low frequency response is much slower than that of high frequency.

In the conventional geometrical acoustics, the reflection order is more related to the estimated reverberation time. If the reflection order is small, the reverberation time such as T_{30} can not be calculated from the energy reflectogram. The recommended reflection order in the conventional geometrical acoustics corresponds to the length of the impulse response considering the mean free path of the space. This issue for the conventional geometrical acoustics method is beyond the scope of this study and will not be discussed.

2.3.4.4. Sampling Frequency

In the present method, the frequency response is inversely Fourier transformed to obtain an octave band impulse response. The sampling frequency is actually the upper frequency of the transfer function. For instance, to have an impulse response in 125 Hz octave band, the frequency band in transfer function should be larger than the band from 88 Hz to 177 Hz. At least, the sampling frequency should be higher than 177 Hz.

2.3.4.5. Temporal resolution

Temporal resolution is inversely determined only by the sampling frequency of a transfer function. As the upper frequency of interest increases, temporal resolution gets small. If the temporal resolution is not small enough to represent the impulse response smoothly, the zero padding technique [70] can be adopted to increase the temporal details.

Table 2.1. Recommended number of beams depending on time length of IR.

Time length, t	No. of beams	Notes
0.7 s	6.2×10^4	Medium sized room (V~100 m^3, f_C=177 Hz)
0.35 s	2.6×10^4	Small sized room (V~50 m^3, f_C=88 Hz)
0.1 s	1.5×10^3	
0.08 s	1×10^3	Criterion for early reflections (80 ms)
0.05 s	400	Criterion for early reflections (50 ms)

Table 2.2. Number of detected beams according to the order of reflection.

Number of beams Reflection order	20	80	180	320	500	1280	2000	8000
0th (direct)	1	1	1	1	1	1	1	1
1st	6	6	6	6	6	6	6	6
2nd	12	16	18	18	18	18	18	18
3rd	17	30	38	38	38	38	38	38
4th	17	44	57	62	66	66	66	66
5th	19	52	74	90	97	101	102	102
6th	19	62	93	114	127	144	146	146
7th	20	63	113	139	165	190	193	198
8th	20	74	122	173	194	249	250	258
9th	20	72	142	191	224	300	313	326
10th	20	75	147	209	265	351	379	400

Table 2.3. Absorption coefficient of room surfaces in 500 Hz octave band.

Surface	Material	Absorption coefficient
Floor	Stone	0.03
Ceiling	Gypsum	0.09
Wall with door	concrete and wood	0.05
Wall with whiteboard	concrete and plastic	0.03
Window	Glass	0.07
Ventilation grating		0.5
Thin panel	Steel	0.15
Wall	Concrete	0.03

Table 2.4. Effect of frequency resolution on phase delay, number of non-minimum zeros, and corresponding reverberation time (750 Hz).

Δf	*1 Hz*	*0.5 Hz*	*0.2 5Hz*	*0.1 Hz*	*0.05 Hz*	*0.01 Hz*
Phase delay (rad.)	-265	-290	-296	-302	-302	-303
No. of non-minimum phase zeros	42	46	47	48	48	48
$(\mathrm{RT})_p$ (s)	0.72	0.97	1.12	1.17	1.17	1.18

Table 2.5. A comparison of phase delay, number of non-minimum zeros, and the corresponding reverberation time due to the application of data interpolation (750 Hz).

	Original data		After interpolation	
Δf	1 Hz	0.1 Hz	Linear, 0.1 Hz	Spline, 0.1 Hz
Phase delay (rad.)	-265	-302	-277	-296
No. of non-minimum phase zeros	42	48	44	47
$(\mathrm{RT})_p$ (s)	0.72	1.17	1.00	1.10

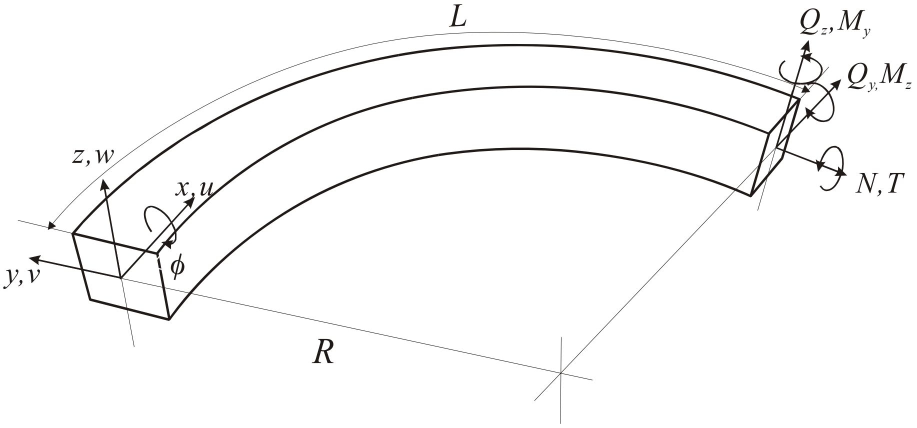

Fig. 2.1. Coordinate system of the curved beam model with loss factor, η=0.05. The left end is clamped and right end is free. The radius of curvature was 0.25 m and the length of the beam was 1 m.

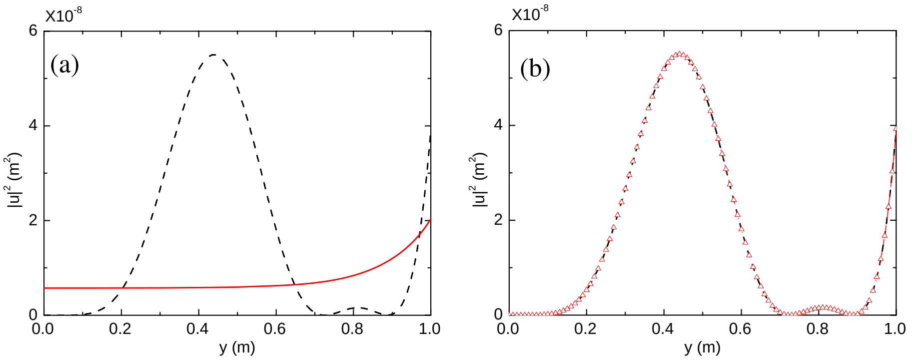

Fig. 2.2. Comparisons of vibration response calculated from three methods for a pure tone excitation at 100 Hz. Quadratic longitudinal displacement is calculated as a vibration response. (a) Ray tracing method, (b) phased ray tracing method. – – – –, Traveling wave method; ——, ray tracing method; △, phased ray tracing method.

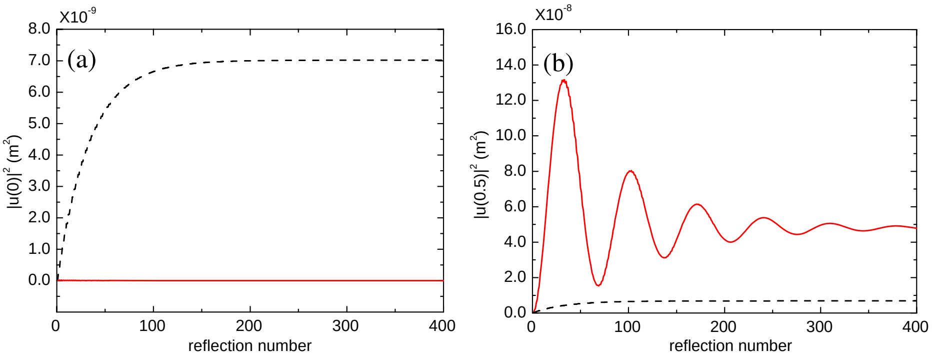

Fig. 2.3. A comparison of convergence of quadratic longitudinal displacement with increase of the reflection number. (a) At x=0, (b) at x=0.5 *m*. – – – –, RTM without phase; ——, RTM with phase. In Fig. 2.3(a), the result from RTM with phase are all zeros.

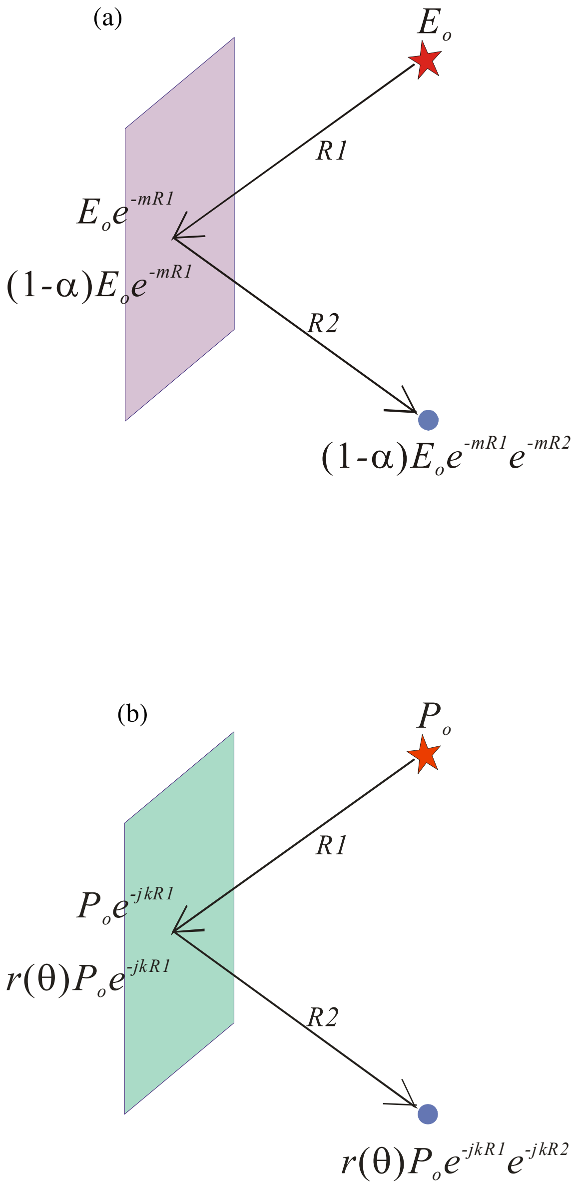

Fig. 2.4. A comparison of basic concepts of ray tracing and phased ray tracing method, (a) Conventional ray tracing method, (b) phased ray tracing method.

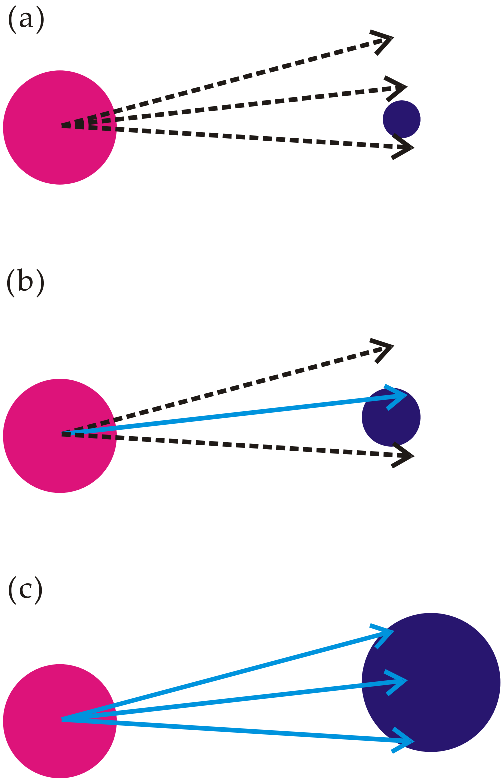

Fig. 2.5. Detection of direct ray depending on the receiver size. (a) No direct ray is detected for small sized receiver, (b) single direct ray detected, (c) several direct rays detected.

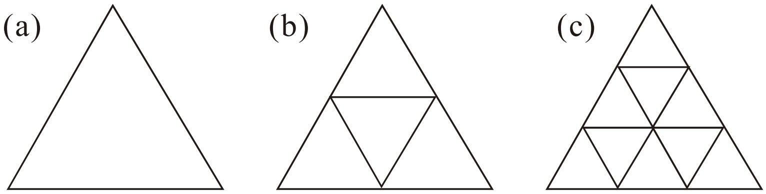

Fig. 2.6. Subdivision of a triangle (n_s = the subdivision factor). (a) n_s=1, (b) n_s=2, (c) n_s=3.

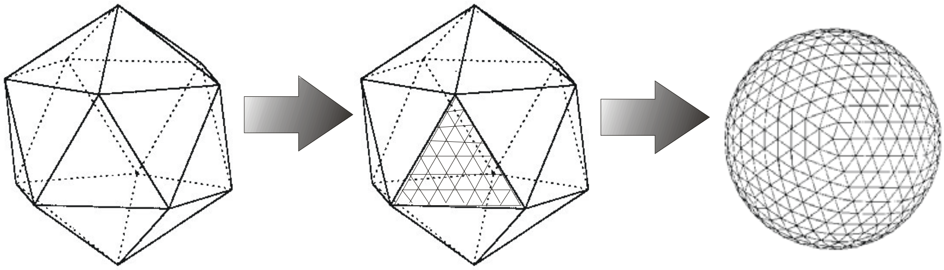

Fig. 2.7. Division of a sound source for the approximation of small triangles [21].

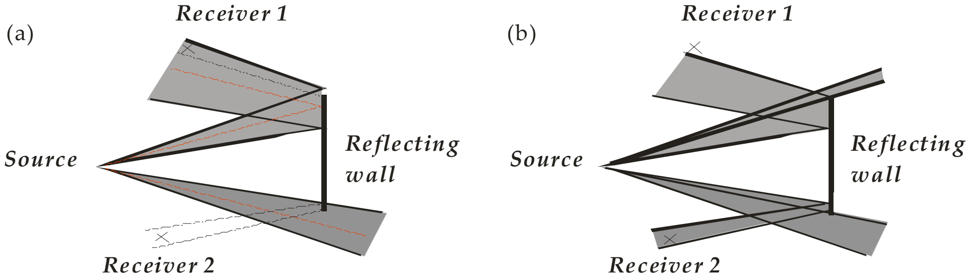

Fig. 2.8. Occurrence of scanning error owing to the central axis tracing. (a) Receiver 1 is included by the beam and receiver 2 is not hit by the beam, (b) receiver 1 is located outside the beam and receiver 2 is detected by the beam.

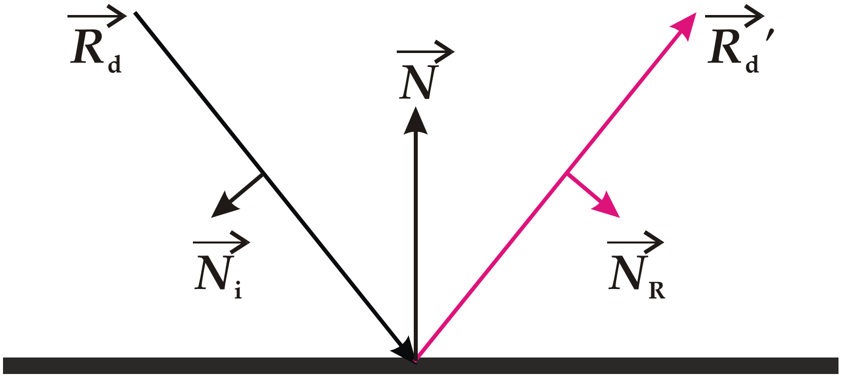

Fig. 2.9. Snell's law in two-dimensional case. $\vec{N}$ denotes the outer normal vector of the surface and $\vec{N}_I$ and $\vec{N}_R$ the outer normal vector of the incident ray and reflected ray, respectively. θ_i and θ_r mean the angle of incidence and angle of reflection, respectively. $\vec{R}_d$ and $\vec{R}_d^{'}$ represents the direction of incident and reflected ray, respectively.

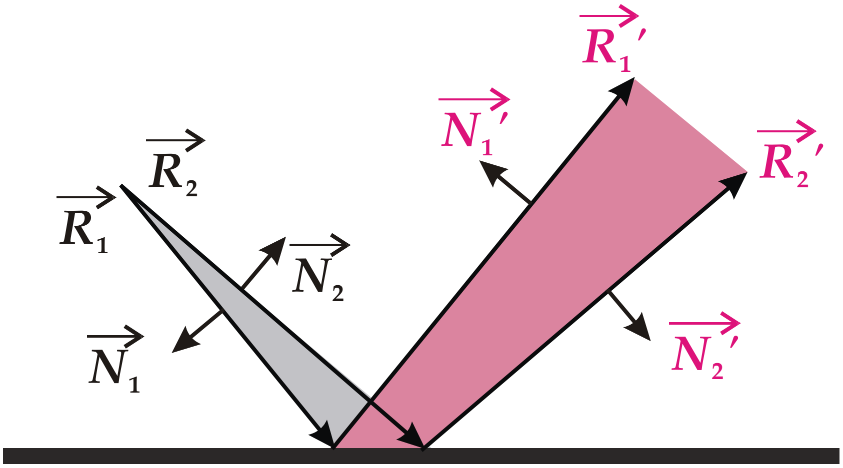

Fig. 2.10. Reflection of a beam in two-dimensional case. $\vec{N}_1$ and $\vec{N}_2$ mean the outer normal vectors of the incident two-dimensional beam and $\vec{N}_1^{'}$ and $\vec{N}_2^{'}$ the outer normal vectors of the reflected two-dimensional beam. $\vec{R}_1$ and $\vec{R}_2$ represent the edge vectors of the incident beam and $\vec{R}_1^{'}$ and $\vec{R}_2^{'}$ the edge vectors of the reflected beam.

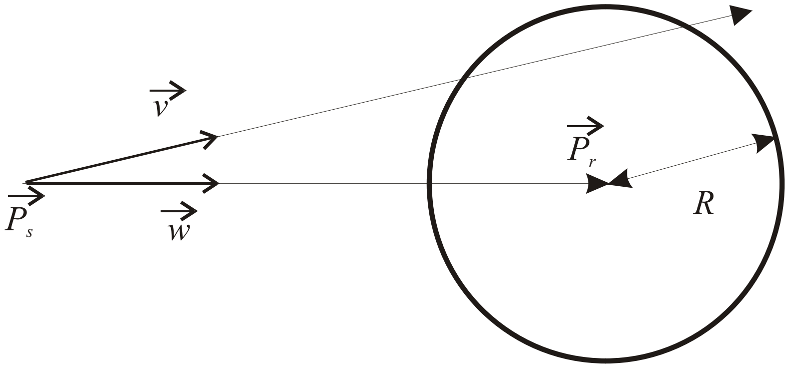

Fig. 2.11. Arrival of a ray at the observation region [2]. The receiver can be detected when $A^2 - B + R^2 \geq 0$, where $A = \vec{v} \cdot \vec{w}$ and $B = |w|^2$. The $\vec{P}_s$ and $\vec{P}_r$ denote the source and receiver position, respectively. $\vec{v}$ is the ray direction and $\vec{w}$ the vector between the reflection point and the sphere center. *R* denotes the radius of the curvature of the sphere.

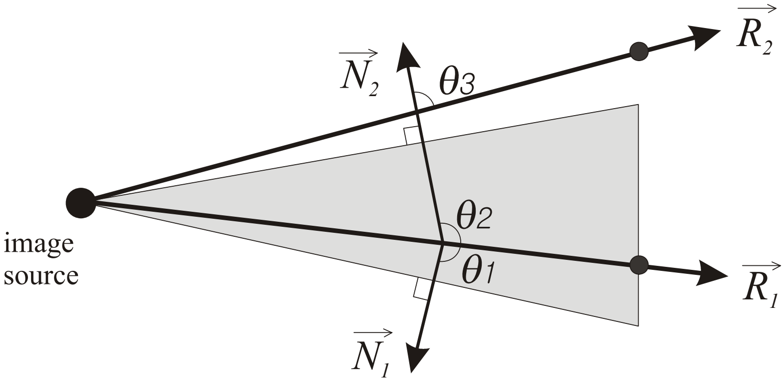

Fig. 2.12. Detection algorithm for triangular beam tracing method [21]. $\vec{R}_1$ and $\vec{R}_2$ denote the vectors between the source image source and the receiver 1 and 2, respectively. The shaded region represents the triangular beam and $\vec{N}_1$ and $\vec{N}_2$ denote the outer normal vectors of the beam. In order to be detected by the beam, angles between $\vec{R}$ and the outer normal vectors should be obtuse. In the case of receiver 1, all the angles are obtuse. In case of receiver 2, it cannot be detected by the beam due to acute angle of θ_3.

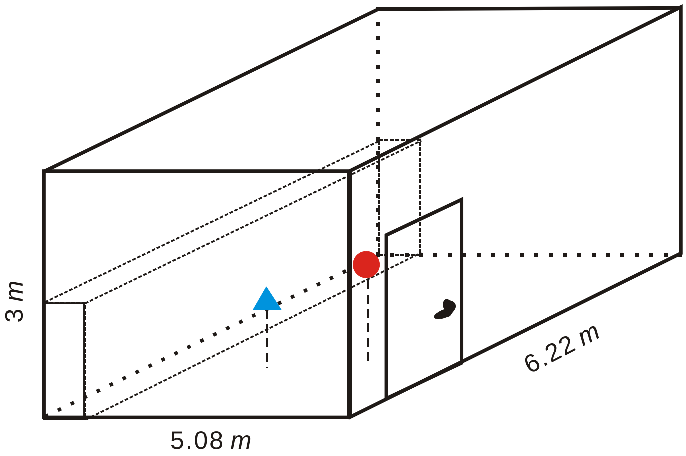

Fig. 2.13. Test room model. ●, Source; ▲, observer. Surface properties are listed in Table 2.3.

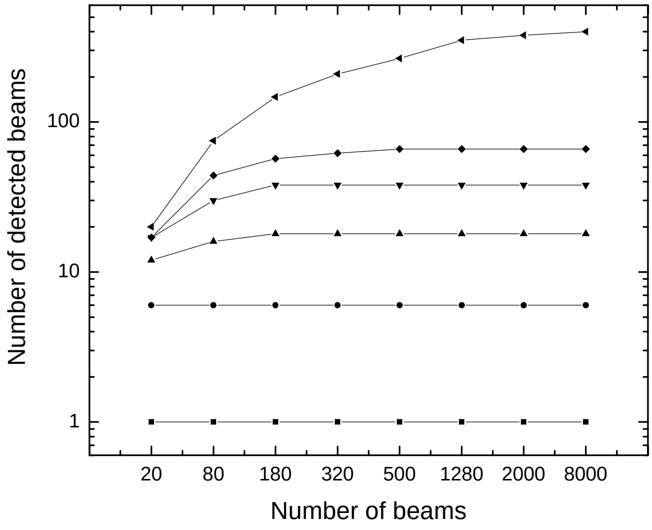

Fig. 2.14. Number of detected beam as a function of number of beams. —■—, Direct sound; —●—, 1st reflection; —▲—, 2nd reflection; —▼—, 3rd reflection; —◆—, 4th reflection; —◀—, 10th reflection.

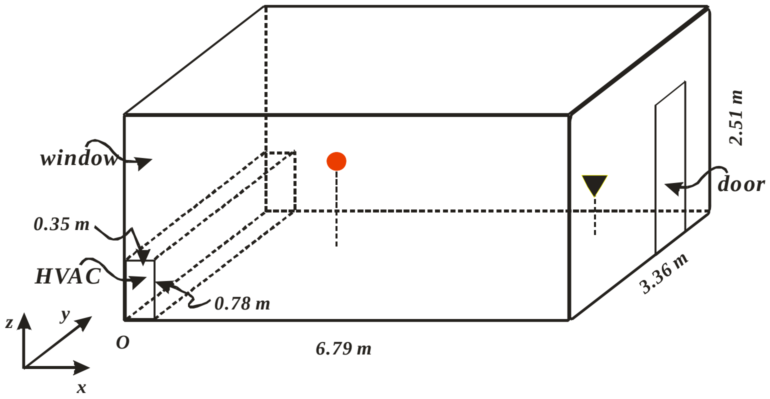

Fig. 2.15. Test room geometry. ●, Source; ▼, observer. Wall properties are listed in Table 2.3.

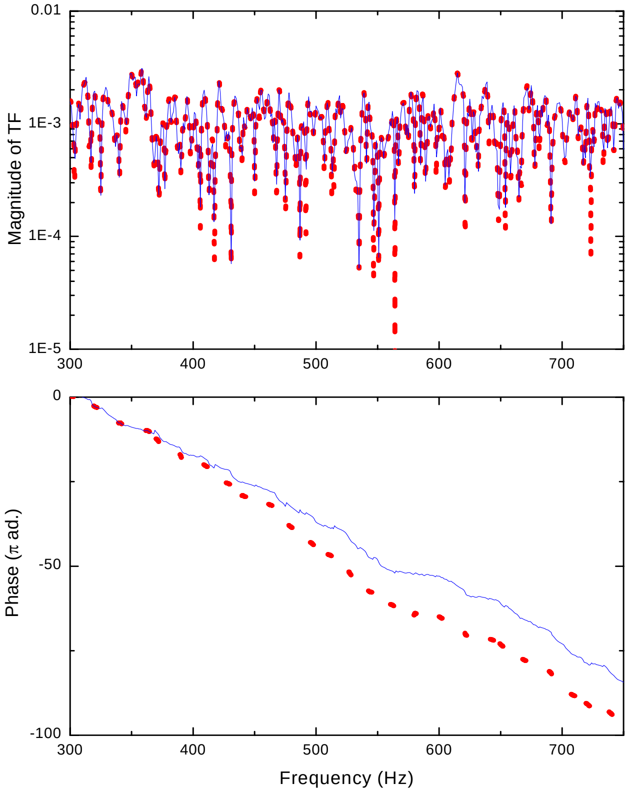

Fig. 2.16. Steady-state transfer functions for two different frequency resolutions, Δf: ——— ,Δf=1 Hz; ●●●●,Δf=0.1 Hz.

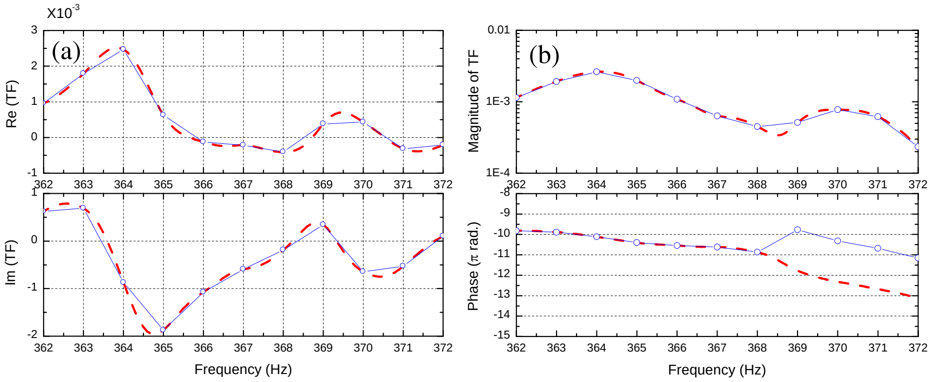

Fig. 2.17. A comparison of zoomed transfer functions for two different frequency resolutions, Δ*f*: —○—, Δ*f*=1 Hz; - - -,Δ*f*=0.1 Hz. (a) Real and imaginary parts, (b) magnitude and phase.

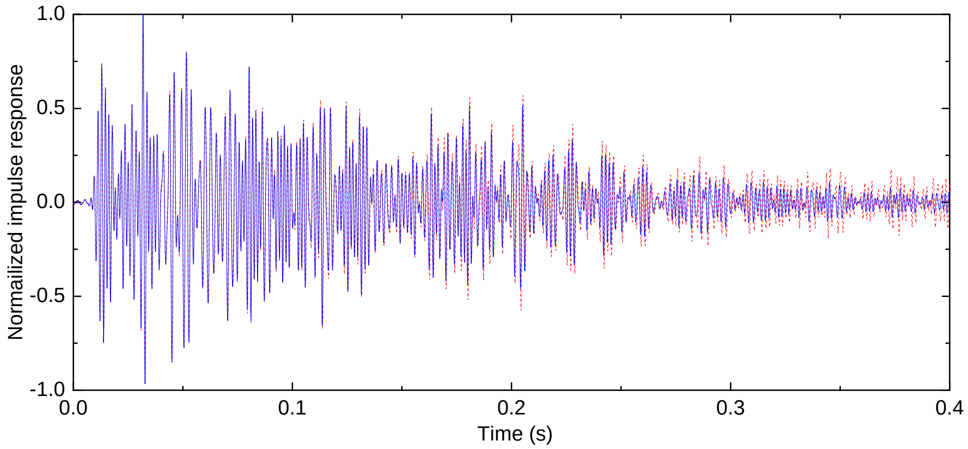

Fig. 2.18. A comparison of impulse responses varying the frequency resolution: ——, Δ*f*=1 Hz; - - -,Δ*f*=0.1 Hz.

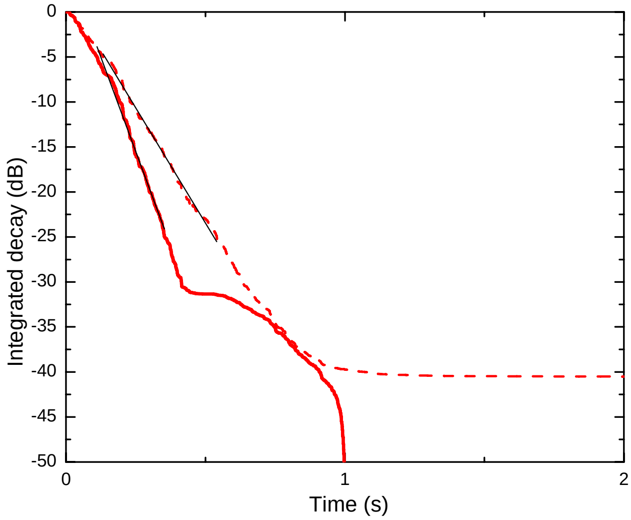

Fig. 2.19. A comparison of decay curves. ——, Δ*f*=1 Hz; - - - -, Δ*f*=0.1 Hz. Thin solid line (——) displays the least square regression line for calculating T20.

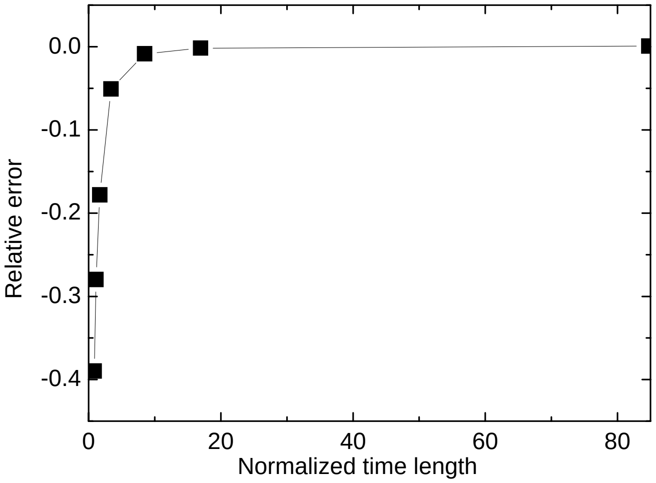

Fig. 2.20. Relative error as a function of the normalized time length.

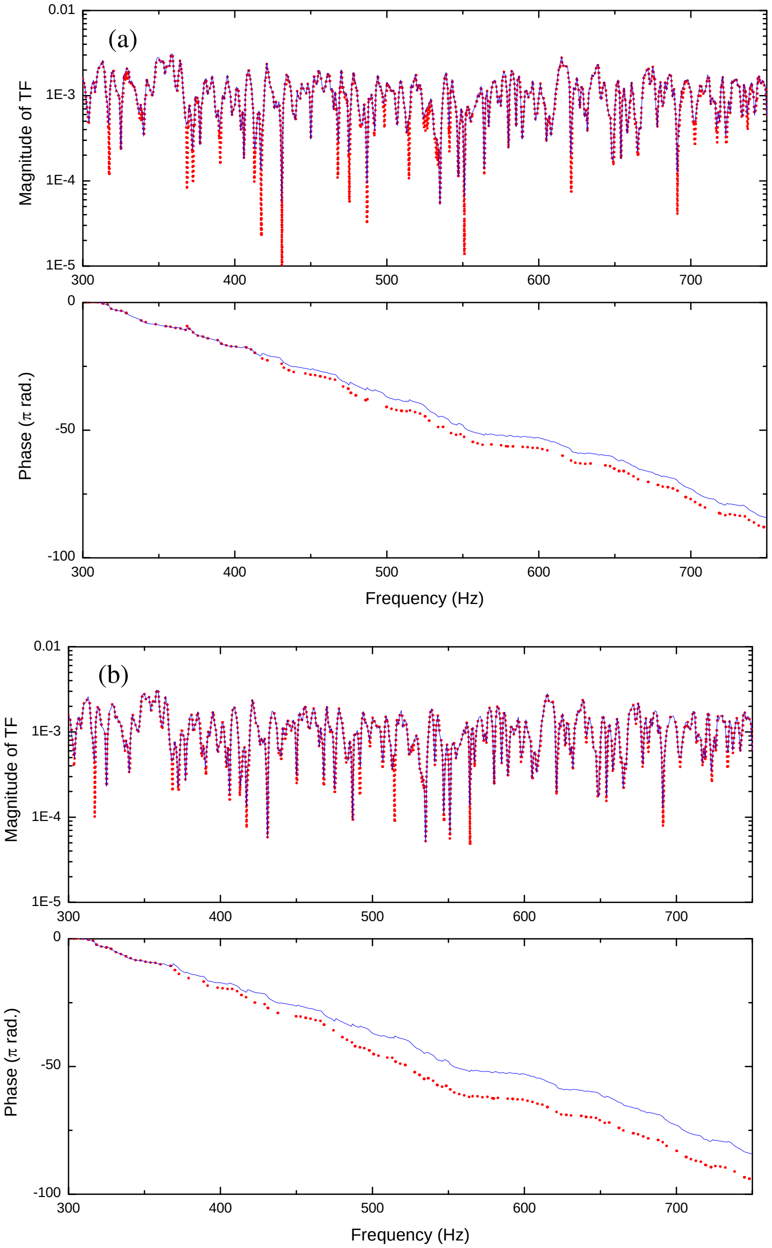

Fig. 2.21. Comparisons of transfer functions: ——, Original Δf=1 Hz; – – –, interpolated. (a) Linear interpolation, (b) cubic spline interpolation.

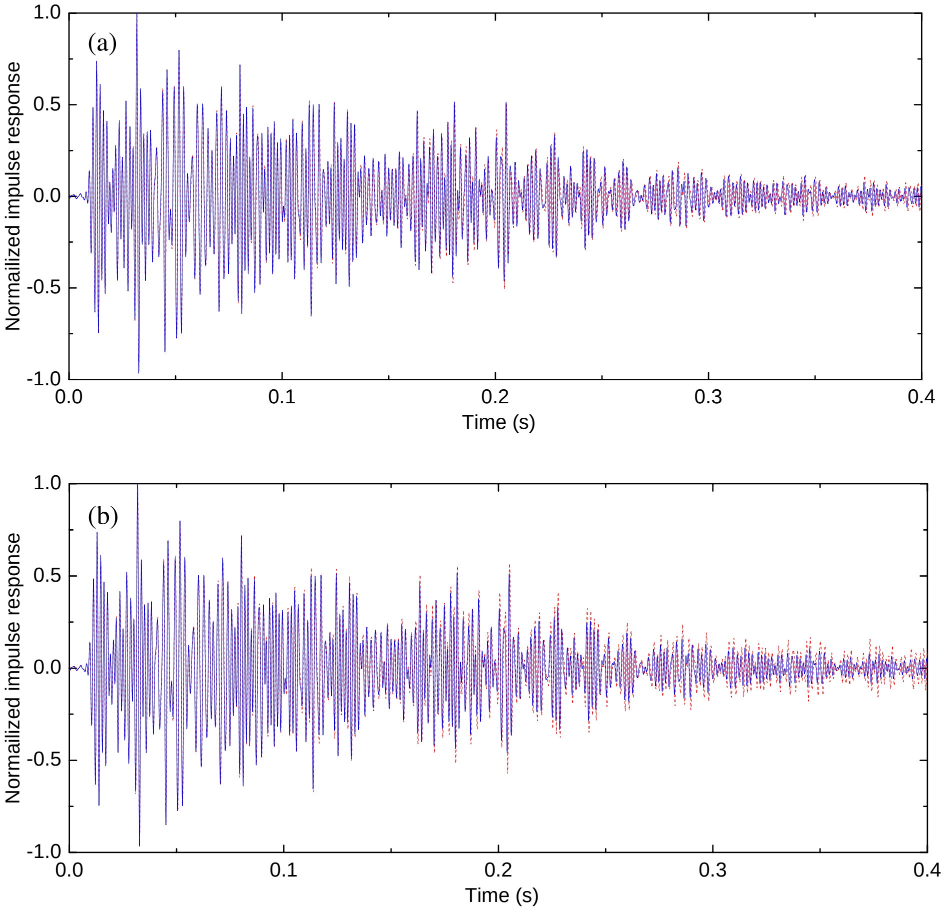

Fig. 2.22. Comparisons of impulse responses: ——, Original Δf=1 Hz; – – –, interpolated. (a) Linear interpolation, (b) cubic spline interpolation.

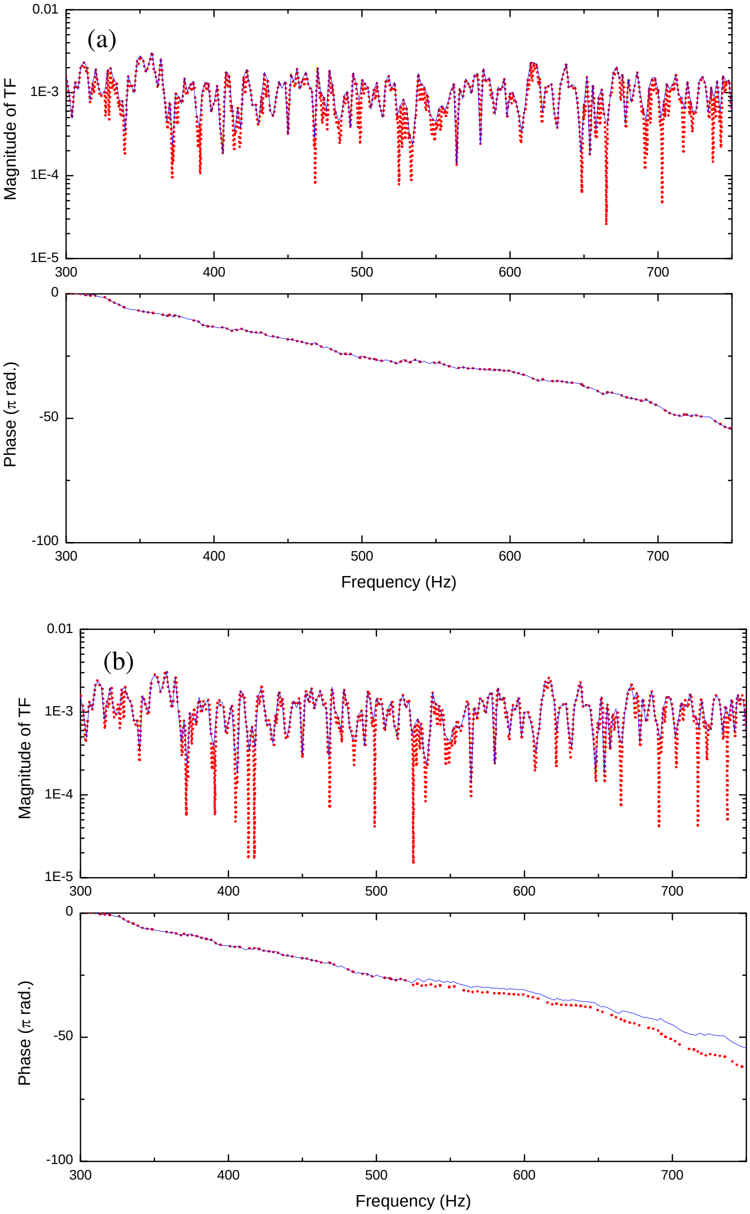

Fig. 2.23. Comparisons of transfer functions: ——, Original Δ*f*=2 Hz; ••••••, interpolated. (a) Linear interpolation, (b) cubic spline interpolation.

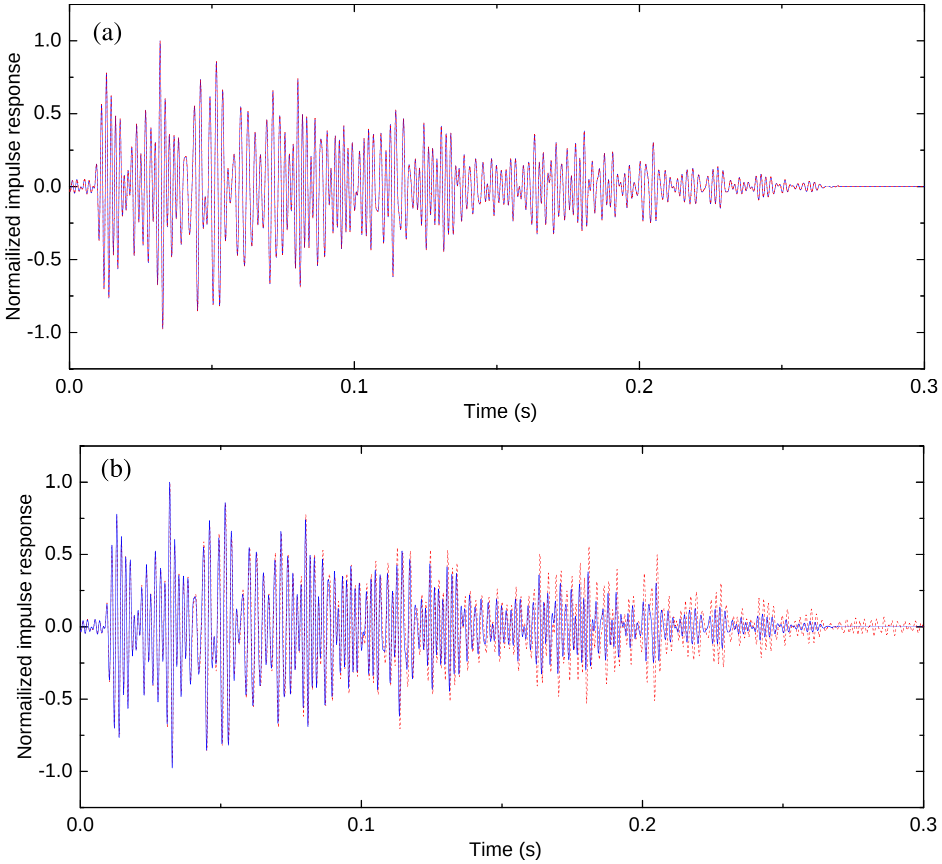

Fig. 2.24. Comparisons of impulse responses: ——, original Δf=2 Hz; ••••••, interpolated. (a) Linear interpolation, (b) cubic spline interpolation. In Fig. 2.24(a), two curves are perfectly overlapped.

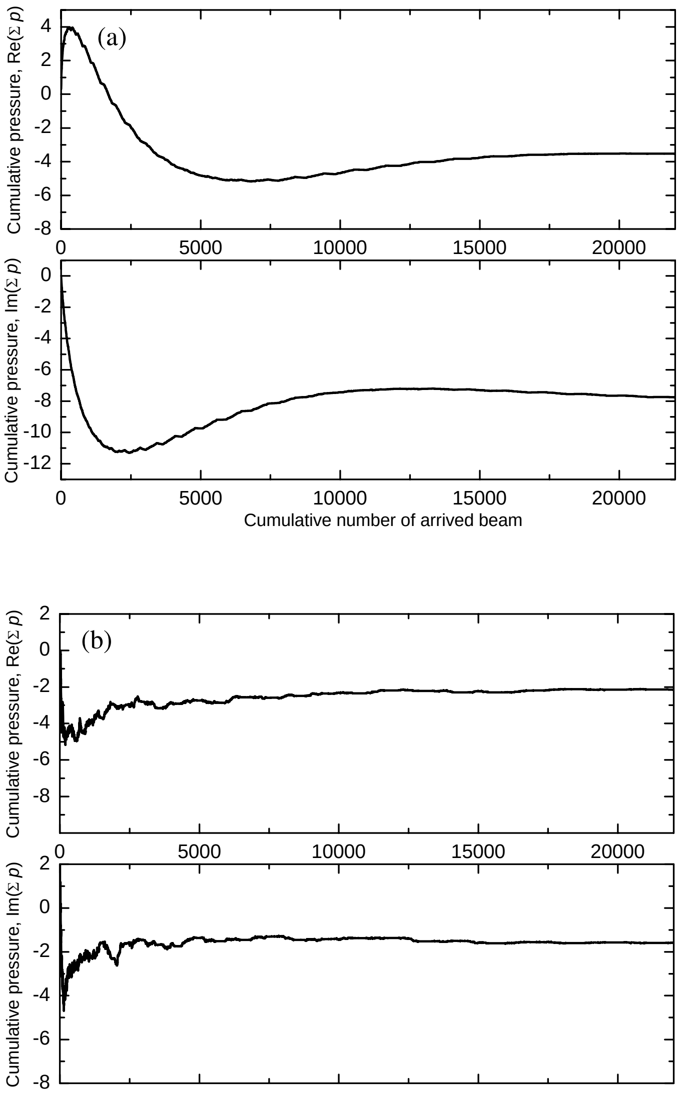

Fig. 2.25. Convergence check for the steady-state pressure. (a) *f*=90 Hz, (b) *f*=1000 Hz.

3. TREATMENT OF REFLECTION AT MID FREQUENCY

3.1. Reflection Coefficient

3.1.1. Definition

Reflection coefficient plays an essential role in the phased beam tracing method to predict a pressure impulse response. In fact, it can be easily calculated from the measured surface impedance, if the data are available under the assumptions of *plane wave incidence* to the *infinitely large* panel: [71]

$$r = \frac{Z_w \cos\theta_1 - \rho c_o \cos\theta_2}{Z_w \cos\theta_1 + \rho c_o \cos\theta_2}. \tag{3.1.1}$$

Here, Z_w means the surface impedance of the wall (rayl) and θ_1 and θ_2 the angle of incidence and angle of refraction, respectively. When the relationship of $k_2 \sin\theta_2 = k_1 \sin\theta_1$ is substituted, the plane wave reflection coefficient is expressed as [72]

$$r = \frac{Z_w \cos\theta_1 - \rho c_o (1 - k_1^2 / k_2^2 \sin^2\theta_2)^{1/2}}{Z_w \cos\theta_1 + \rho c_o (1 - k_1^2 / k_2^2 \sin^2\theta_2)^{1/2}}. \tag{3.1.2}$$

The propagation in the second medium, e.g. the wall behind the surface, can be ignored by the *locally reacting material* assumption. Then the reflection coefficient reduces to [73]

$$r = \frac{Z_w - \rho c_o / \cos\theta_1}{Z_w + \rho c_o / \cos\theta_1}. \tag{3.1.3}$$

The term of $\rho c_o/\cos\theta$ corresponds to the radiation impedance from the infinitely large normal impedance boundary. However, in the simulation of RTM or BTM, absorption coefficient is generally employed to account for the energy decrease when ray or beam meets the surface. Absorption coefficient is easily calculated from the reflection coefficient by random incidence, but there are many ways to deduce the complex reflection coefficient from the real absorption coefficient.

3.1.2. Approximated Reflection Coefficient

For the practical purpose, in particular in the initial design stage, the reflection coefficient can be approximately deduced from the absorption coefficient under some assumptions. As a rough assumption, one can employ the real-valued reflection coefficient and the locally reacting surface. Then, the reflection coefficient simply becomes the 'angle-independent', real reflection coefficient, r_θ^i, expressed as $r_\theta^i = \pm\sqrt{1-\alpha_s}$. Here, α_s denotes the statistical absorption coefficient of the surface material under diffuse condition. Acoustically hard material is associated with the positive sign, whereas the negative value stands for the acoustically soft material.

Alternatively, an angle-dependent reflection coefficient, r_θ^d, can be also used approximately, which is obtained using the surface impedance and the radiation impedance as follows: [74]

$$r_\theta^d = \frac{Z_w - Z_r(\theta)}{Z_w + Z_r(\theta)}. \tag{3.1.4}$$

Here, Z_w means the surface impedance of the wall and Z_r the radiation impedance. The surface impedance can be calculated again from the angle-independent reflection coefficient, r_θ^i, and the equivalent radiation impedance Z_r^* of the wall material, expressed as $Z_w = Z_r^* \frac{1+r_\theta^i}{1-r_\theta^i}$. Equivalent radiation impedance is a compensation factor to match the random incidence absorption coefficient from the real reflection coefficient with the initially given absorption coefficient, α_s. For finite surfaces, $Z_r^*/\rho c$ is smaller than 1.64 and it depends on *ke*, in which *e* denotes the characteristic dimension (m) expressed as *e=4S/U*, in which *S* is the area (m^2), and *U* the perimeter (m). For infinite area and angle of incidence θ_i=60°, the normalized value of the equivalent field impedance Z_r^* should be 2. However, walls are finite, a somewhat lower value which is frequency dependent has been found for the final approximation model.

The approximated solution for the Z_r in Eq. (3.1.5) is given by

$$Z_r = \rho c\left[\left(\cos^2\theta - A\frac{2\pi}{ke}\right)^2 + B\left(A\frac{2\pi}{ke}\right)^2 + \left(\frac{2\pi}{(ke)^2}\right)^4\right]^{-\frac{1}{4}}, \tag{3.1.5}$$

where the empirical constants A and B are 0.6 and π, respectively, obtained by trial and fitting method. The Z_r in Eq. (3.1.5) differs from the numerical results within ±10% for *ke*>8 and up to ±20% for *ke*<8 [75]. One way to check the approximation when using the angle dependent reflection coefficient is to calculate the random incidence absorption coefficient by integrating over all angles of incidence according to Paris' formula as:

$$\alpha_{rand} = \int_0^{\pi/2} \alpha_\theta \sin(2\theta) d\theta, \tag{3.1.6}$$

where $\alpha_\theta = 1 - \left| r_\theta^d \right|^2$. To mach the α_{rand} with original value α_s, the equivalent field impedance should be adjusted. The test was carried out through with the values 0.2, 0.5, and 0.8 for α_s.

The equivalent field impedance is calculated as shown in Table 3.1 for the square wall with 10 *m* edge length. The result is related to an equivalent angle of incidence if the equivalent field impedance of the diffuse field is compared to the plane wave field impedance of an infinite area, i.e., $\rho c/\cos\theta$. At high frequencies and for large surface area, the value converges to 1.64, which corresponds to the incidence angle of 52.5° and thus it is somewhat smaller than the original assumption of 60°. The normalized field impedance and the reflection coefficient for a panel of 100 m^2 in area are shown in Fig. 3.1 and 3.2, respectively. It should be reminded that for the approximate reflection coefficient are based on the assumptions of local reaction and plane wave incidence, but the size effect is compensated.

3.1.3. Condition of Negative Real Part

As mentioned in the previous chapter, the real reflection coefficients can be employed in the PBTM. The most valuable merit of angle dependent reflection coefficient in Eq. (3.1.4) is the representation of the negative reflection coefficient depending on the angle of incidence. When the sound is incident from the almost grazing angle onto a soft material, the negative reflection coefficient can be observed [76]. Here, acoustically soft material or pressure-release boundary means that its surface impedance is sufficiently smaller than the radiation impedance, e.g., porous materials at high frequencies. Thus, the condition for the negative real part should be examined in this chapter. The condition for negative real part of complex reflection coefficient can be a hint. The complex reflection coefficient is expressed as follows:

$$r(\theta)=\frac{\zeta-\dfrac{1}{\cos\theta}}{\zeta+\dfrac{1}{\cos\theta}}=\frac{(R^2+X^2)\cos^2\theta-1}{\left(R\cos\theta+1\right)^2+\left(X\cos\theta\right)^2}+j\frac{2X\cos\theta}{\left(R\cos\theta+1\right)^2+\left(X\cos\theta\right)^2}, \qquad (3.1.7)$$

where normalized surface impedance, $\zeta=R+jX$, R denotes the resistance, X the reactance. In Eq. (3.1.7), the condition for the negative real part is written as follows:

$$\theta>\theta_c=\cos^{-1}\left(1/|\zeta|\right). \qquad (3.1.8)$$

The condition is only dependent on the magnitude of the surface impedance. However, this condition can not be directly adopted in the present method, because the criterion is expressed in terms of impedance. The absorption coefficients are expressed by the following equation, using Paris' formula.

$$\alpha_s=\frac{8}{|\zeta|^2}\cos\beta\left[|\zeta|+\frac{\cos2\beta}{\sin\beta}\arctan\left(\frac{|\zeta|\sin\beta}{1+|\zeta|\cos\beta}\right)-\cos\beta\ln\left(1+2|\zeta|\cos\beta+|\zeta|^2\right)\right]. \qquad (3.1.9)$$

Here, β is the phase of the surface impedance. Figure 3.3 shows the value of three terms in the square parenthesis and absorption coefficient. The value of the parenthesis is almost dominated by the 1st term, the magnitude of impedance. If the parenthesis can be substituted by $|\zeta|$, the approximated equation can be expressed as follows:

$$\alpha_s\approx\frac{8}{|\zeta|^2}\cos\beta\cdot\frac{|\zeta|}{2}=\frac{4}{|\zeta|}\cos\beta. \qquad (3.1.10)$$

There is no information on the phase, therefore the β should be ignored under the assumption of medium as follows:

$$\alpha_s\approx\frac{4}{|\zeta|}\cos\beta\approx\frac{1}{|\zeta|}. \qquad (3.1.11)$$

Therefore the criterion of negative real part for real reflection coefficient is expressed as follows:

$$\theta>\theta_c=\cos^{-1}\left(\alpha_s\right). \qquad (3.1.12)$$

The angle of zero crossing is shown in Fig. 3.5 as a function of frequency. One absorptive material was tested to check the validity of criterion for the negative real part. Material was closed cell poly-urethane (PU) foam (25 mm in thickness). Surface impedance (see Fig. 3.6(a,b)) was measured in the impedance tube of diameter 45 mm using multiple microphone method [77]. The absorption coefficient from the Eq. (3.7) was shown in Fig. 3.6(c).

The measured and calculated real reflection coefficient from the absorption coefficient was shown in Fig. 3.7. Naturally, the angle-independent reflection coefficient, r_θ^i, has a constant value for a given absorption coefficient. The angle-dependent reflection coefficient, r_θ^d, has both positive and negative values depending on the incidence angle. Although an abrupt change exists around 80° from positive to negative value, it corresponds better with the measured complex reflection coefficient. The negative reflection coefficient is important in accounting for the interference effect and it can be described by r_θ^d.

3.1.4. Test of the Approximate Reflection Coefficients

3.1.4.1. Test Room Condition

A medium sized room with absorption data was taken as a test example. Room dimensions were 6.22×5.08×3.00 m^3 as shown in Fig. 3.8. The wall absorption coefficient data are listed in Table 3.2. A wall having a door and another wall in yz-plane at (6.22, y, z) were brick walls and a wall in yz-plane at (0, y, z) had a plaster surface. The upper space of the wall in xz-plane at (x, 5.08, z) is made of glass. Source (S) and receiver (R1) were located at (1.50, 1.50, 1.10) and (1.50, 3.08, 1.27), respectively. The height of R1 position corresponded with a human sitting posture. Measurement and analysis of impulse response were conducted according to the ISO 3382 standard [78]. The maximum length sequence (MLS) signal was radiated from a dodecahedron omni-directional source and the transmitted sound was picked up using an omni-directional microphone (AKG C34).

The Schroeder cutoff frequency, f_c, of this room was calculated as 150 Hz; therefore, it is expected that the PBTM will be useful within the medium frequency range of 150-600 Hz. Because the absorption at the ceiling (acoustic tile) was large, the reflection in between the ceiling and floor was much weaker than other directional reflections. In the simulation, the number of beams was 2000 and the number of reflections was allowed up to 30 to obtain the impulse response of 1 s in duration. Both of r_θ^i and r_θ^d concepts were tested. One should remind that r_θ^d also takes the size effect of the reflecting surfaces into account.

3.1.4.2. Application of Approximate Reflection Coefficient

The early parts of pressure impulse responses for octave bands in the range of 125 Hz ~ 1 kHz are shown in Fig. 3.9. It should be recalled that 125 Hz band is lower than f_c and 1 kHz band is higher than 4 f_c; the frequency span in between two bands can be called the medium frequency range. The displayed time lengths of the impulse responses were halved with increasing the frequency by an octave to clearly demonstrate the similarity of wave forms. The predicted impulse response at 125 Hz shows some differences with the measurement. One can find that an excessive decay in the late part is introduced by employing r_θ^d. At 250 Hz, both simulations employing r_θ^i and r_θ^d show excellent correspondence with measurement. Predicted direct sound from source to receiver, which is not affected by any reflection from the wall, matches exactly with measured data. The peaks are slightly overestimated using r_θ^d, but the overall trend of the transient response is more similar to the measured response than the case using r_θ^i. When r_θ^d is employed in the simulation at 500 Hz band, a precise prediction of responses around 0.03 s was obtained in contrast to the case using r_θ^i. The overall trend of predicted impulse response corresponds to the measured data very well. In the simulation in 1 kHz band, a reasonable agreement with measurement can be seen although the frequency band exceeds the high frequency limit of applicable range. The predicted peak values of the angle-dependent case are slightly bigger than those of angle-independent case. The simulation results as shown in Fig. 3.9 reveals that the PBTM using real reflection coefficient can be a very useful mid frequency predictor for the pressure impulse response in an enclosed room. One can also find a possibility for the extension of the applicable range at low and high frequency ends, if some error can be accepted in an engineering sense.

The pressure impulse response cannot be obtained from the beam tracing method. Therefore, energy impulse responses, which can be calculated by squaring a pressure impulse response, computed from BTM and PBTM were compared with the measured data as shown in Figs. 3.10 and 3.11, for 250 Hz and 500 Hz band, respectively. Significant differences can be observed between PBTM and BTM results. The predicted energy impulse responses by using BTM usually show monotonic decay, because energy of the reflected beam is smaller than that of a direct sound. The results by using PBTM show a good agreement with measured data, especially when r_θ^d is used. Although not shown here for brevity, it was also observed that the predicted energy impulse responses by using both methods become similar at 1 kHz, which is beyond $4f_c$.

Reverberation times (EDT, T30), Definition (D50, D80), Clarity (C80), and center time (Ts) [78] were calculated from the simulated and measured impulse responses. In estimating EDT, the PBTM using r_θ^d yields an excellent agreement with measured data, whereas the other predictions seem to be slightly different as shown in Fig. 3.12. This means that the initial part of impulse response is accurately predicted by employing the PBTM, which clearly show the angle-dependent acoustic characteristics of walls. In the results of T30 and D50 calculations, both BTM and PBTM show good agreements with measured data. It is noted that the predicted parameters agree well with measured data, although the energy impulse response by using the BTM is clearly different. D80 data shows a distinguishable difference between BTM and PBTM. D80 by using BTM is underestimated regardless of frequency while D80 values by using PBTM show a good agreement irrespective of the types of reflection coefficient. Similarly, in C80, one can clearly observe that the PBTM result shows better correspondence with measurement. Results by using BTM are underestimated because of the reverberation after 80 ms, while the measured data and PBTM results display little reverberation components in Figs. 3.10 and 3.11. The reason why C80 shows a bigger error than D80 comes from the definition. The higher the D80, the smaller the late energy after 80 ms. In the definition of C80, the small late energy is a denominator. For example, the 5% variation of D80 value of 0.9 (from 0.855 to 0.945) causes more than 20% difference in C80 (7.7 dB to 12.35 dB; original C80 is 9.54 dB). For the D80 value of 0.8, the difference becomes smaller, but still the variation is larger than 12%.

It is hard to predict the Ts, because the overall shape of the predicted transient response should correspond well with the measured data. The predicted data by PBTM are smaller than the measured data due to a small overestimation in the early part before 20 ms at 500 Hz and 1 kHz bands, while the BTM prediction yields an overestimated data.

The other two receiver positions, R2 (4.72, 3.58, 1.27) and R3 (4.72, 1.5, 1.27) as shown in Fig. 3.8 were also tested. These two additional points have the same height as the former receiving position, R1. Because the main purpose of this study was to test a new method for the prediction of the impulse response more precisely than before, the study was focused on the human hearing position in the chamber, thus the receiver height was determined as 1.27 m in a sitting posture. The three receiving points were selected to have some meaning, though. R1 was a point near to the source and near to the yz-plane; R2 was a point far from the source in a diagonal way and it is very near to the glass window in xz-plane; R3 was a point far from the source and its distance from the xz-plane was the same with the source point, which was located at a nearly symmetric position in x-direction. One-dimensional reflections along x direction and y direction should have been dominant at R3 and R1, respectively, whereas the result at R2 was not strongly influenced by such one-dimensional reflection. In Fig. 3.13, the measured and calculated pressure impulse responses at R2 in medium frequencies are shown. The peaks in the pressure impulse response are slightly shifted in the early parts of the impulse response due to the incorrect phase shift at the wall by employing the real reflection coefficient and some diffraction effect near the HVAC system than other receiving points. Figure 3.14 shows a comparison of measured and calculated acoustic parameters at R2. All simulation results, including the data calculated in 1 kHz octave band which can be considered as high frequency, show a reasonable agreement with measurement. It is noted that the center times using the BTM were clearly smaller than the measured data. This was resulted from the monotonic decaying characteristic of BTM result. In 250 Hz and 500 Hz bands, the calculated center times using the PBTM were larger than those calculated by using the BTM and they correspond better with measured data than the BTM.

Figure 3.15 and 3.16 show the comparisons of pressure impulse response and acoustic parameters at R3. In Fig. 3.15, calculation method using r_θ^d yielded better results than using r_θ^i, especially in 500 Hz octave band. Also, C80 and center times computed from the PBTM at medium frequencies corresponded better with measured data. It should be mentioned that the D50 values are overestimated by employing the BTM, because of the monotonic decrease of the energy impulse responses: sound energy is concentrated on the early part of the IR. The same thing happens in the estimation of C80 and center time; the larger C80 value and smaller center times.

At 1 kHz which is higher than the high frequency limit of PBTM application, it is observed that all acoustic parameters obtained by PBTM using the angle-dependent reflection coefficient agreed very closely with measured data compared to the BTM, except EDT, T30 only at R3 position. When the scattering is not severe in a room, the high frequency response can be accurately predicted by the present method.

3.1.5. Comparison Between Complex and Real Reflection Coefficient

In this chapter, the results from the complex reflection coefficient and real reflection coefficients were compared. As a test example, a medium sized room was chosen from Suh and Nelson's work [25]. Walls and ceiling were made up of plaster and concrete and the absorption coefficients are 0.08 and 0.02, respectively. The plaster and concrete are assumed as acoustically hard walls, therefore assumption for the real reflection coefficients are acceptable. Floor is covered by a carpet and they measured the surface impedance in an impedance tube. A comparison between the phased geometrical acoustics methods and the measurement was shown in Fig. 3.17. Figure 3.17(a) shows the phased beam tracing result with 2000 beams and Fig. 3.17(b) shows the phased ray tracing result with same number of rays and the radius of the spherical receiver is 1 m, which seems to be the most proper receiver size. In Fig. 3.17(a), the second peak around 0.02 s is delayed a little bit, but phased BTM result in Fig. 3.13(b) shows a good correspondence in the peak and through location. Especially the early part of the impulse response shows almost perfect match with measurement. Even for the late reflection around 0.07 s, the peak position is well matched with measurement. From the Fig. 3.17, the precision of the PBTM using complex reflection coefficient was validated.

Here, two types of real reflection coefficients which were adopted in the previous chapter were tested. Figure 3.18 shows comparisons of impulse response by using the approximate real reflection coefficients, r_θ^d and r_θ^j, and the complex reflection coefficient. In Fig. 3.18, the peaks are exaggerated when the real reflection coefficients are involved. Figure 3. 18(c) incorporates the r_θ^d scaled by a correction factor of 0.8, shows reasonable agreement with complex reflection coefficient. The correction factor could be introduced depending on the impedance of the surface; as the wall becomes acoustically soft, the small value of correction factor could be adopted.

The overestimation of peaks comes from the exaggerated real part of reflection coefficient owing to the neglect of imaginary part. From the relationship between the absorption coefficient and the impedance, sometimes called "circles of constant absorption" [62], it can be explained that the neglect of imaginary part overestimates the real part of reflection coefficient.

In Fig. 3.19, zero imaginary part significantly exaggerates the *negative* real part of reflection coefficient while the magnitude of positive real reflection coefficient is comparable to the complex one. Therefore the peaks are more distinguished than those from the complex reflection coefficient. The reason for the overestimated negative real part is due to the sudden change from the positive value to negative shown in Fig. 3.7 (the abrupt change around 80° from 0.8 to -0.8).

3.1.6. Stepwise and Continuous Reflection Coefficient

So far, the stepwise reflection coefficients have been employed in the simulation. In an actual situation, the reflection coefficient or absorption coefficient should be smoothly and continuously changed with respect to the frequency. In a practical situation, a frequency-averaged absorption coefficient for each octave band is initially given. Because the reflection coefficient, which is deduced from the absorption coefficient, should be constant in a band, the reflection coefficients are expressed as the step-wise functions.

In this chapter, effects of the step-wise reflection coefficient were investigated in the comparison with the continuous reflection coefficient. The frequency averaged reflection coefficient in a band is assumed to be the value at the center frequency. Then the reflection coefficients can be linearly regressed. The room in Fig. 2.13 was chosen as a test example and the absorption coefficients used in the simulation are tabulated in the Table 3.2. The stepwise and continuous absorption coefficients of the ceiling are plotted in Fig. 3.20. In Fig. 3.21, the results do not differ much in both the magnitude plot of transfer function and impulse response. It might be due to the small change between the neighboring absorption coefficients from 0.4 to 0.65 in the wide frequency range from 125 Hz to 1 kHz.

Consequently the reflection coefficient varying from 1 to 0.3 is artificially assigned to the ceiling and it is illustrated in Fig. 3.22. As a result, the transfer functions differ distinguishably near troughs, but the impulse response are almost the same. The change in the reverberation time between two results is only 0.1 s, which differs just by 1.5%. These two examples clearly demonstrate the validity of using step-wise reflection coefficient and hereafter the step wise reflection coefficient will be involved in the foregoing simulation.

3.1.7. Spherical Wave Reflection Coefficient

Use of the plane wave reflection coefficient may cause some errors in evaluating the acoustics of fairly small room. If the room is quite large, the source and receivers are normally distant from each other, but in a small room, the source-receiver locations are close. There have been several studies of pointing out the discrepancy when the plane wave reflection coefficient is involved [22,51,79]. It becomes increasingly inaccurate at low frequencies. Practically one never has plane waves and there are limitations to the applicability of the Eq. (3.1.3). First, regardless of the relative magnitude of the impedance at grazing incidence, reflection coefficient becomes -1, which means the reflected wave is equal in magnitude and 180° out of phase with the incident wave. Thus the reflected wave completely cancels out the incident wave and there is no energy propagation along the boundary. This is called as the grazing incidence paradox for plane wave. This paradoxical result indicates qualitatively the difficulty of realizing plane wave condition at a boundary at angles near grazing. The same problem has arisen in the electromagnetic theory and Sommerfeld attacked the problem first in 1909. The spherical wave reflection has been discussed by many researchers [51,72,73,80-82]. The spherical wave reflection coefficient is given by

$$r_s = r + (1-r)F(w_n)\,. \tag{3.1.13}$$

The term *F(wn)*, known as the boundary loss factor [51] or residual term caused by the sphericity of the wave, is expressed as follows:

$$F(w_n) = 1 + j\sqrt{\pi}\, w_n e^{-w_n^2} erfc(-jw_n)\,, \tag{3.1.14}$$

with the parameter w_n which is known as the numerical distance, defined by

$$w_n = \sqrt{kd_n/2}\,(1+j)\left(\cos\theta + \frac{1}{\zeta}\right). \tag{3.1.15}$$

where d_n is the distance from the source to receiver (m). For the grazing incidence with *large impedance* of the surface or *small* kd_n (consequently w_n will be small), $F(w_n)$ approaches unity. So the reflection coefficient no longer becomes -1, irrespective of reflection coefficient. In other limiting case, that for *higher frequencies*, *longer distance* and *smaller surface impedances*, w_n gets much larger than unity and the $F(w_n)$ goes to zero. Thus the spherical wave reflection coefficient reduces to plane wave one. Ingard [73] found the identical result for the image source strength to that given in Eq. (3.1.13) when considering the locally reacting case, however the numerical distance reduced to

$$w_n = \frac{1}{2} ikd_n \frac{\left(\cos\theta + \frac{1}{\zeta}\right)^2}{\left(1 + \cos\theta \frac{1}{\zeta}\right)}. \tag{3.1.16}$$

The result shows that the error at normal incidence is smaller for a hard wall than for a soft one, whereas the opposite is true for angles near grazing. Approximately for angles larger than 80°, the plane wave condition can not be maintained [73].

Comparisons between the plane wave reflection coefficient and the spherical wave reflection coefficient are shown in Fig. 3.24 and Fig. 3.25. One more reflection coefficient is added in the comparison which is expressed as

$$r_{finite} = \frac{Z_w - Z_r(\theta)}{Z_w + Z_r(\theta)}. \tag{3.1.17}$$

In this reflection coefficient, the finite size effect is considered by introducing the Z_r, which was already mentioned in Eq. (3.1.5). The approximate radiation impedance also prevents the pressure reflection coefficient to be -1, although the sound is incident grazingly. In this case the surface area is set to 10 m^2. The spherical wave reflection coefficient is based on the fact that the residual term, caused by the sphericity of the wave, makes the reflection coefficient not to be -1, but the size compensated reflection coefficient assumes that the radiation impedance does not goes to infinity because of the finiteness of the panel.

In Fig. 3.24, when the sound is grazingly incident onto the surface, the discrepancy was found whereas insignificant difference was shown when the angle of incidence is 45°. In addition, when the surface becomes softer, the spherical wave reflection coefficient shows a good agreement with the plane wave reflection coefficient. For the hard surface, the spherical wave reflection coefficient at low frequency notably differs from the plane wave reflection coefficient. Especially after 80°, the plane wave reflection coefficient does not work properly as can be seen in Fig. 3.25. The reflection coefficient of Eq. (3.1.17) shows a slight difference with the spherical wave reflection coefficient, but they play the same role to prevent the excessive negative reflection coefficient.

3.2. Application Example of Conference Room

3.2.1. Binaural Simulation Using the HRTF

Binaural simulation is a method of making binaural signals at receiver's both ears in non-existing spaces by means of a computer model. In recent days, simulation of listening impressions becomes more and more important for the acoustical design of an enclosed space such as concert hall and theater, etc. There are lots of binaural simulation techniques in combination with the computational method and the domain where the calculation is performed. In most cases, the geometrical acoustics techniques such as the mirror image source method [8], the ray tracing method, and hybrid method have been employed [83-85]. Modal methods such as the FEM, BEM and FDM can be adopted in the binaural simulation. However, they have a practical limitation of exponential growth of computation load. Besides, the handling of source directivity is tricky [86]. Also the radiosity [87-89], in which the boundary is pre-divided into surface patches that do not need to be smaller then the wavelength [86], can be an alternative. This method has a significant advantage which is opposite to the geometrical acoustics that the diffuse reflection, typically Lambert directivity [62], is easy to implement. Unfortunately, because the specular reflection can not be handled with using this method, the decomposition of reflected sounds is almost impossible. Therefore the radiosity is not a proper solution for the binaural simulation. To the end we applied the phased beam tracing method owing to the easy decomposition of sound field and fast calculation.

Although it is impossible to simulate an actual sound field accurately by using the geometrical acoustics methods, the previous works have been successful and some of them have been already commercialized. The great advantage of geometrical acoustics technique compared to modal method is the simple and easy decomposition of reflections toward the receiver. Also, the limited spatial resolution of human auditory system [90] can make the binaural simulation successful by means of geometrical acoustics method [83-85,91]. Once the distribution of image sources is quantized, the binaural simulation can be carried out by convolving with HRTF. Traditionally the generation of reverberation part was not feasible due to the practical limitation of computer speed, therefore the reverberation was treated by stochastic methods in room acoustics.

The binaural simulation can be carried out both in time and frequency domain. The previous methods mostly have employed the time domain calculation, because the result by using the geometrical acoustics methods is an energy reflectogram in the time domain. In order to create binaural signals from the reflection data, an appropriate impulse response filter is necessary to represent the octave band, and then convolved with the corresponding HRTF. The well-known commercial software ODEON uses infinite impulse response filter of Kaiser-Bessel type to make the room impulse response and binaural signals [91]. In the superposition of reflections, the phase shift can be considered. Finally each binaural reflection filter is located at the appropriate time of arrival, τ_i.

Martin and Vian have studied binaural sound simulation in the frequency domain by using the cone tracing method [92]. The elementary filters are source filter, material filter, air absorption filter and so on. The reflection filters are calculated by using the cone tracing method. The ear filters were measured. They computed the elementary filters for each path i with associated delay τ_i. Then two impulses for both ears were calculated by the inverse Fourier transform.

Finally, the global responses were synthesized by summing over all the paths expressed as follows:

$$R(t)=\sum_i R_i\left(t-\tau_i\right),\ L(t)=\sum_i L_i\left(t-\tau_i\right). \tag{3.2.1a,b}$$

Here, $R(t)$ and $L(t)$ are the signals at both right and left ears, respectively. τ_i is the delay time of each reflection. In both methods, the associated delay time τ_i is always crucial information to make the correct binaural signals.

The generation of the late part of room response such as reverberation tails is still a problem to be solved due to the heavy computation effort. Traditionally reverberation is treated by stochastic method in room acoustics. Martin and Vian also have suggested a new binaural reverberation process by dividing a pressure impulse response into three parts depending on the order of reflections [93,94]. The first deterministic part is calculated by the geometrical approach, usually restricted to 6th order, and second and third parts are simulated by the pseudo random and random process, respectively. The transition between the exactly and stochastically simulated parts of room responses are still the disputable point. On the contrary, the recent research by Summers asserted that the direct calculation of late reflections improve the accuracy in the medium frequency range [95].

3.2.2. Suggested Method

The PBTM is different from the conventional geometrical acoustics method in terms of the calculation domain. The main calculation is carried out in the frequency domain to calculate the steady-state transfer function and impulse response can be obtained by taking the inverse Fourier transform. This feature makes the binaural simulation fast because the convolution with HRTF is a simple multiplication in the frequency domain. The convolution is carried out for each arriving beam, one by one, and convolved transfer functions are summed into a final frequency response function. During the process, the aforementioned delay time, τ_i is not concerned, but automatically reflected because the phase information is retained and gives the information of distance from the source to receiver in the room transfer function. In the simulation of the impulse response at a receiver location, transfer functions from all directions are summed into a overall transfer function. On the contrary, to perform the binaural simulation, all reflected components should be decomposed and convolved with the corresponding HRTF which was measured in an anechoic chamber. For example, reflected sound which is incident from the front direction should be convolved with the HRTF measured when the source is located at the same point of reflection. Then the convolved transfer function can be inverse Fourier transformed into an impulse response at each ear position as shown in Fig. 3.26. The convolution process in the frequency domain is much faster than that in the time domain. The feature that main calculation is performed in the frequency domain readily facilitates the signal processing.

The other key to succeed in the binaural simulation is the precise measurement of HRTF. A transfer function for one reflection is convolved with the corresponding HRTF having the same angle of incidence. Martin and Vian measured the HRTF by employing the time delay spectrometry (TDS) based on the frequency sweeping which allows to separate one peculiar path [92]. The source was 3 m apart from the head and the measurement positions are located with a step of 30° in elevation angle and 15° in azimuth direction The electret microphones capsules placed in the ear carnal entrance and the sampling frequency was 20 kHz and the number of samples was 512 [93]. In this simulation, the HRTF data set of B&K HATS was measured using the random noise at every five degrees, 1 m apart from the sound source [96]. The sampling frequency was 44.1 kHz and the number of time samples was 512. It should be noted that the elevation angle changes from -35° to 90° owing to the restriction of measurement equipment. Then, the sound incident below the -35° in elevation angle was assumed to be incident from the -35°. Even though the HRTF data for the reflected sound from the bottom have not been precisely measured, one can guess the simulation accuracy would not be degraded significantly. The sound components from the positive elevation angle are much more predominant than those from the negative elevation angle.

3.2.3. Simulation Result

One conference room was chosen as a test example of the suggested binaural signal processing. The shape of the room is displayed in Fig. 3.27 and absorption coefficient used in the simulation is tabulated in Table 3.3. Four octave band responses from 125 Hz to 1 kHz ware calculated and compared with the measurement. The Schroeder cutoff frequency is 289 Hz, therefore 250 Hz and 500 Hz octave bands are medium frequency ranges. In the measurement, B&K HATS dummy head (type 4128) and B&K Nexus power supply (type 2690) were used. DIRAC software (type 7841) was employed to save the measured impulse response of 2 s long as using the maximum length sequence (MLS) signal. In measuring the impulse response at the head center, 1/2″ B&K microphone (type 4180) was used, which is the same type with the microphones installed in B&K HATS' ear positions, to remove the variation due to microphone characteristics.

Above all, the room impulse responses at the head center from the measurement were compared with those using the phased beam tracing method. This procedure can confirm the validity of the phased beam tracing method. Figure 3.28 shows the comparisons between two impulse responses from 125 Hz to 1 kHz. The impulse response in 125 Hz octave band shows a poor correspondence compared to other frequency bands. 125 Hz octave band response, where the frequency range is below the Schroeder cutoff frequency, may not be accurately solved by the geometrical acoustics method. Even though 250 Hz octave band is in-between the low and medium frequency range, the accuracy of room impulse response seems acceptable.

The binaural impulse responses at both ears from 125 Hz to 1 kHz octave band are shown in Fig. 3.29 Although 250 Hz octave band is in-between the low and mid frequency range, the trend in the early part is very similar to the measured data. The response over 500 Hz octave band, the simulated impulse response shows good correspondence with measurement. The accuracy of binaural signals is connected with that of impulse response at the head center. Over 250 Hz octave band, the results were well matched with measured data. The accuracy of binaural simulation result in 125 Hz octave band was degraded due to the incorrect prediction of impulse response at the head center.

The errors in the binaural simulation are discussed here. The PBTM is also a kind of the geometrical acoustics in that the principal assumptions of geometrical acoustics still hold, even though the phase information is retained. Therefore the low frequency response without considering diffraction and other wave phenomena may be inaccurate. Second, the differences may come from the improper determination of absorption coefficient, and consequently the incorrect reflection coefficients are used in the simulation. In this simulation, the angle-independent reflection coefficient is used in characterizing the acoustic property of the wall. In addition, measurement error of HRTF can cause some errors in the binaural outputs. In conclusion, the frequency domain binaural simulation by using the phased beam tracing method was suggested and applied to the meeting room. Frequency domain calculation facilitates the binaural simulation. The direct sound and early parts of the impulse response at the head center match well with those of measurement beyond 250 Hz octave band. Also in the binaural signals, the accuracy is satisfactory except for 125 Hz octave band mainly due to the accurate simulation of room transfer function by using the phased beam tracing method.

For auralization, one bassoon sound was convolved with the simulated and measured binaural impulse responses. Because the loudest frequency range of bassoon sound is distributed from 125 Hz to 1 kHz, this sound sample might be an appropriate demonstration example. In this study, subjective test was not carried out, but subjective test for several sounds from low frequency sample to high frequency sample can be very interesting for further study.

Table 3.1. Equivalent field impedance for a panel of 100 m^2 in area.

Frequency (Hz)	Z_f^*
125	1.46
250	1.60
500	1.63
1000	1.64
2000	1.64
4000	1.64

Table 3.2. Absorption coefficients of the test room surfaces.

Surface and material	Octave-band center frequencies (Hz)			
	125	250	500	1k
Wooden floor	0.15	0.12	0.11	0.10
Absorptive ceiling	0.60	0.72	0.78	0.82
Brick wall	0.01	0.02	0.03	0.04
Glass window	0.10	0.08	0.05	0.04
Gypsum wall	0.15	0.11	0.08	0.08
Ventilation grating	0.40	0.50	0.50	0.60

Table 3.3. Absorption coefficients used in the simulation.

Surface	Material	125 Hz	250 Hz	500 Hz	1 kHz	2 kHz	4 kHz
Floor	Tile	0.04	0.04	0.03	0.03	0.03	0.03
Ceiling	Gypsum	0.2	0.15	0.07	0.04	0.03	0.03
Wall with door	Concrete and wood	0.08	0.06	0.06	0.03	0.03	0.02
Wall with Whiteboards	Concrete and plastic	0.04	0.04	0.03	0.03	0.03	0.02
Window	Glass	0.1	0.1	0.04	0.04	0.03	0.03
Ventilation grating		0.5	0.5	0.4	0.3	0.3	0.3
Panel	Steel	0.3	0.15	0.1	0.05	0.05	0.04
Wall	Concrete	0.04	0.04	0.03	0.03	0.03	0.02

.

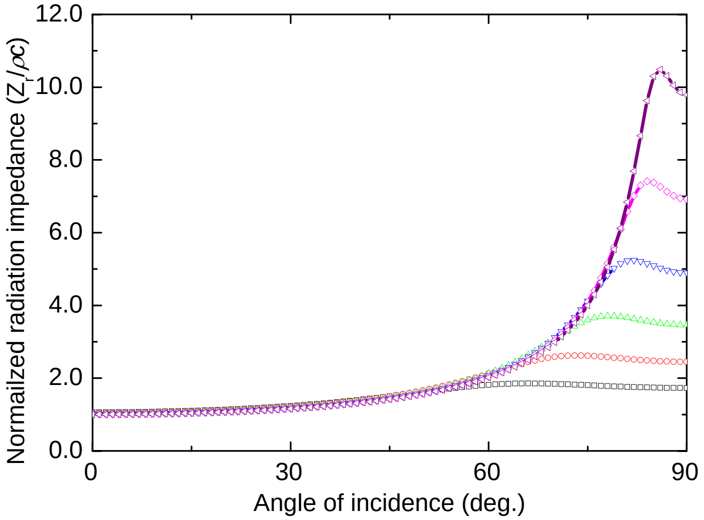

Fig. 3.1. Normalized radiation impedance for a panel of 100 m^2 in area. —□—, 125 Hz; —○—, 250 Hz; —△—, 500 Hz; —▽—, 1 kHz; —◁—, 2 kHz; —◇—, 4 kHz.

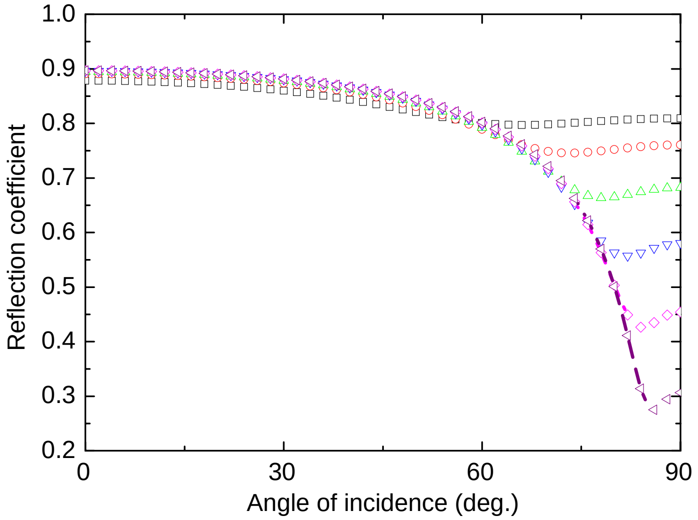

Fig. 3.2. Angle-dependent reflection coefficient for a panel of 100 m^2 in area. —□—, 125 Hz; —○—, 250 Hz; —△—, 500 Hz; —▽—, 1 kHz; —◇—, 2 kHz; —◁—, 4 kHz.

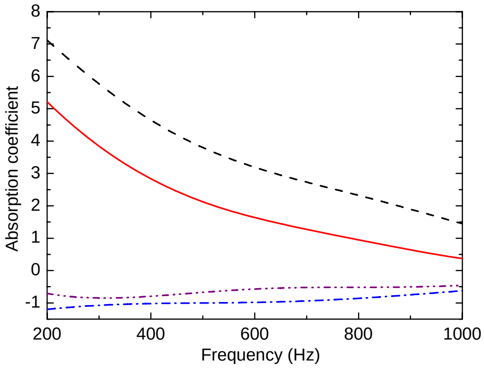

Fig. 3.3. The values in the parenthesis in Eq. (3.1.9). ——, Total; – – –, first term; ▬ • ▬, second term; – • • –, third term.

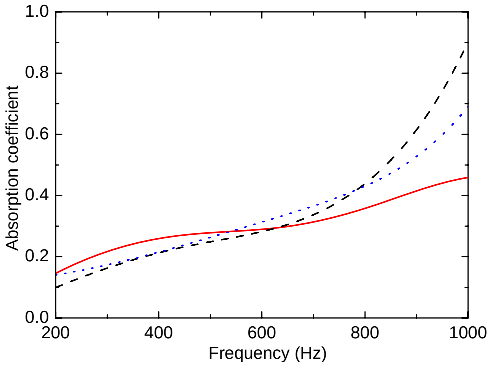

Fig. 3.4. A comparison of absorption coefficient. ——, Eq. (3.1.9); – – –, Eq. (3.1.10); • • • •, Eq. (3.1.11).

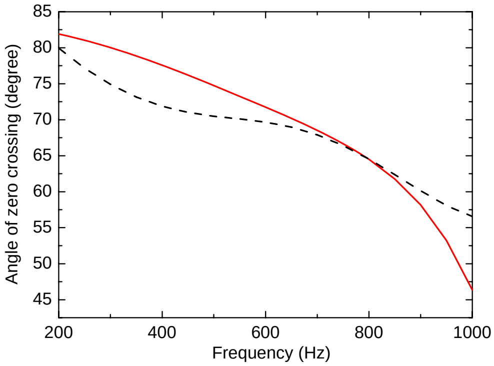

Fig. 3.5. A comparison of Angle of zero crossing as a function of frequency. ——, Eq. (3.1.8); – – –, Eq. (3.1.12).

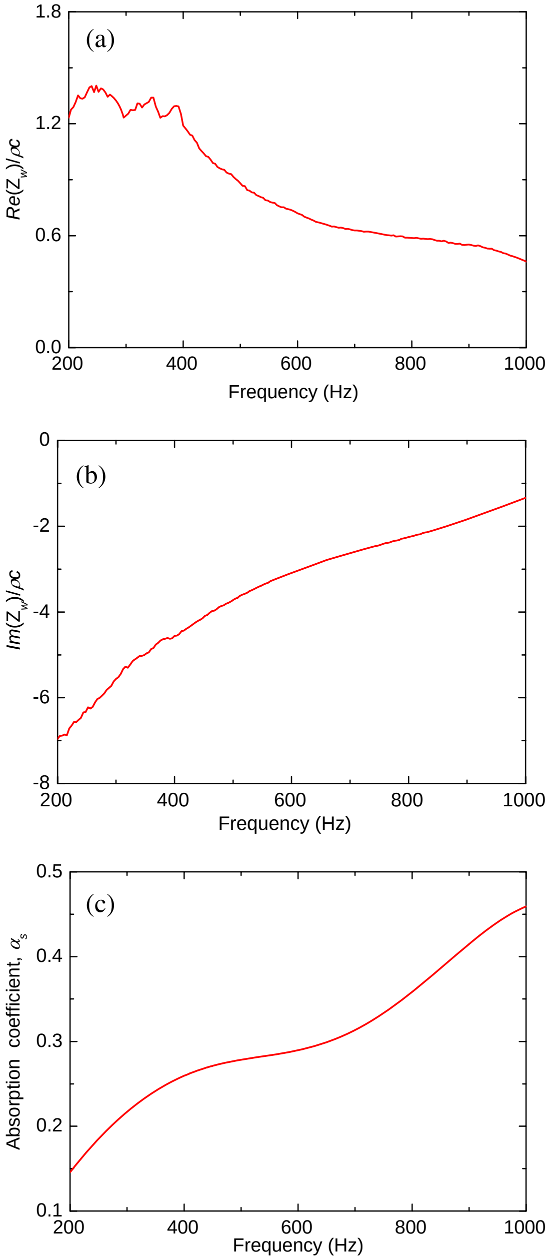

Fig. 3.6. Measured surface impedance and corresponding absorption coefficient. (a) Real part of surface impedance, (b) imaginary part of surface impedance, (c) calculated absorption coefficient.

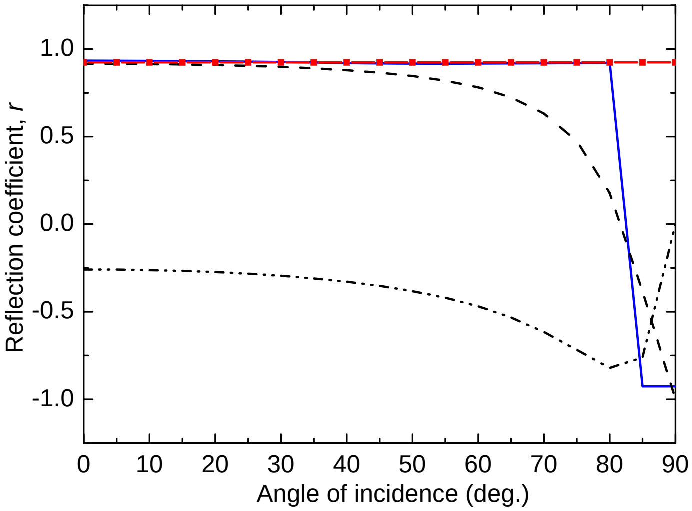

Fig. 3.7. A comparison of measured and calculated reflection coefficients as a function of incidence angle (200 Hz). — — —, Real part of directly measured *r*; ▬ ▪ ▪ ▬, imaginary part of directly measured *r*; —■—, r_θ^i; ———, r_θ^d. The test sample was 20 mm thick PU form (Z_w = 511-2881j, α_s= 0.15 at 200 Hz).

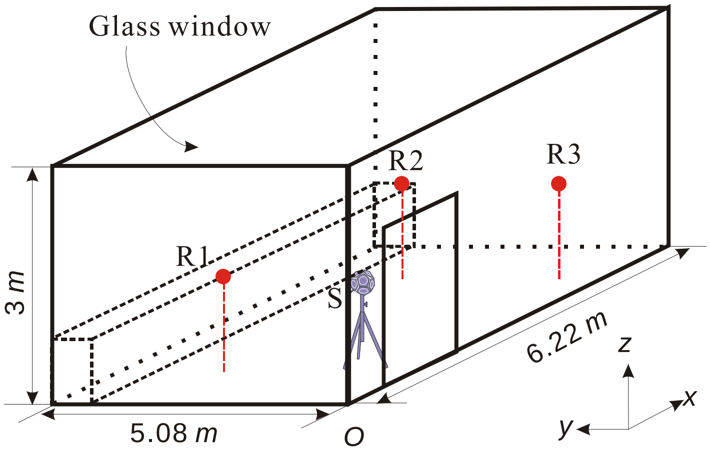

Fig. 3.8. Geometry and dimensions of the test room. Acoustic properties of surfaces are specified in Table 3.2.

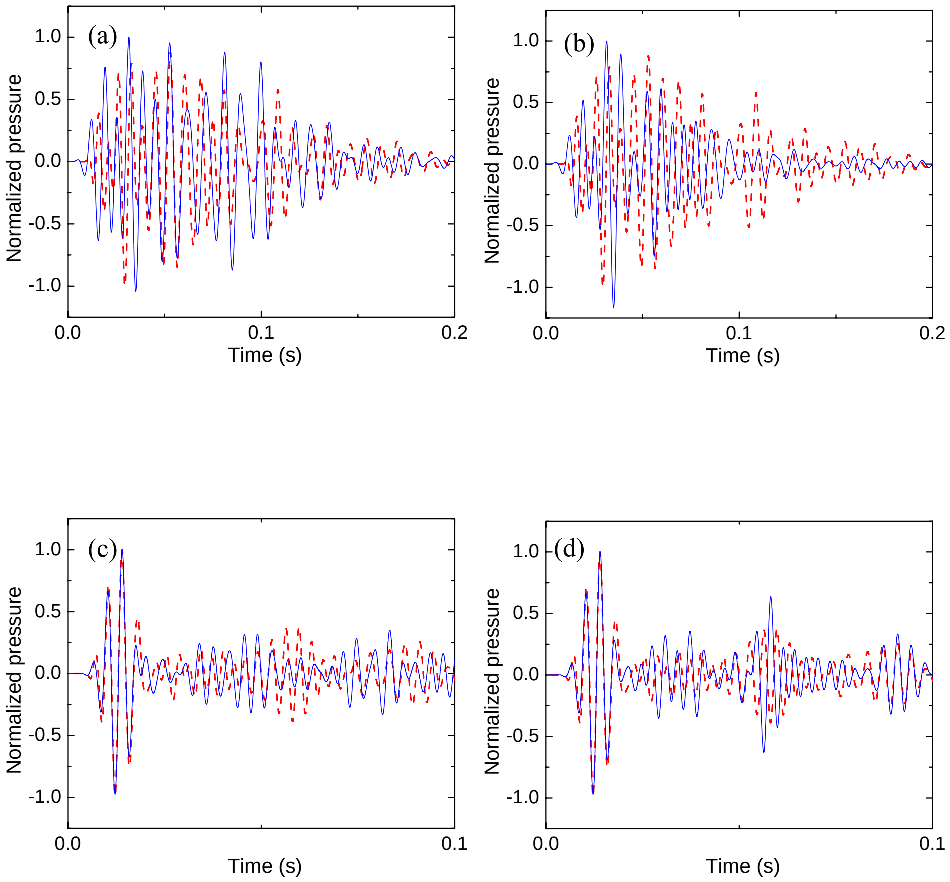

(Fig. 3.9 continued)

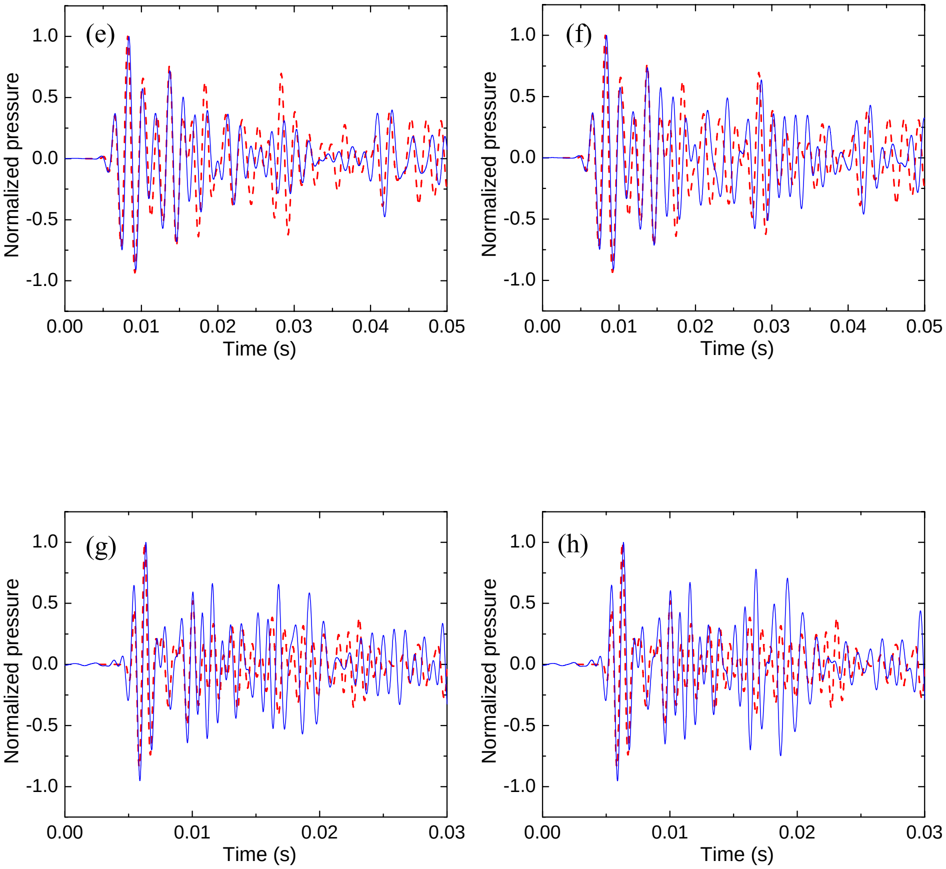

Fig. 3.9. A comparison of measured and calculated pressure impulse responses (R1). – – –, Measurement; ——, calculated by PBTM. (a), (b) 125 Hz; (c), (d) 250 Hz; (e), (f) 500 Hz; (g), (h) 1 kHz. (a), (c), (e), (g) Use of r_θ^i; (b), (d), (f), (h) use of r_θ^d.

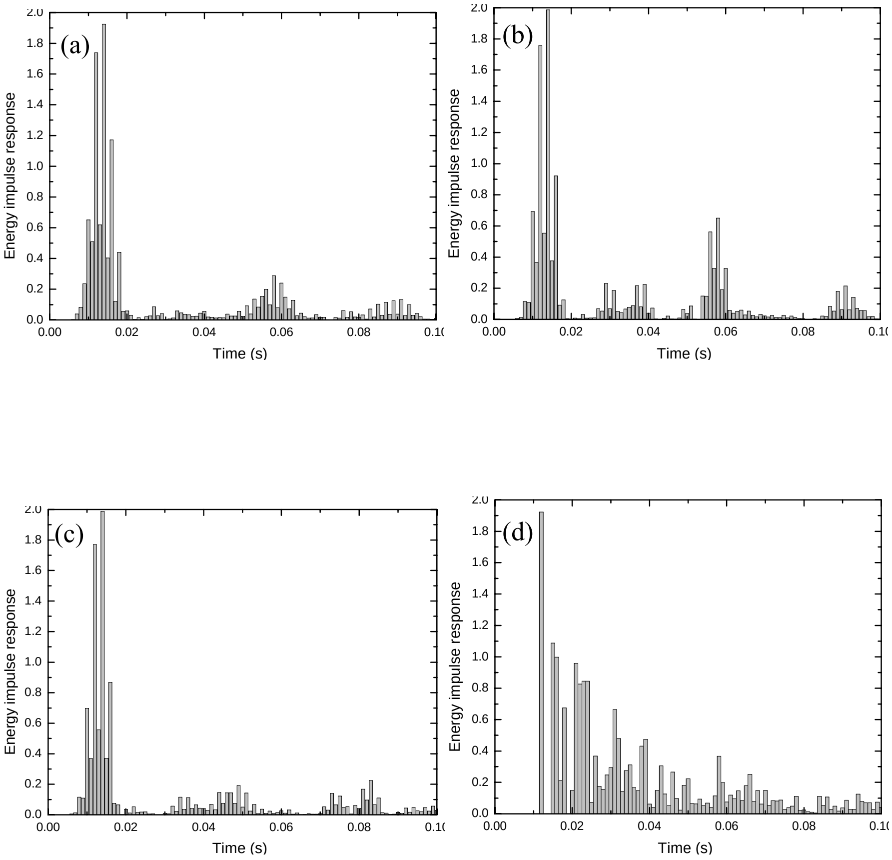

Fig. 3.10. A comparison of measured and calculated energy impulse responses at 250 Hz. (a) Measurement, (b) PBTM using r_{θ}^{d}, (c) PBTM using r_{θ}^{i}, (d) BTM.

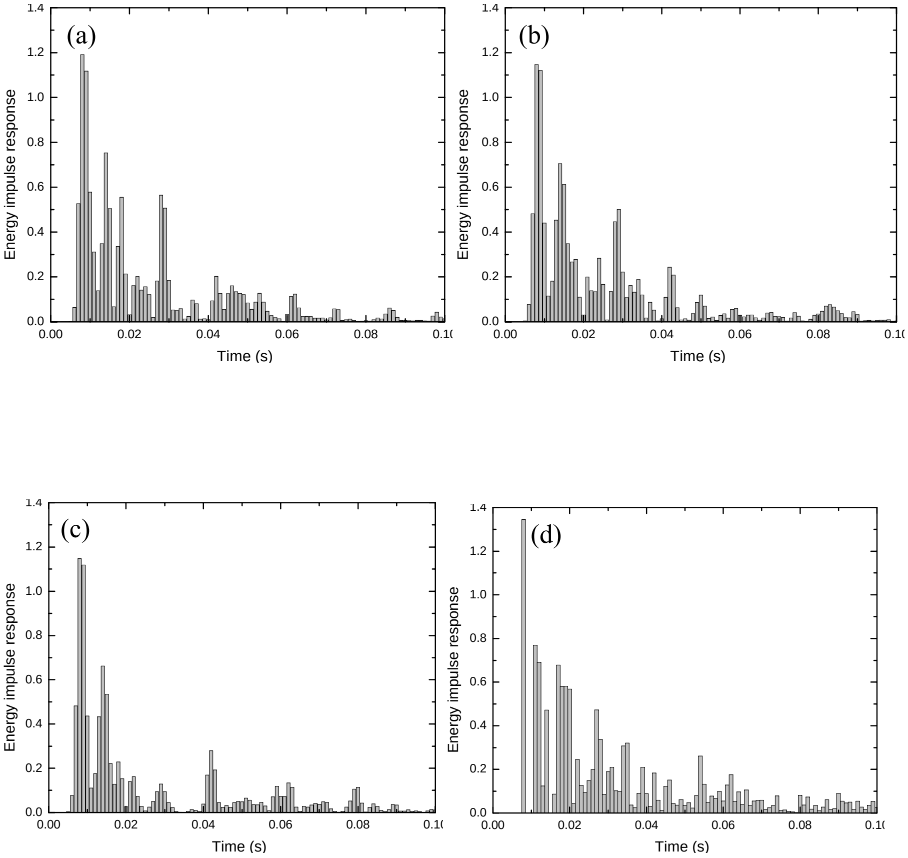

Fig. 3.11. A comparison of measured and calculated energy impulse responses at 500 Hz (R1). (a) Measurement, (b) PBTM using r_θ^d, (c) PBTM using r_θ^i, (d) BTM.

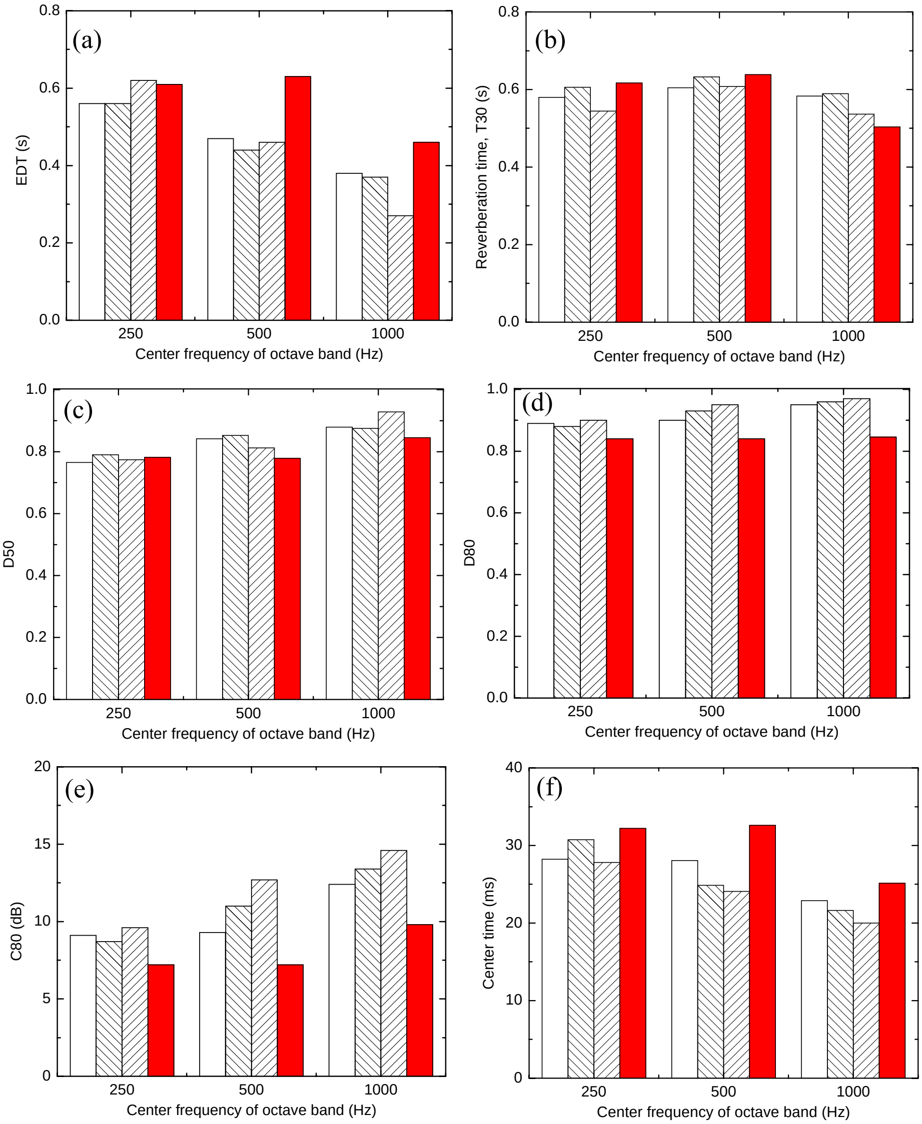

Fig. 3.12. Comparisons of measured and calculated room acoustic measures (R1). (a) Early decay time (EDT), (b) Reverberation time (T30), (c) Definition (D50), (d) Definition (D80), (e) Clarity (C80), (f) center time (Ts). ☐, Measurement; ▧, PBTM using r_θ^d; ▨, PBTM using r_θ^i; 🟥, BTM.

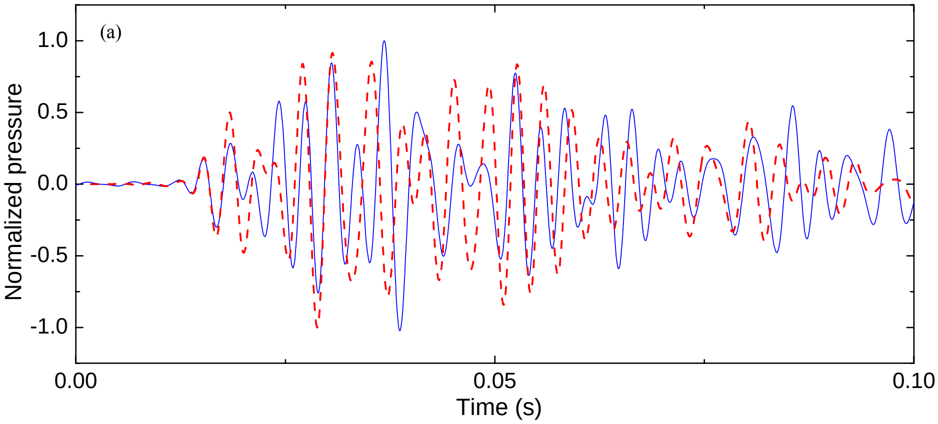

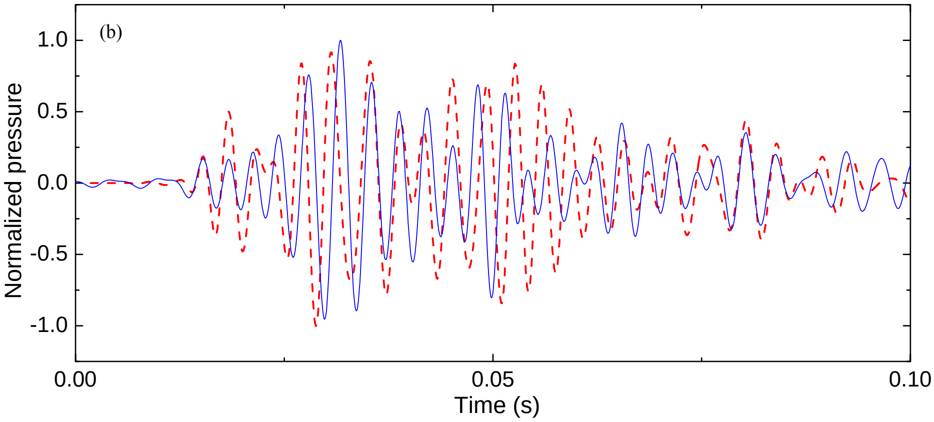

(Fig. 3.13. continued)

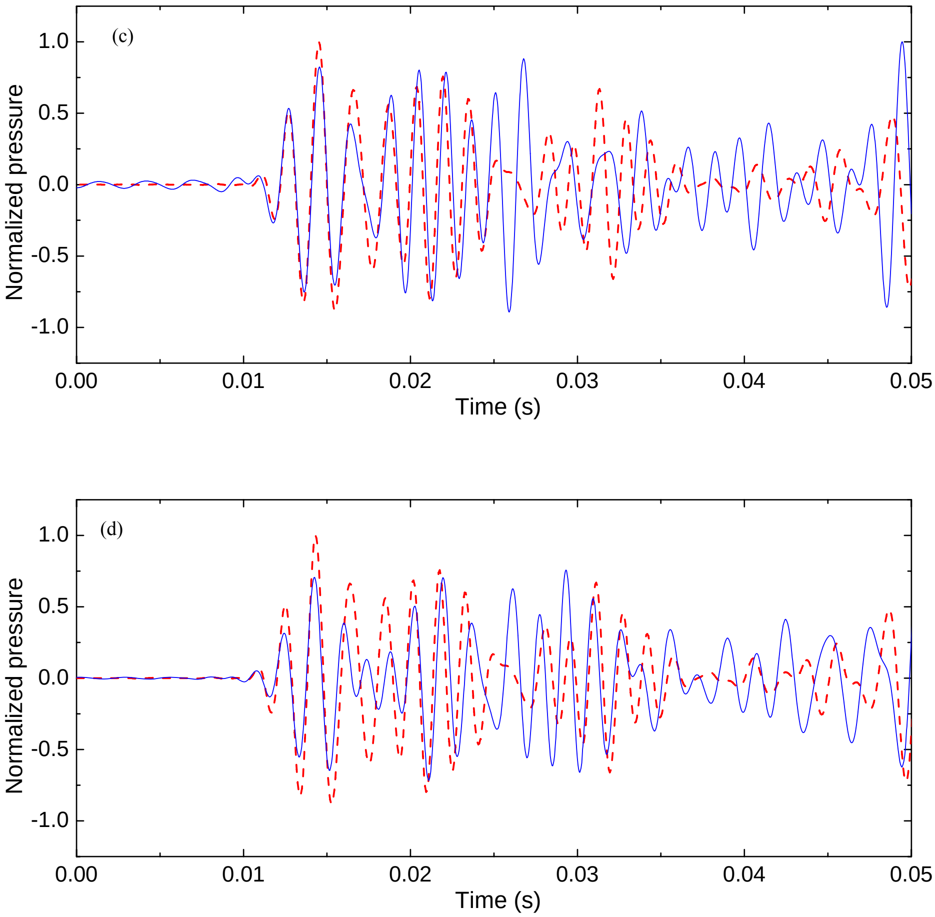

Fig. 3.13. A comparison of measured and calculated pressure impulse responses (R2 position): – – –, measured; ——, calculated by PBTM. (a), (b) 250 Hz; (c), (d) 500 Hz. (a), (c) Use of angle-independent reflection coefficient r_{θ}^{i}; (b), (d) use of angle-dependent reflection coefficient r_{θ}^{d}.

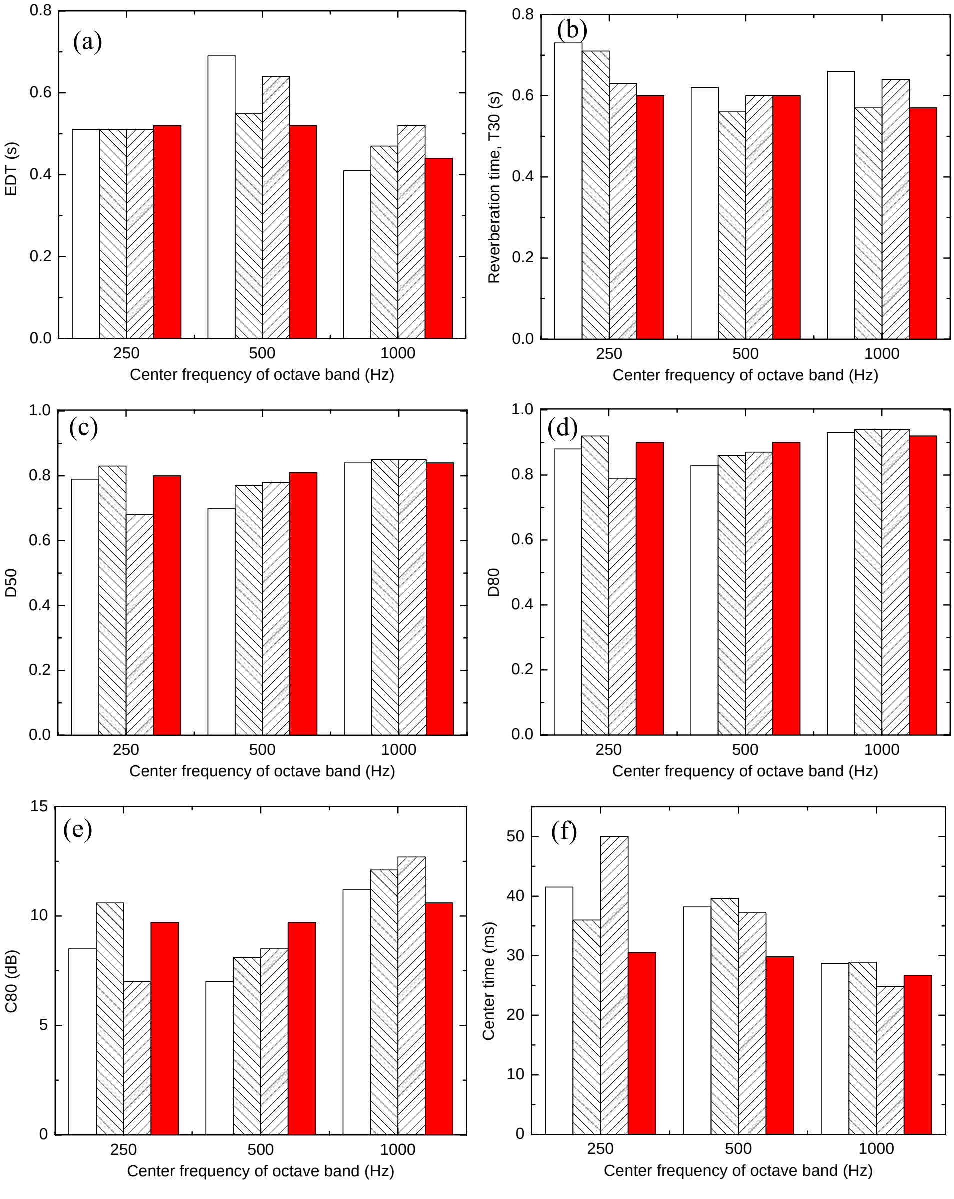

Fig. 3.14. A comparison of measured and calculated room acoustic measures (R2). (a) Early decay time (EDT), (b) Reverberation time (T30), (c) Definition (D50), (d) Definition (D80), (e) Clarity (C80), (f) center time (Ts). ☐, Measurement; ▧, PBTM using r_θ^d; ▨, PBTM using r_θ^i; 🟥, BTM.

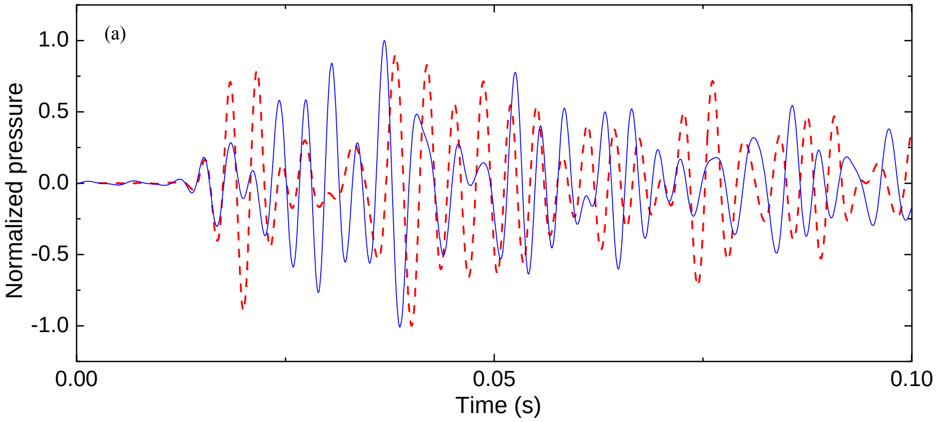

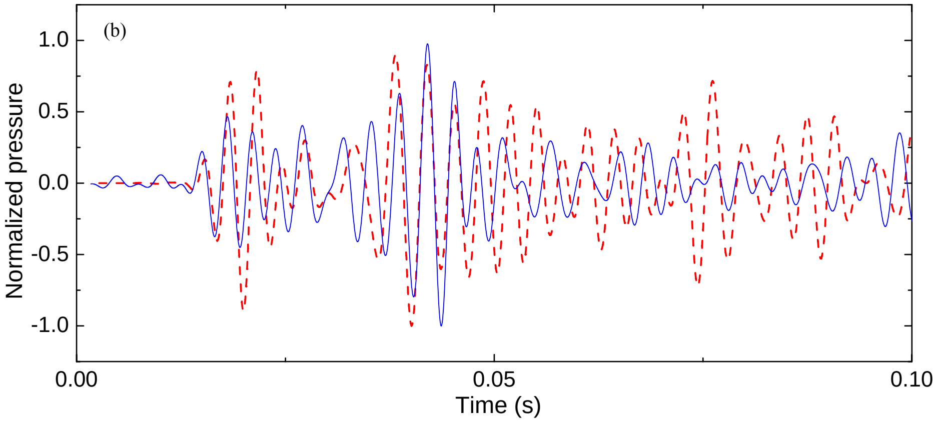

(Fig. 3.15 continued)

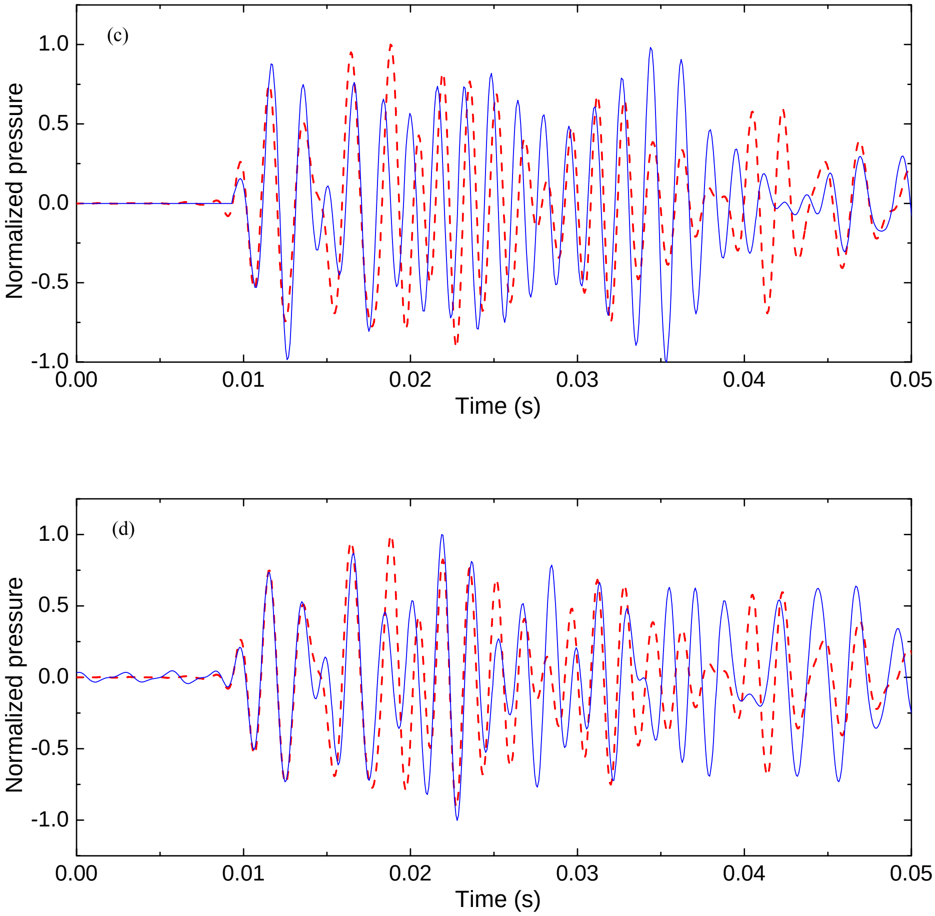

Fig. 3.15. A comparison of measured and calculated pressure impulse responses (R3 position): – – –, measured; ——, calculated by PBTM. (a), (b) 250 Hz; (c), (d) 500 Hz. (a), (c) Use of angle-independent reflection coefficient r_θ^i; (b), (d) use of angle-dependent reflection coefficient r_θ^d.

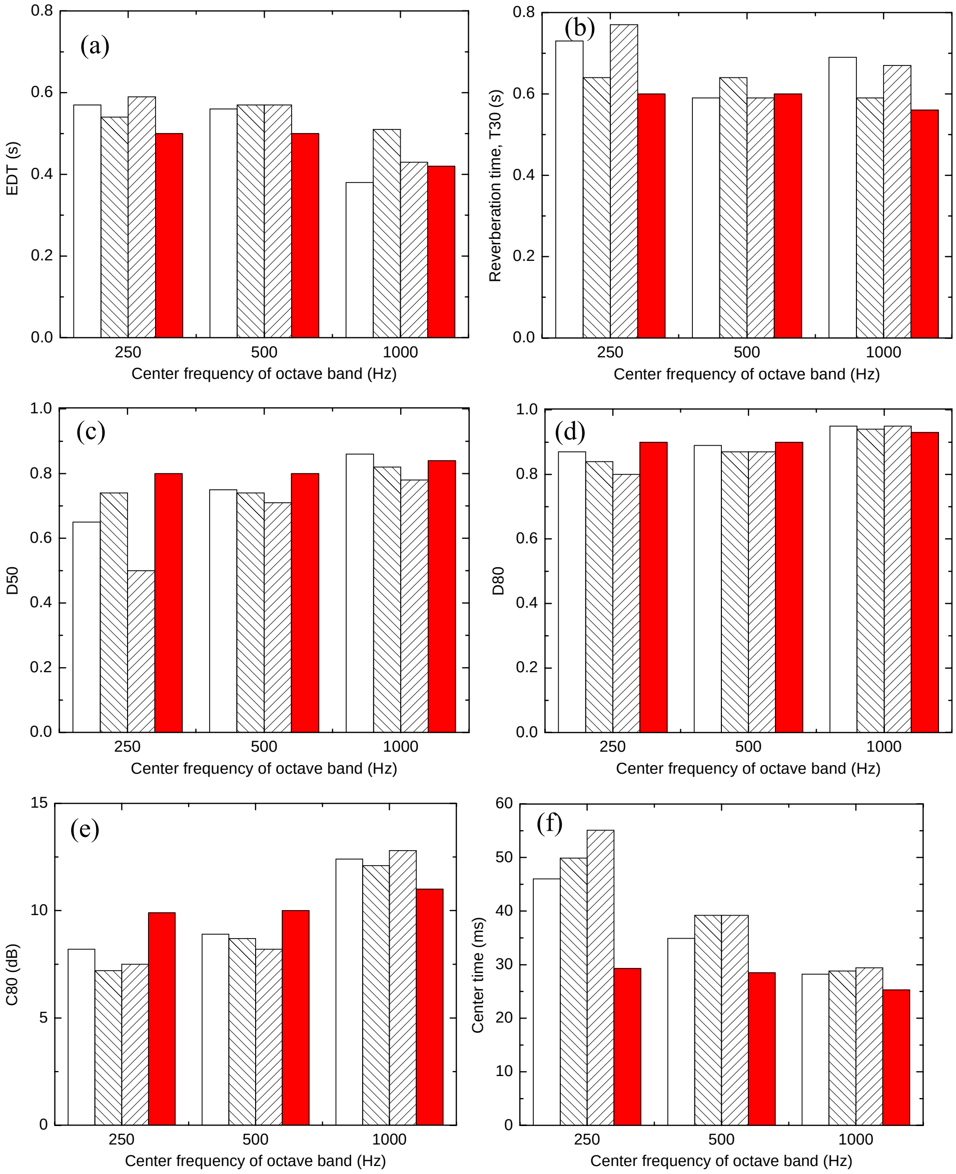

Fig. 3.16. A comparison of measured and calculated room acoustic measures (R3). (a) Early decay time (EDT), (b) Reverberation time (T30), (c) Definition (D50), (d) Definition (D80), (e) Clarity (C80), (f) center time (Ts). ☐, Measurement; ▧, PBTM using r_θ^d; ▨, PBTM using r_θ^i; 🟥, BTM.

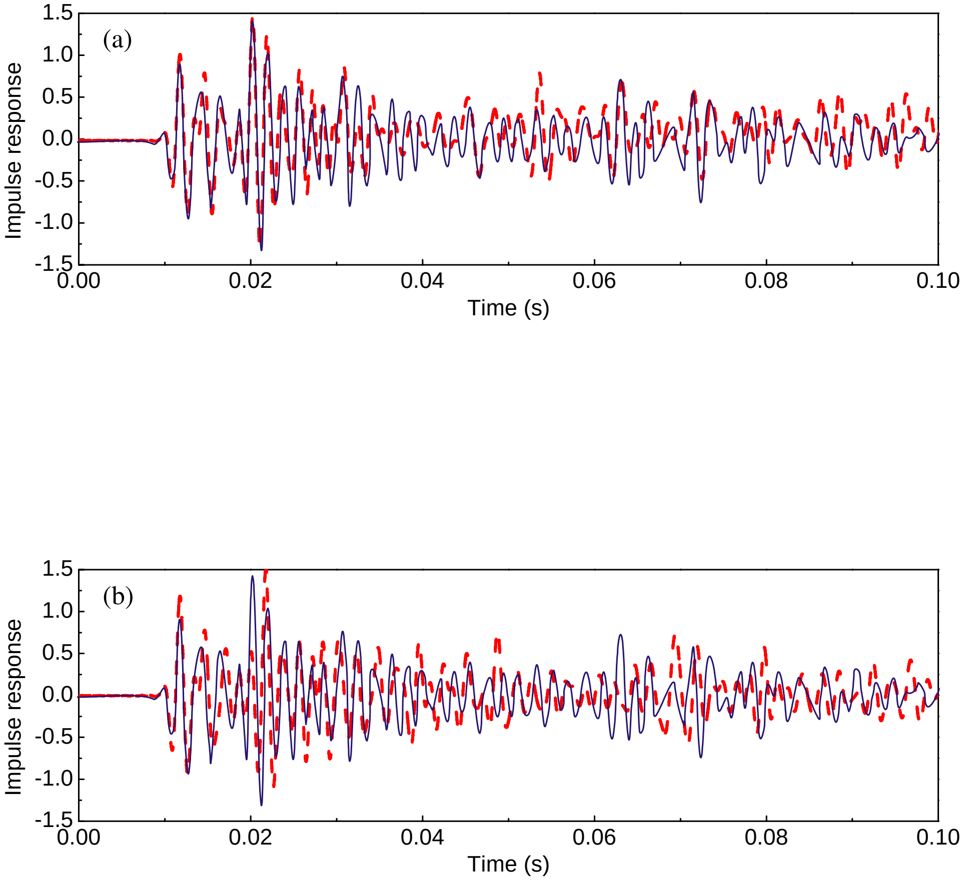

Fig. 3.17. A comparison of IR between the phased geometrical method and measurement. – – –, The phased geometrical method; ——, measurement [25]. (a) PBTM with 2000 beams, (b) PRTM with 2000 rays and the spherical receiver of which the radius of 1 m.

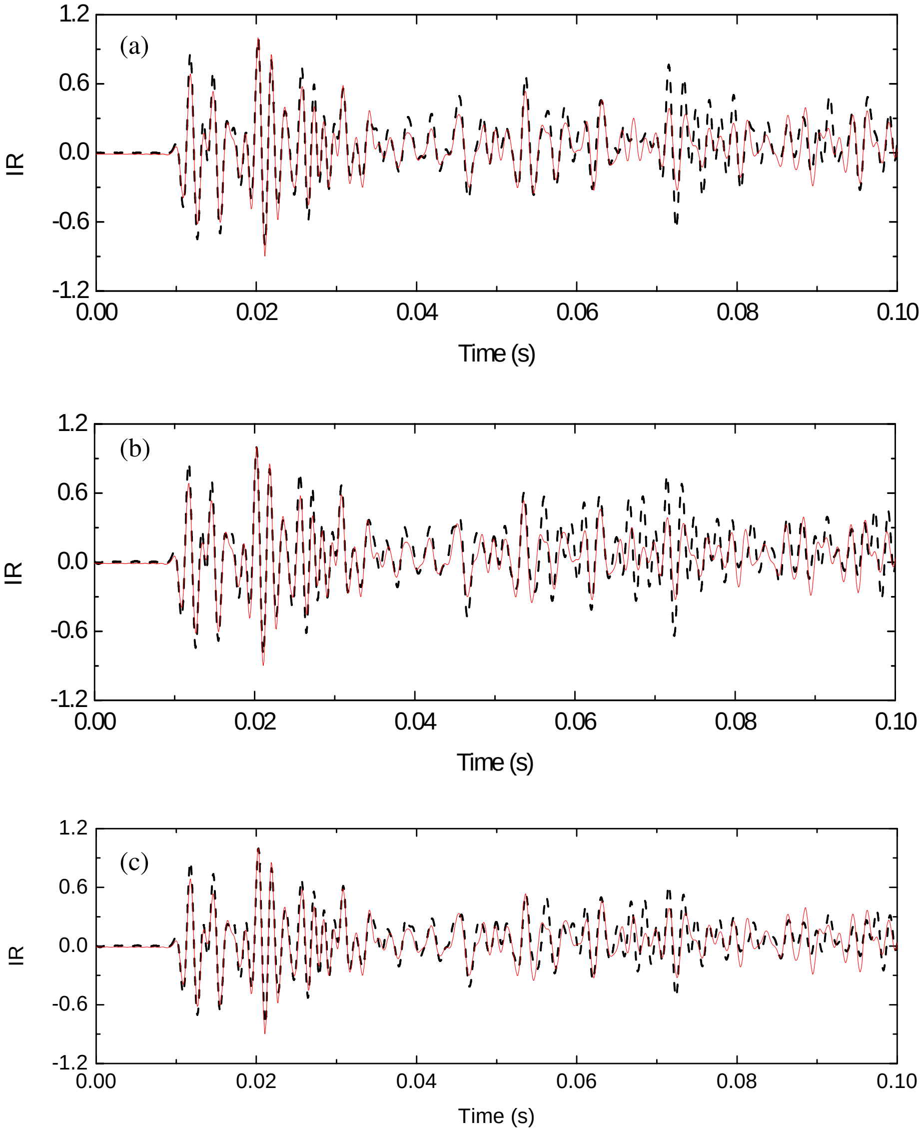

Fig. 3.18. A comparison of normalized impulse response., ——, Use of complex reflection coefficient; – – –, use of approximate real reflection coefficient. (a) r_{θ}^{d}, (b) r_{θ}^{i}, (c) attenuated r_{θ}^{d} by a factor of 0.8. The RTs are 0.50 s, 0.46 s, 0.51 s. The RT from complex reflection coefficient of 0.49 s.

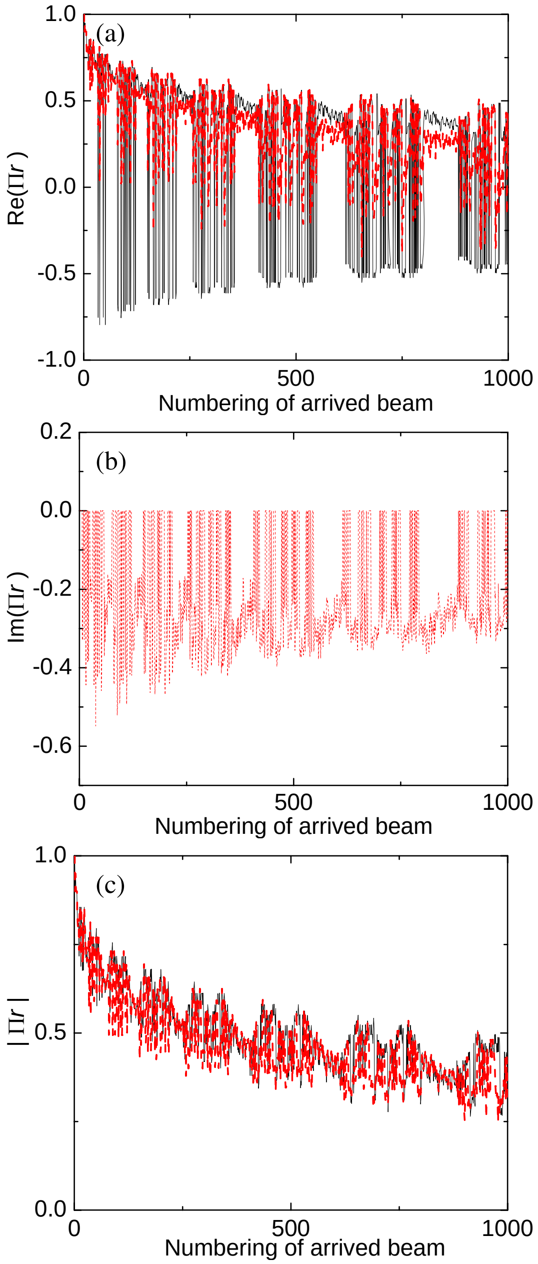

Fig. 3.19. A comparison of reflection coefficient. (a) Real part of reflection coefficient, (b) imaginary part of reflection coefficient, (c) magnitude of reflection coefficient. - - - - - -, Use of complex reflection coefficient; ——, use of angle-dependent reflection coefficient.

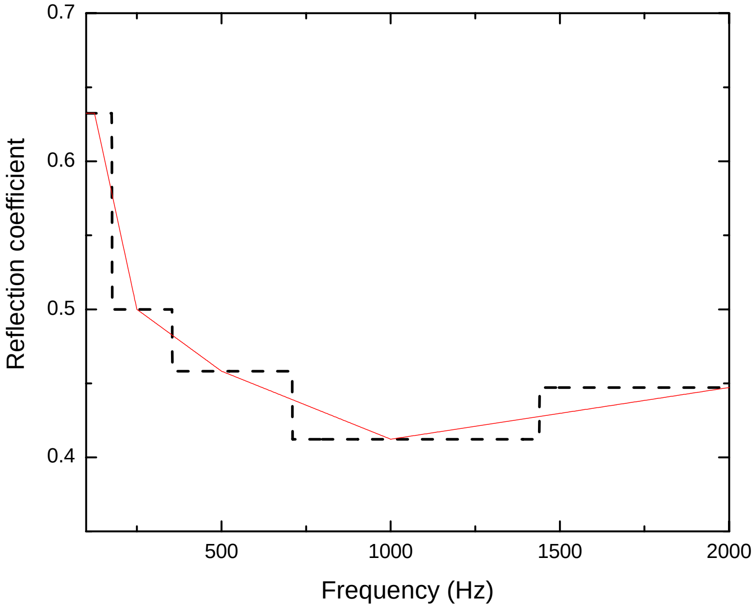

Fig. 3.20. Example of continuous and stepwise reflection coefficient for the ceiling. ———, Continuous reflection coefficients; — — —, Stepwise reflection coefficient.

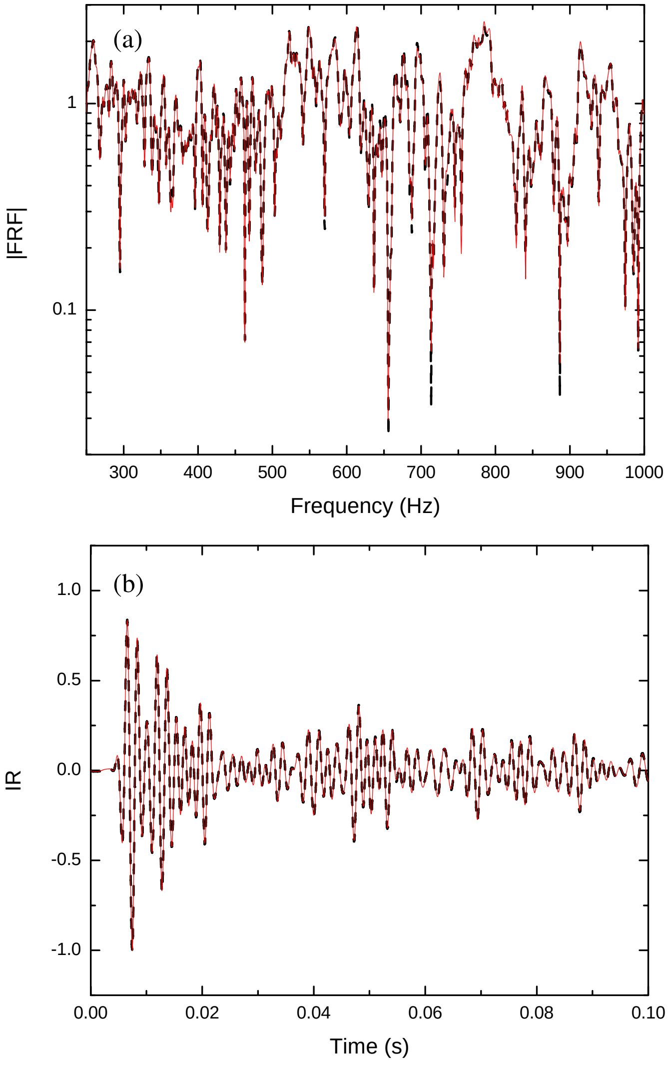

Fig. 3.21. Comparisons of FRF and IR. (a) FRF, (b) IR. ———, Continuous reflection coefficient; — — —, stepwise reflection coefficient. RT from stepwise and continuous reflection coefficient are 0.64 s and 0.63 s, respectively.

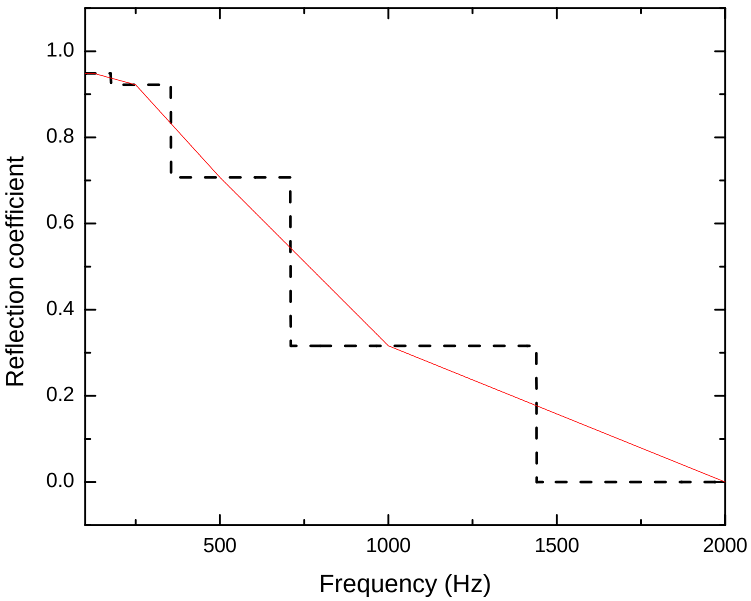

Fig. 3.22. Example of continuous and stepwise reflection coefficient for the ceiling. ——, Continuous reflection coefficient; – – –, stepwise reflection coefficient.

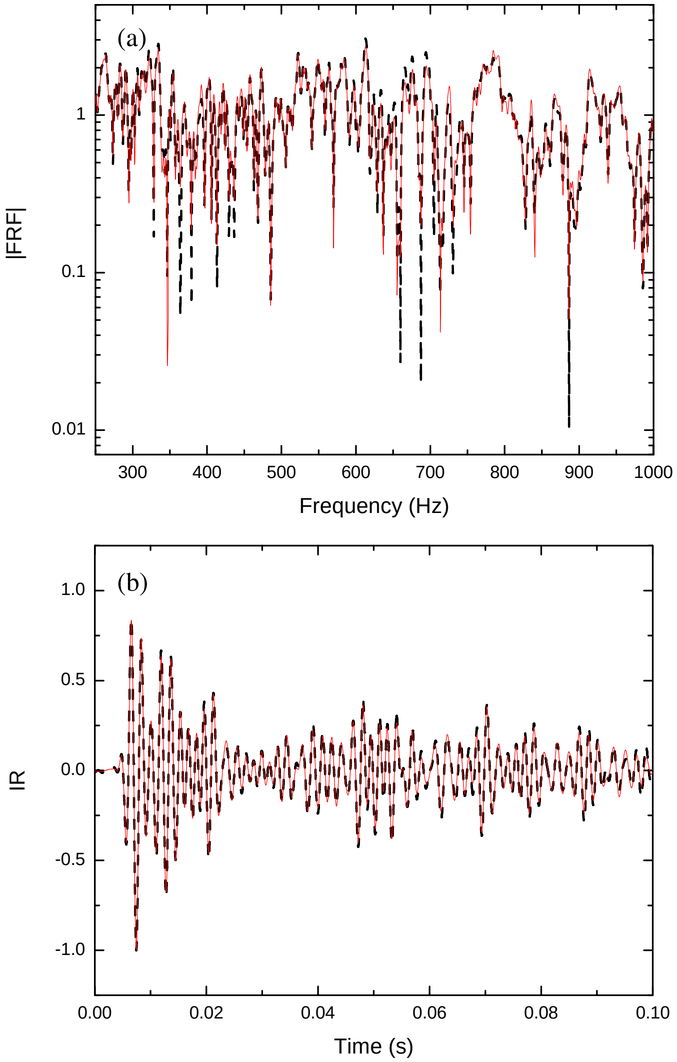

Fig. 3.23. Comparisons of FRF and IR. (a) FRF, (b) IR. ———, Continuous reflection coefficients; — — —, Stepwise reflection coefficient. RT employing stepwise reflection was 0.65 s and RT employing continuous reflection coefficient was 0.64 s.

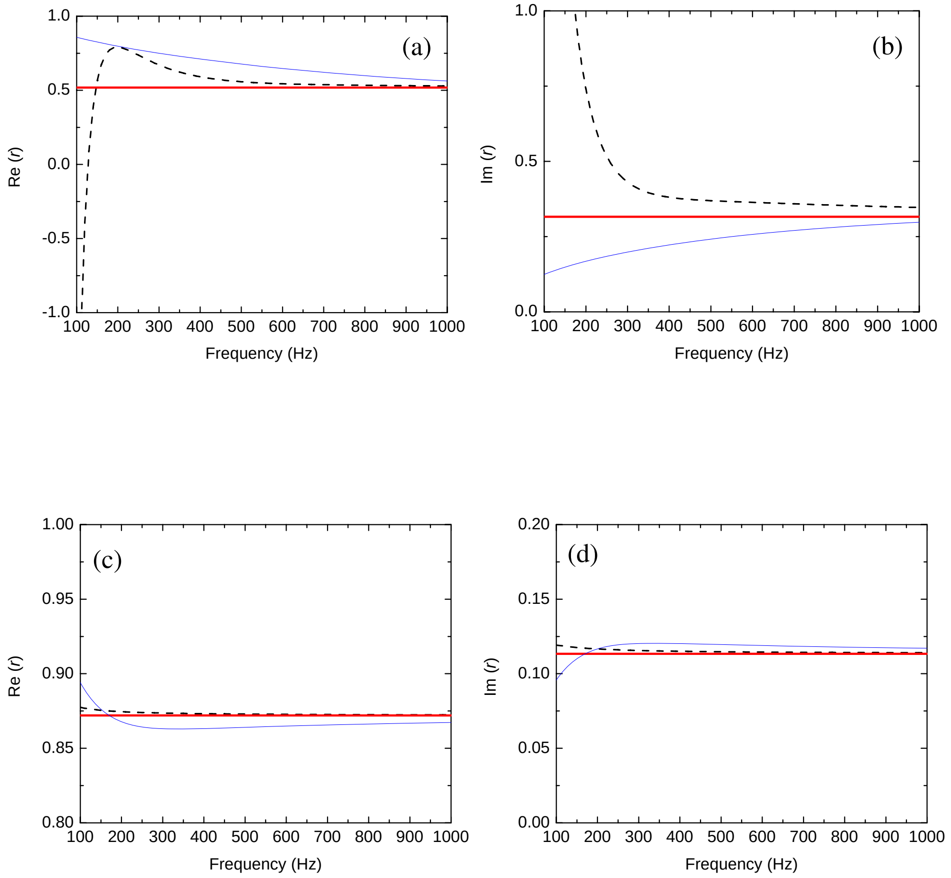

Fig. 3.24. A comparison of reflection coefficient as a function of frequency when Z_w=4150+4150*j*. (a),(c) Real part of reflection coefficient, (b),(d) imaginary part of reflection coefficient. (a),(b) θ=80°, (c),(d) θ=45°. ▬, plane wave *r*, – – – –, spherical wave *r*; ——, size compensated *r*.

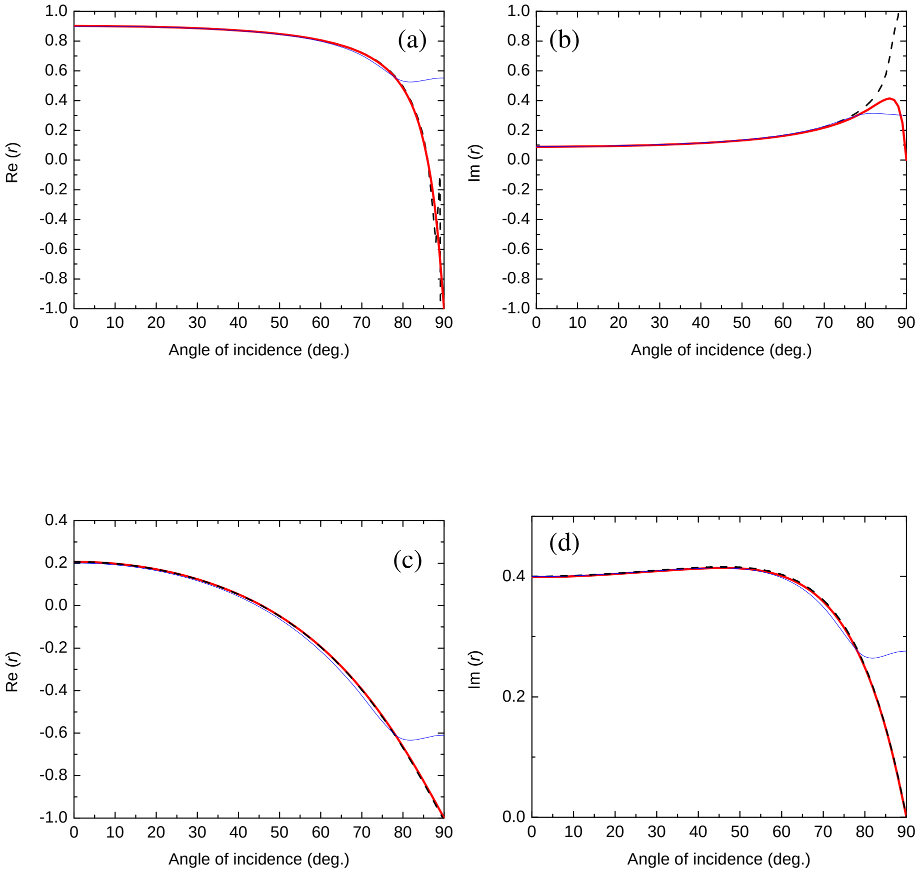

Fig. 3.25. A comparison of reflection coefficient as a function of angle of incidence at 1 kHz. (a),(c) Real part of reflection coefficient, (b),(d) imaginary part of reflection coefficient. (a),(b) Hard surface (Z_w=4150+4150j), (c),(d) soft surface (Z_w=415+415j). ▬, plane wave r, – – – –, spherical wave r; ——, size compensated r.

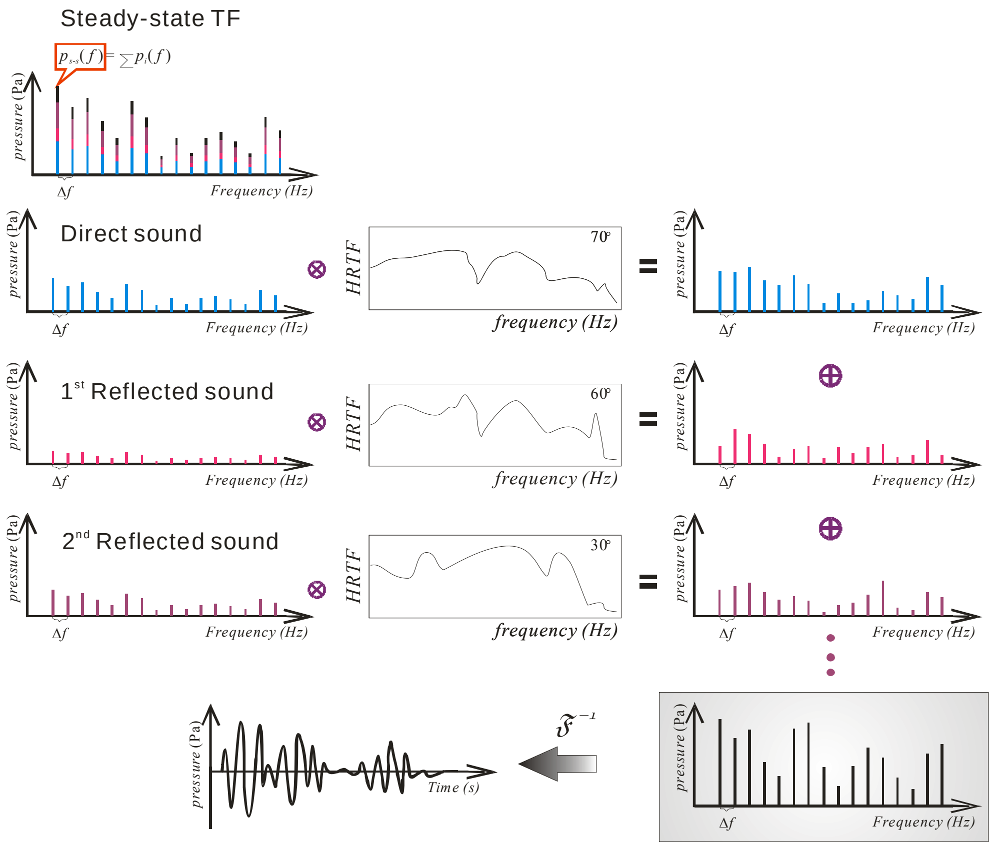

Fig. 3.26. Binaural processing. Transfer function for each reflection is decomposed and convolved with the measured HRTF. The convolved signals are summed into a total transfer function and inverse Fourier transformed into a time domain response.

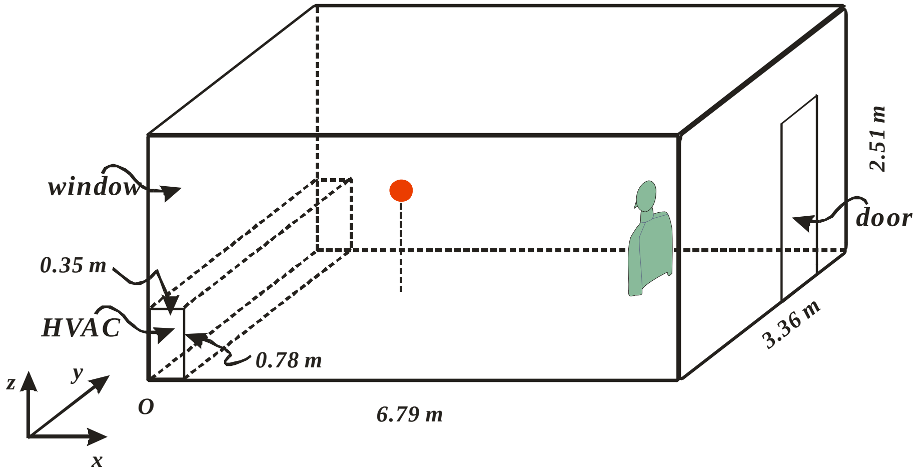

Fig. 3.27. Test room model. ● denotes the source and 👤 the dummy head. Acoustic properties of surfaces are specified in Table 3.3.

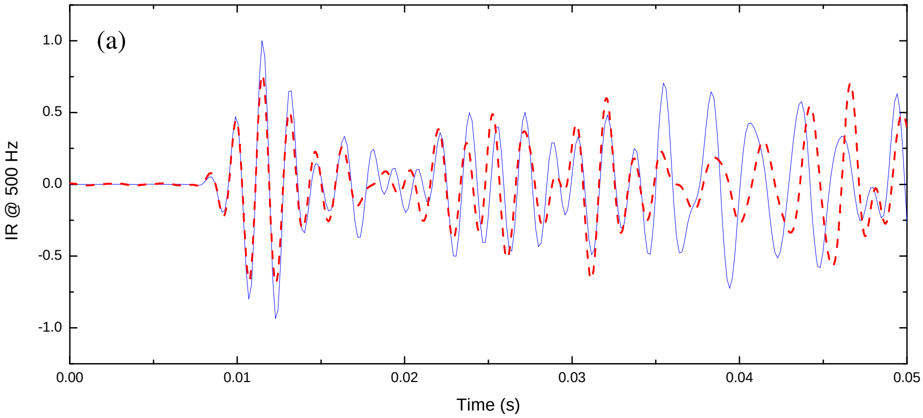

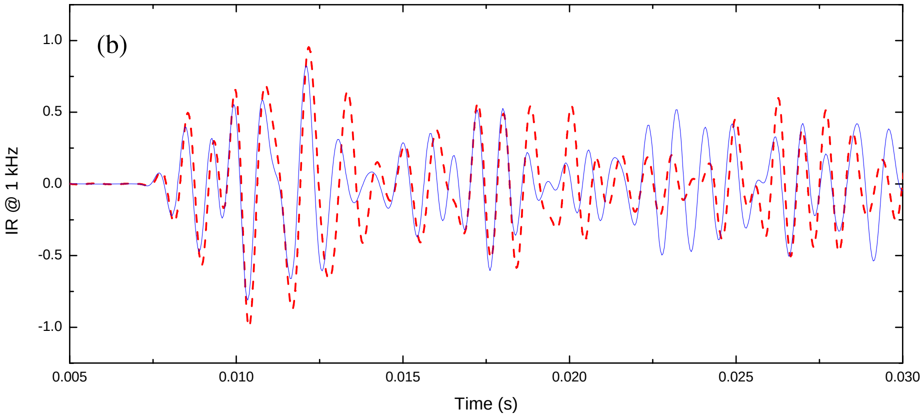

(Fig. 3.28 continued)

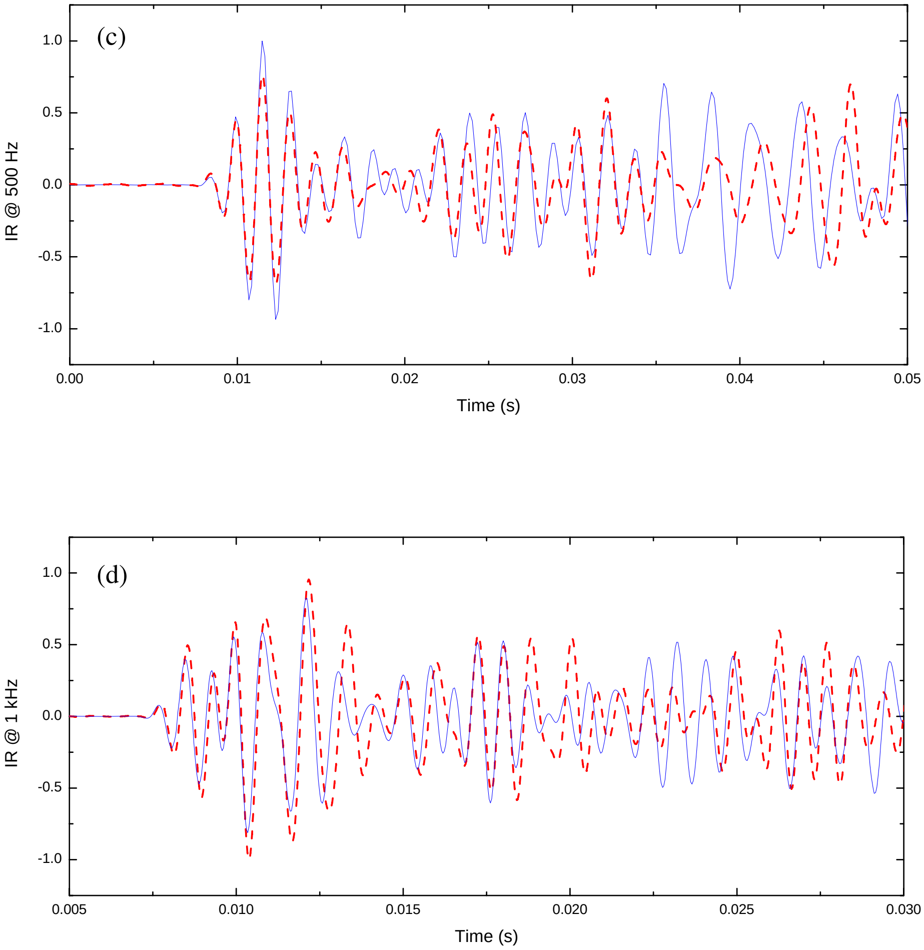

Fig. 3.28. Comparisons of IR for octave band. ——, PBTM; – – –, measurement. (a) 125 Hz, (b) 250 Hz, (c) 500 Hz, (d) 1 kHz.

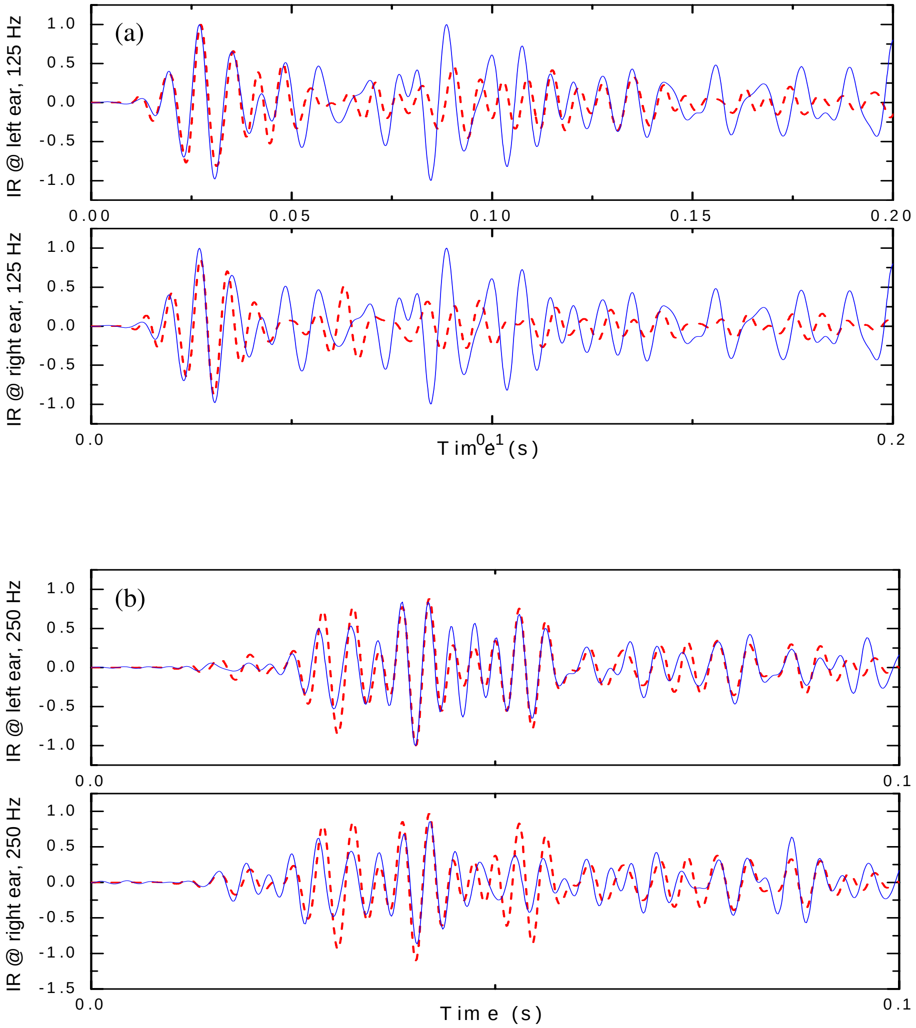

(Fig. 3.29 continued)

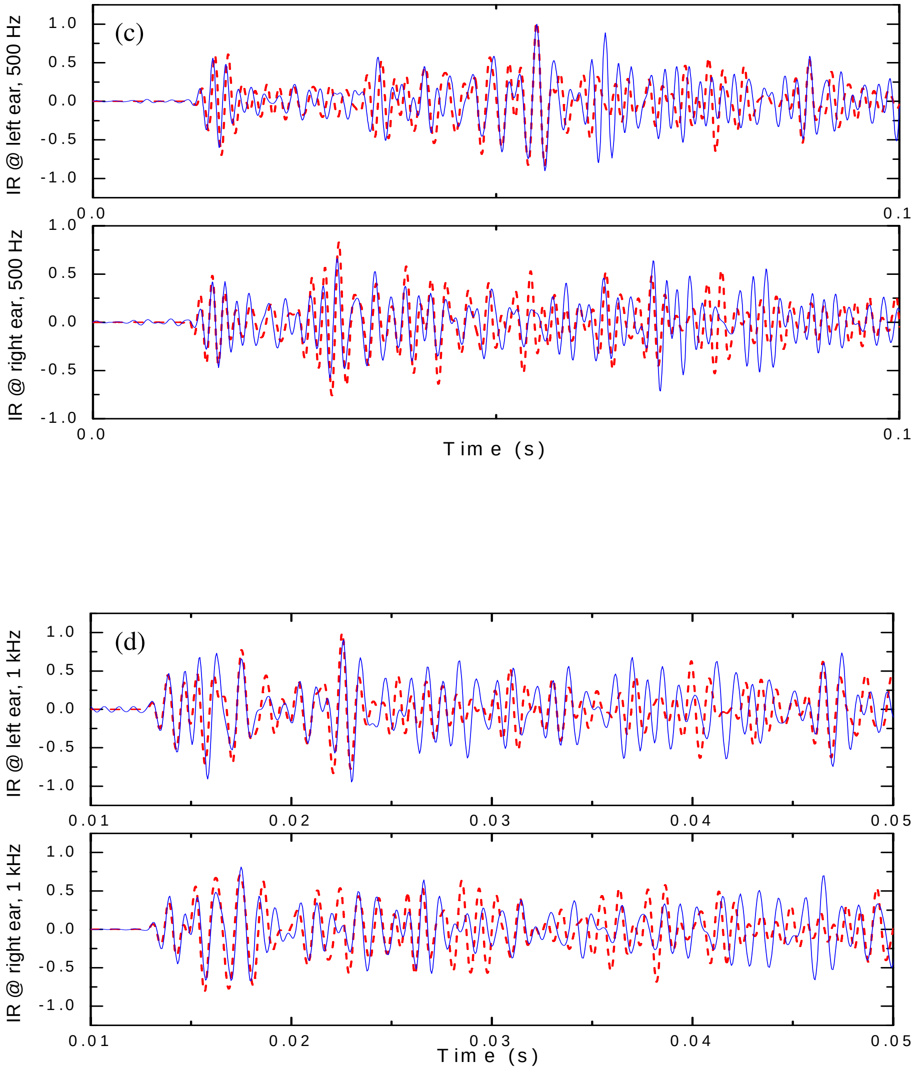

Fig. 3.29. Comparisons of binaural signals for octave band. ———, PBTM; – – –, measurement. (a) 125 Hz, (b) 250 Hz, (c) 500 Hz, (d) 1 kHz.

4. CONSIDERATION OF DIFFRACTION

Diffraction is defined as the bending of waves around small obstacles and spreading out of waves beyond small opening. It means the distortion of wave fronts due usually to the presence in a medium of bodies or obstacles of a highly disparate medium [18]. Diffraction is the major concern at low frequency because the acoustic diffraction occurs when the wavelength of the sound is comparable or larger than the dimension of an obstacles or aperture. Conventional geometrical acoustics fails to account for the phenomenon of diffraction because the rays or ray tubes (generally called beams) should spread straightly, not bend over any obstacles or aperture. That feature results in the existence of zero pressure field in the shadow zone, which consequently yields the discontinuity near the shadow boundary and reflection boundary. The diffraction considerably affects the pressure field near the corner, edges, aperture in the screen. Also, grazing incidence on the edge is the typical example of diffraction effect.

The diffraction problem of an infinite wedge irradiated by a point source was studied by Biot and Tolstoy [36] by using normal modes as generalized coordinates in Hilbert space. It was extended by Medwin to apply the Biot-Tolstoy solution to underwater problem and noise barrier [37] by the concept of secondary edge source. The key is the analytical directivity functions for the edge sources and the contributions of first order diffraction to impulse response from the two sides around the apex point are exactly identical. The Biot-Tolstoy model has been also extended by the Göteberg group to improve the accuracy of the early part of room impulse response [40,79,97-100]. They chose the time domain model by virtue of time domain representation for room acoustics analysis and auralization.

The Kirchhoff diffraction approximation based on Huygen's principle has been introduced to represent the field diffracted through an aperture as an integral over the aperture [38,101-104]. It can be used for both frequency and time domain, but generally employed in the time domain for edge diffraction. However it has been reported by several researchers that it is compute intensive [39] and leads to large errors even at high frequencies[40-42]. The boundary conditions in the aperture plane are not reproduced and aperture edge interaction is not accounted for. For the object or surface that has sharp edges the Kirchhoff approximation does not yield correct diffraction behavior.

The geometrical theory of diffraction (GTD) was initially suggested by Keller [43] to account for the diffraction using in the geometrical optics field. His main idea was to introduce new diffracted ray at the corners, edges, and vertices of surfaces with an appropriate diffraction coefficient. Then the diffracted field is added to the geometrically calculated field. This was successfully adopted for optics and electro-magnetics as well as acoustics. It has been known that the GTD is generally superior to Kirchhoff diffraction theory in both accuracy [45-47] and efficiency at high frequencies [41,43]. The shortcoming of above mentioned sharp edge problem was corrected by the GTD. Keller's geometrical theory of diffraction provides a systematic means for computing diffraction coefficient. The diffraction coefficient is obtained from a special canonical problem, the problem of diffraction of a plane wave by a half plane [43,48]. The GTD is well formulated in the acoustics field by Le Bot [105,106].

However, it fails at near shadow and reflection boundaries due to singularity in the diffraction coefficient. Therefore the uniform theory of diffraction (UTD) was suggested by Kouyoumjian and Pathak [48] to remove the singularity. This theory shows considerable improvement over the earlier methods in accurately and efficiently accounting for observations. Most of the research have been focused on the perfectly conducting surface condition [41,43,48], not the realistic impedance boundary condition.

Geometrical theory of diffraction started from the hypothesis that the geometrical optics field corresponds to the leading term of Luneberg-Kline series for the reduced wave equation or Maxwell's equation. The higher order terms account for diffraction and other wave phenomena. This concept can be also adopted in the acoustics. The geometrical acoustics can predict quite accurately when the leading term of a boundary value problem is dominant compared to other higher order terms, i.e, at high frequency response and weakly reverberant field. Otherwise, the diffraction effect should be taken into account to improve the precision of the simulations.

The most common diffraction problem is the diffraction of half plane, wedge, and aperture. Among them, while the diffraction of half plane such as barrier or screens is the remarkable problem in the outdoor propagation, the diffraction of wedge is the most important issue in an enclosed room. One example of wedge diffraction is a step discontinuity, because there are many structures having right-angle edges such as HVAC (heating, ventilating and air conditioning) system and furniture in a room.

4.1. Uniform Theory of Diffraction

Diffraction is absolutely the topmost phenomenon at low to mid frequency. So far in the PBTM, the straightly propagating beams can not detect the receiver position in the shadow region outside the reflection boundary where the diffraction phenomenon becomes predominant. The aim of this chapter is to integrate the UTD into the PBTM to account for the diffraction near the reflection and shadow regions to remove the discontinuities. Also, the applicability of the PBTM can be extended to low frequency range by considering the diffraction. The PBTM allows both frequency and time domain calculation. Generally, after a frequency domain response between the source and receiver is obtained, an impulse response can be calculated by the inverse Fourier transform. Hence the frequency domain solution for diffraction problem is more appropriate in this case.

According to the previous researches, the general expression of the diffracted pressure for spherical wave is as follows:

$$p^d(\rho,\phi;\rho',\phi') = \frac{e^{-jk(\rho+\rho')}}{\rho'} D\left(\frac{\rho\rho'}{(\rho+\rho')},\phi,\phi'\right)\sqrt{\frac{\rho'}{\rho(\rho+\rho')}} \,. \tag{4.1.1}$$

Here, ρ and ρ' are the distances from the diffracted spot to receiver and source, respectively. ϕ and ϕ' are the angles from the surface to the source and receiver, respectively. Last term means a divergence factor which is the function of both ρ and ρ'.

The diffraction coefficient is the function of both distance and angles which originated from Fresnel integration. According to the GTD by Keller [43], The diffraction coefficient for the wedge of angle $(2\text{-}n)\pi$, which was deduced by comparing the asymptotically expanded Sommerfeld's exact solution for large values of kr is expressed as (if the field point is not close to a shadow or reflection boundary)

$$D_{s,h}\left(\phi,\phi';\beta_o\right)=-\frac{e^{-j\pi/4}\sin\frac{\pi}{n}}{n\sqrt{2\pi k}\,\sin\beta_o}\left[\left(\cos\left(\frac{\pi}{n}\right)-\cos\left(\frac{\phi-\phi'}{n}\right)\right)^{-1}\mp\left(\cos\left(\frac{\pi}{n}\right)-\cos\left(\frac{\phi+\phi'}{n}\right)\right)^{-1}\right], \quad (4.1.2)$$

where β_o is the angle between the incident ray and the tangent to the edge. In the equation, the upper sign applies to D_s, the scalar diffraction coefficient for soft boundary and the lower to D_h standing for hard boundary. This expression becomes singular as shadow or reflection boundaries are approached. The diffraction coefficient vanishes when sin $\pi/n=0$; hence for $n=1$, entire plane, $n=1/2$, the interior right angle, $n=1/M$, $M=3,4,5,\ldots$, interior acute angles. The boundary value problem can be solved exactly in terms of the incident field and finite number of reflected fields, which may be determined from image theory. Moreover as $n\rightarrow 0$, even with the non-vanishing diffracted field, the phenomenon is increasingly dominated by the incident and reflected field.

The regions of rapid field change adjacent to the shadow and reflection boundaries are referred to as transition regions. In the transition regions, the magnitude of the diffracted field is comparable with the incident or reflected field, and since these field are discontinuous at shadow and reflection boundaries for the total field to be continuous there.

The uniform version of GTD, suggested that the diffraction coefficient for the wedge of angle $(2-n)\pi$ is expressed as follows: [39,41,48]

$$D\left(L,\phi,\phi'\right)=-\frac{e^{-j\pi/4}}{2n\sqrt{2\pi k}}\sum_{i=1}^{4}\cot\left(T_i\right)F\left(x_i\right), \quad (4.1.3)$$

where

$$T_{1,2}=\frac{\pi-\left(\phi\mp\phi'\right)}{2n},\ T_{3,4}=\frac{\pi+\left(\phi\mp\phi'\right)}{2n}\ \text{ and }\ F\left(x\right)=2jwe^{jx^2}\int_x^{\infty}e^{-j\tau^2}d\tau. \quad (4.1.4)$$

Arguments of the Eq. (4.1.3) are given by

$$x_{1,2}=\sqrt{\frac{2k\rho\rho'}{\left(\rho+\rho'\right)}}\cos\left[\frac{2\pi nN^{\pm}-\left(\phi\mp\phi'\right)}{2}\right]\ \text{ and }\ x_{3,4}=\sqrt{\frac{2k\rho\rho'}{\left(\rho+\rho'\right)}}\cos\left[\frac{2\pi nN^{\mp}-\left(\phi\mp\phi'\right)}{2}\right]. \quad (4.1.5)$$

Here, N^+ and N^- are integers which most nearly satisfy the following equation:

$$2\pi nN^{+}-\left[\phi\mp\phi'\right]=-\pi,\ 2\pi nN^{-}-\left[\phi\mp\phi'\right]=-\pi. \quad (4.1.6)$$

In the UTD to resolve the singularity at the reflection/shadow boundary, Fresnel integration, $F(x_i)$, was introduced. The nominator makes the diffraction coefficient complex-value, and there is a summation of four terms which consist of Fresnel integral and corresponding cotangent function. Diffraction coefficient is inversely proportional to the square root of wavenumber. Therefore the diffraction effect is diminishing as the frequency goes higher. The integers $N^{\pm}$ are particularly important near the shadow and reflection boundaries. It can be found that $N^{\pm}$ do not change abruptly near these boundaries, which is a desirable property [48]. The complex Fresnel integral is expressed in terms of the complementary error function with complex arguments as follows: [107]

$$F_1(x) = \int_x^{\infty} e^{-j\tau^2} d\tau = e^{-j\pi/4} \int_{xj\pi/4}^{\infty} e^{-u^2} du = \frac{\sqrt{\pi}}{2} e^{-j\pi/4} erfc\left(x e^{j\pi/4}\right). \tag{4.1.7}$$

The asymptotic solution of the Fresnel integral can also be used in calculating diffraction coefficient. Two asymptotic solutions depending on the low and high values ware suggested and the valid range was investigated [48]. x should be less than 0.3 for Eq. (4.1.8a) and x should be sufficiently larger than 4 for Eq. (4.1.8b). In the intermediate range, the spline interpolation using four points was used.

$$F(x) \approx \left[\sqrt{\pi x} - 2x \exp\left(j\frac{\pi}{4}\right) - \frac{2}{3}x^2 \exp\left(-j\frac{\pi}{4}\right)\right] \cdot \exp\left[j\left(\frac{\pi}{4} + x\right)\right], \ for \ x < 0.3, \tag{4.1.8a}$$

$$F(x) \approx \left(1 + j\frac{1}{2x} - \frac{3}{4}\frac{1}{x^2} - j\frac{15}{8}\frac{1}{x^3} + \frac{75}{16}\frac{1}{x^4}\right), \ for \ x > 4. \tag{4.1.8b}$$

4.2. Characteristics of Diffraction Coefficient

Figure 4.1 shows the diffraction coefficient according to Eq. (4.1.3). Fig. 4.1(a) shows the perfectly conducting step in a free field. Source is located at 45° and receiver points are varied from 0° to 270°. Figs. 4.1(b) and 4.1(c) show the diffraction coefficient of the singly diffracted and doubly diffracted wave, respectively. In both figures, as the frequency gets higher, the diffraction coefficient is decreasing. It is noted that discontinuities in the diffraction coefficient are essential for the total field to be continuous.

For single diffraction, two discontinuities are found at 135° and 225°, which are reflection boundary (RB) and shadow boundary (SB) , respectively in Fig. 4.2. Because there is an abrupt change happening in the geometrical acoustics field at the RB (135° in this case), the diffracted sound field should have the discontinuity. From 0° to RB, diffracted sound contributes in a destructive manner by adopting negative real part of diffraction coefficient, whereas it adds to the geometrical acoustics field in a constructive manner beyond the RB. Then the discontinuity at the RB is alleviated. The same thing happens near the SB. By approaching the SB, the diffraction coefficient gets smaller to alleviate the discontinuity, however the diffraction coefficient suddenly becomes large at the SB. It is noted that the imaginary part of single diffraction smoothly decreases.

For double diffraction, there are discontinuities at 90° in both real and imaginary part in Fig. 4.3 to mitigate the discontinuity at 90° owing to the single diffraction. When the diffraction coefficient has negative real part, then the waveform in time is inverted. Then, discontinuities at RB and SB are corrected by introducing a proper diffraction coefficient.

Zhang et al. [41] have studied on the acoustic pulse diffraction by 90° step in Fig. 4.4(a) and their result showed a good agreement with the previous research for the same problem [108]. Diffraction pattern was investigated, which is $\rho=3\lambda$ apart from the edge of a 90° step of height $h=\lambda$ in a hard plane for essentially plane wave incidence ($\rho'=1000\lambda$, $\phi'=45°$). Figure 4.5 shows the decomposition of sound field into two fields. The geometrical acoustics field is composed of the direct and specularly reflected sound field, which is equivalent to the pressure field by the conventional PBTM. The other one is the diffracted field by the uniform version of GTD. It is noted that incident wave always exist (there is no SB), but reflected sound can not reach the observation points in the angular range from 135° to 163.1° in Fig. 4.4(b). The UTD implemented in the PBTM was compared with their result in Fig. 4.6 Total pressure distribution in Fig. 4.6(a) agrees well with previous result. Pressure field by the direct and reflected field and diffracted portion are shown in Fig. 4.6(b) and Fig. 4.6(c), respectively. The discrepancy between the geometrical acoustics field by the PBTM and the total pressure field can be seen clearly and it can be compensated by the UTD. The diffracted pressure has a maximum value of 30% at 135° and 161°. From 0 to 90°, there are two diffracted sound paths, single and double diffraction in Fig 4.7(a). However, above 90°, the reflection of singly diffracted sound from the lower floor should be added as shown in Fig. 4.7(b).

Figure 4.8 shows the single diffracted sound field which dominates the diffraction effect. Fig. 4.8(a) shows the single diffraction from the corner of upper surface and Fig. 4.8(b) shows the reflection after the edge diffraction. In Fig. 4.8(a), the contribution of edge diffraction is constant of 5% until 90°. At the discontinuity of 135°, it has the maximum value of 23% and gradually decreases. The reflection after single diffraction in Fig. 4.8(b) is discontinuous at 90° and gradually increases. The peak appears at 163.1° and sudden decrease was found due to the reflection from lower plate. After 163.1°, because the geometrical field is predominant, the diffraction effect becomes insignificant.

The double diffraction is quite smaller than single diffraction in Fig. 4.9. The average contribution of double diffraction is negligible about 2%. The maximum contribution appears at 90°. The important role of double diffraction is to compensate the discontinuity at 90° due to the reflection of the diffracted sound. Figure 4.10 shows the diffracted pressure for the single diffraction and both single and double diffraction, respectively. Figure 4.10(a) shows the sum of singly diffracted pressure shown in Fig. 4.9. There is a clear discontinuity at 90°, but it can be corrected by the double diffraction shown in Fig. 4.9. Except for the angular section around 90°, two graphs show a good agreement. The main role of double diffraction is highlighted at the discontinuity at 90°, to mitigate the discontinuity due to the single diffraction.

The second example was chosen as to investigate the diffraction near the shadow boundary. The source was located at the same point as the first example, but the radius of receiver distribution was reduced to the wavelength in Fig. 4.11. Figure 4.12 shows the calculated pressure field by the conventional PBTM and PBTM combined with UTD. Two discontinuities are clearly seen at 135° and 225°. After the RB and SB, the geometrical acoustics field becomes discontinuous by the conventional PBTM, but it can be corrected with the aid of UTD. Diffracted pressure distribution is plotted in Fig. 4.13. The maximum diffracted portion of sound is about 45% after 225°, which can not be neglected in the prediction of pressure near a step. For the spherical wave condition, in which the sound source is 2λ apart from the corner, the diffraction effect gets less significant compared to the plane wave condition, as shown in Fig. 4.14.

The time domain response was investigated for the diffraction model in Fig. 4.11. The receivers were distributed from 0° to 270° with a step of 5°. By the

PBTM with UTD, the transfer function between the source and receiver is calculated in the frequency domain and it is convolved with a Gabor pulse, expressed in Eq (4.2.1).

$$g(t) = e^{-\alpha^2 t^2} \cos(\omega_o t) \tag{4.2.1}$$

Here, the parameters α and, f_0 are set to 1250 and 30 Hz, respectively. The time and frequency domain representation were displayed in Fig. 4.15. Gabor pulse responses including diffraction were shown in Fig. 4.16. The beauty of these plots is that one can see the continuous pulse train clearly for direct sound and reflected sound, and so on. At $\phi = 0°$, the incident and reflected sound are merged at the same time of arrival (0.02 s), but they gradually separate into two branches. After the reflection, the diffracted sounds were followed. By comparing with the geometrical acoustics field shown in Fig. 4.16(b), Fig. 4.16(a) displays small wavelets representing the diffraction effect. Reflected pulses from the surface disappear after RB of ϕ=135° in Fig. 4.16(b). In Fig 4.16(c), the family of single diffraction was displayed and followed by the reflected pulse of single diffraction; pulses around 0.04 s indicate the single diffraction from the upper corner and the positive pulses after the single diffracted pulse are the reflection after the edge diffraction. Figure 4.16(d) displays the doubly diffracted pulses. They are quite small compared to other components. The waveform becomes inverted at ϕ=90°. Figures 4.16(e) and 4.16(f) illustrate the family of single diffraction; diffraction from the upper corner and reflection after the diffraction, respectively. Interestingly, the double diffraction and reflection after edge diffraction appear simultaneously, around 0.06 s. They are all discontinuous at ϕ=90°, but consequently the overall response becomes smooth as shown in Fig. 4.16(a). In the time domain response, positive pulse means the positive real part of diffraction coefficient. When the real part of diffraction coefficient becomes negative, e.g. the single diffraction from 0° to 135° and double diffraction beyond 90°, the negative pulses are found.

4.3. Comparison with Measurement and BEM

Measurement was conducted in an anechoic chamber using MLS signal. B&K dodecahedron sound source (type 4296) and 1/2'' microphone (type 4130) with diffuse field corrector were used. The height of the step, *h*, is 0.68 m, which corresponds to 500 Hz. In the first example in Fig. 4.17, single diffraction path length is shorter than the reflected path length. The locations of source and receiver were set to maximize the diffraction effect where $\phi+\phi' \approx \pi$.

Impulse response in 125 Hz octave band in Fig. 4.18(a) agrees better with measured data than that in Fig. 4.18(b). The reflected pulse at 0.025 s in Fig. 4.18(b) disappears when the diffracted waves are added. Furthermore, the magnitude of the peaks shows a better correspondence than the conventional PBTM. The difference between the measurement and simulation arises owing to finite size of a step and measurement error.

The room with a diffracting edge in Fig. 4.21 was dealt with by adopting the PBTM with UTD. This geometry is the typical example of diffracting object in an enclosure. Source and receiver were located at (0.3, 0.3, 0.3) and (0.5, 0.7 0.3), respectively. The room is quite small with the volume of 3 m^3 and the Schroeder cutoff frequency is quite high as 387 Hz. The order of diffraction in an actual enclosed space should be determined. As well as the diffraction of the actual sound source, the diffraction of reflected sounds should be included. By virtue of the image source concept, the diffraction of reflected sound can be implemented. It should be mentioned that the image sources lower then the step should be neglected. For the diffraction of the reflected sound, corresponding reflection coefficient of the wall was multiplied to the calculated pressure. Figure 4.20 shows the comparison of transfer functions in terms of order of diffraction. The simulation results converge when the diffraction order is 6. A comparison between PBTM result and BEM result is shown in Fig. 4.21. Precision of the simulation is improved by considering the diffraction effect. Usually the zeros are mostly influences, because diffracted pressure is comparable to the pressure by the geometrical acoustics near zeros. The convergence of diffracted pressure as a function of order of diffraction is shown in Fig. 4.22. As frequency goes higher, the convergence rate gets faster and the ratio of diffracted pressure to geometrical acoustics pressure gets smaller.

One more realistic room was chosen to investigate the diffraction effect. This performing space has 870 seats and the volume of the space is about 5300 m^3. The geometry is shown in Fig. 4. 23 and absorption coefficients of surfaces are specified in Table 4.1. Because the measured reverberation time is about 1.5 s, the Schroeder cutoff frequency is 40 Hz. Then 63 Hz octave band and 125 Hz octave band belong to the mid frequency range. The source was located at (9.4, 0, 1.3). Five receivers were distributed on the floor seats and three points are chosen for the balcony seats; (20.0, 0, 2.0), (30.0, 1, 3.5), (25.0, 5.0, 3.1), (24.0, .10.0, 3.1), (33.0, 8.0, 3.7), (30.0, 1.0, 10.0), (30.0, 10.0, 10.0), (33.0, 8.0, 11.0).

The measurement over 24 positions was compared to the averaged simulation result over 8 positions. Figure 24 compares the acoustic measures such as reverberation time, Definition, and Clarity factors. At mid frequency ranges, the simulation including diffraction effect shows better agreement with measurement except for the reverberation time. Small variations in the decay curve due to diffraction cannot significantly change the reverberation time. The other temporal parameters related to the intelligibility show a noticeable difference. According to this result, the diffraction effect enhances the precision of simulation of an actual concert hall.

Table 4.1. Absorption coefficients of test room surfaces.

Surface and material	Octave-band center frequencies (Hz)							
	63	125	250	500	1k	2k	4k	8k
Wooden flooring	0.15	0.15	0.11	0.10	0.07	0.06	0.07	0.07
Wooden paneling	0.12	0.12	0.11	0.10	0.07	0.05	0.06	0.06
Upholstered chair	0.63	0.63	0.75	0.84	0.89	0.87	0.80	0.80
Plaster board	0.13	0.13	0.19	0.45	0.86	0.80	0.84	0.84
Mineral fiber board	0.38	0.38	0.28	0.39	0.59	0.64	0.65	.0.65
Rear wall	0.53	0.53	0.49	0.57	0.82	0.90	0.83	0.83
Ceiling	0.20	0.20	0.15	0.10	0.08	0.04	0.02	0.02

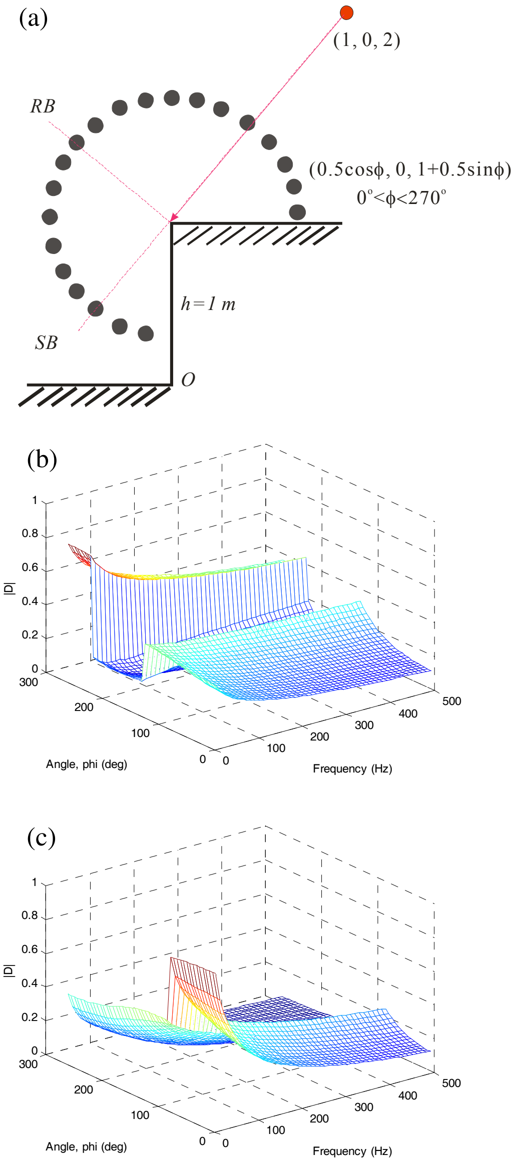

Fig. 4.1. Diffraction coefficient for the perfectly conducting step discontinuity. (a) 90° step model, (b) $|D_s|$ for single diffraction, (c) $|D_d|$ for double diffraction.

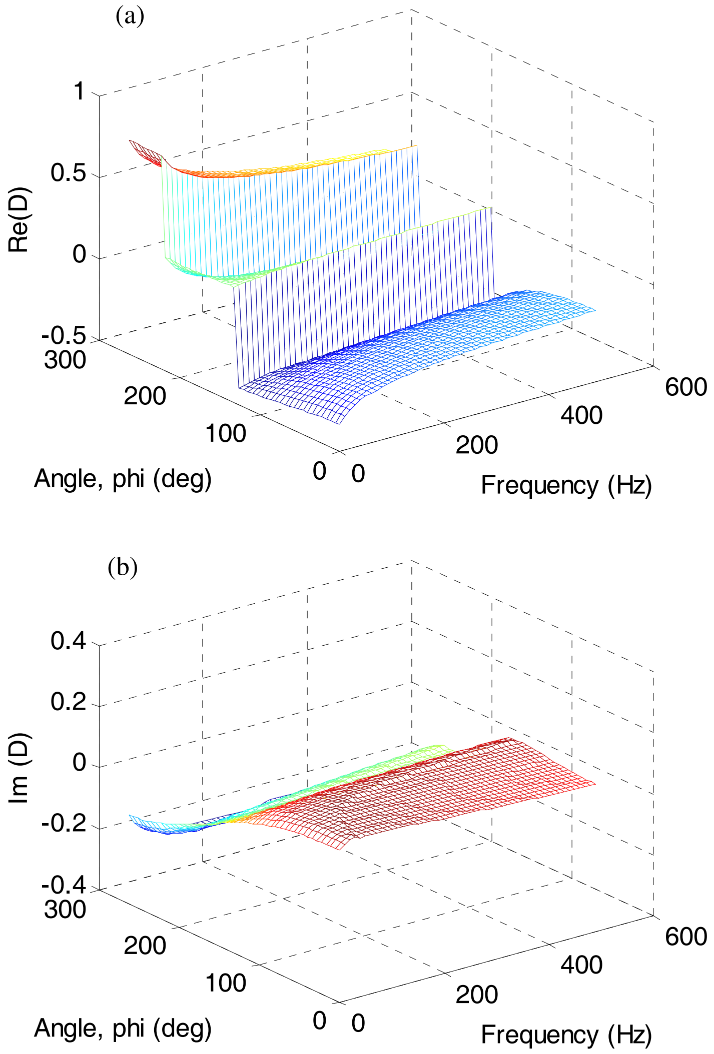

Fig. 4.2. Single diffraction coefficient for the step model in Fig. 4.1(a). (a) Re(D_s), (b) Im(D_s).

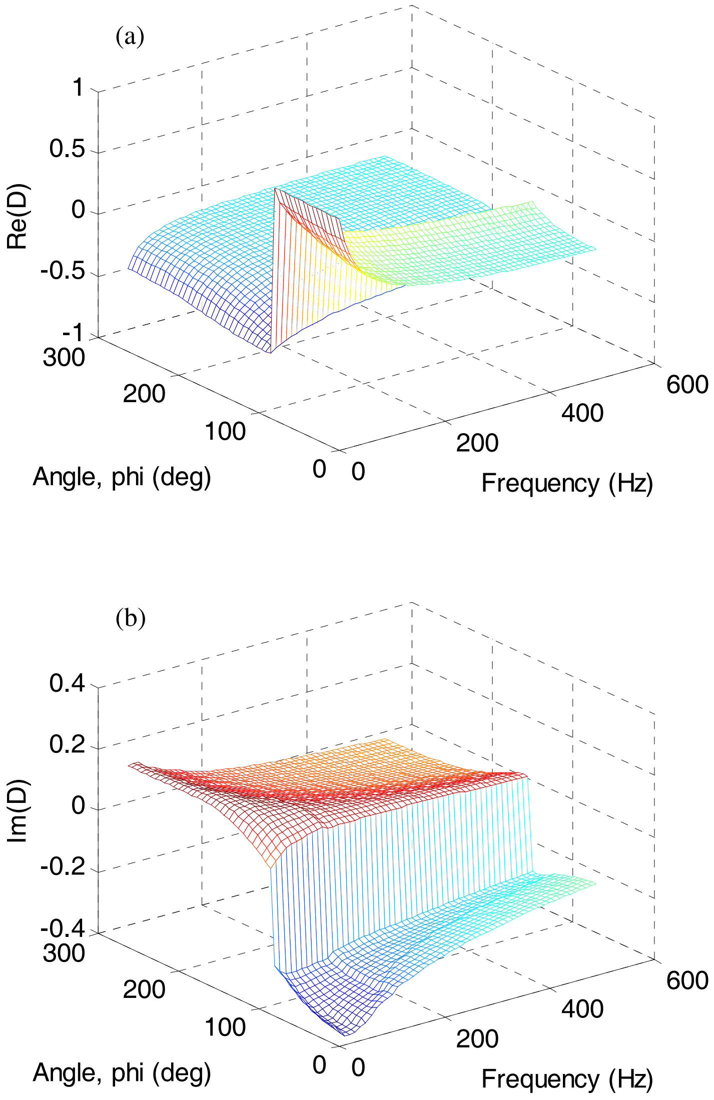

Fig. 4.3. Double diffraction coefficient for the step model in Fig. 4.1(a). (a) Re(D_d), (b) Im(D_d).

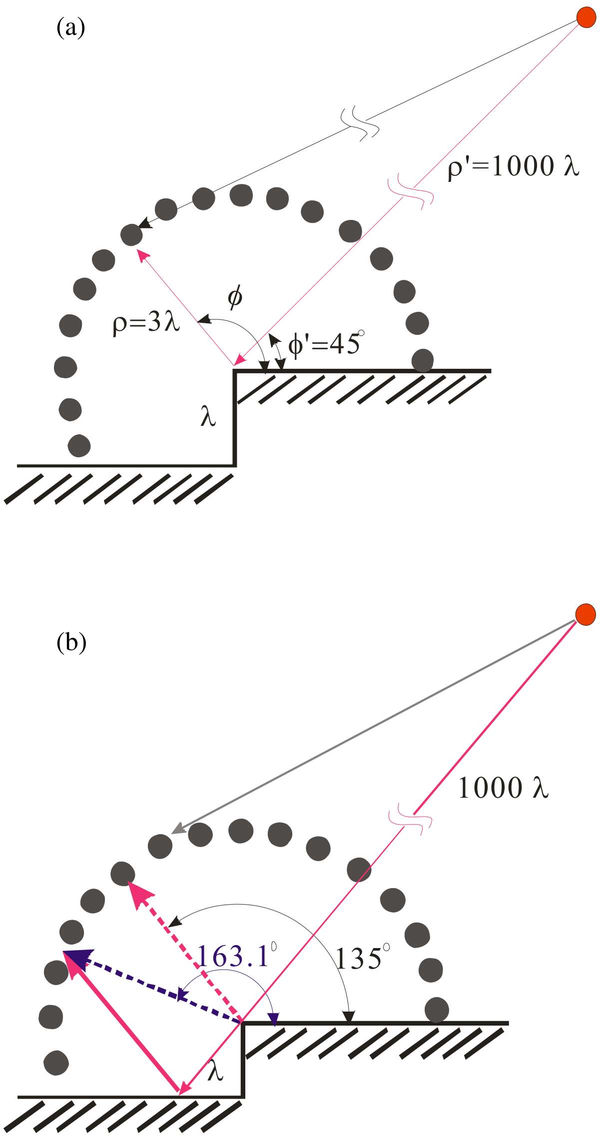

Fig. 4.4. 90˚ step model for plane wave. (a) Geometrical model, (b) limiting angles for upper and lower reflection.

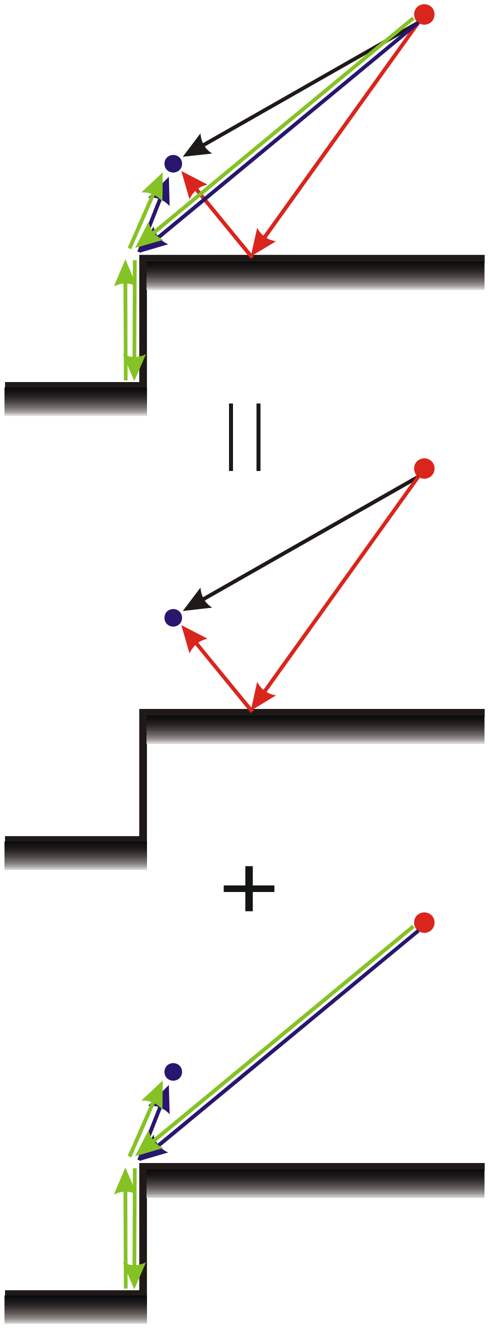

Fig. 4.5. The decomposition of sound paths from source to receiver.

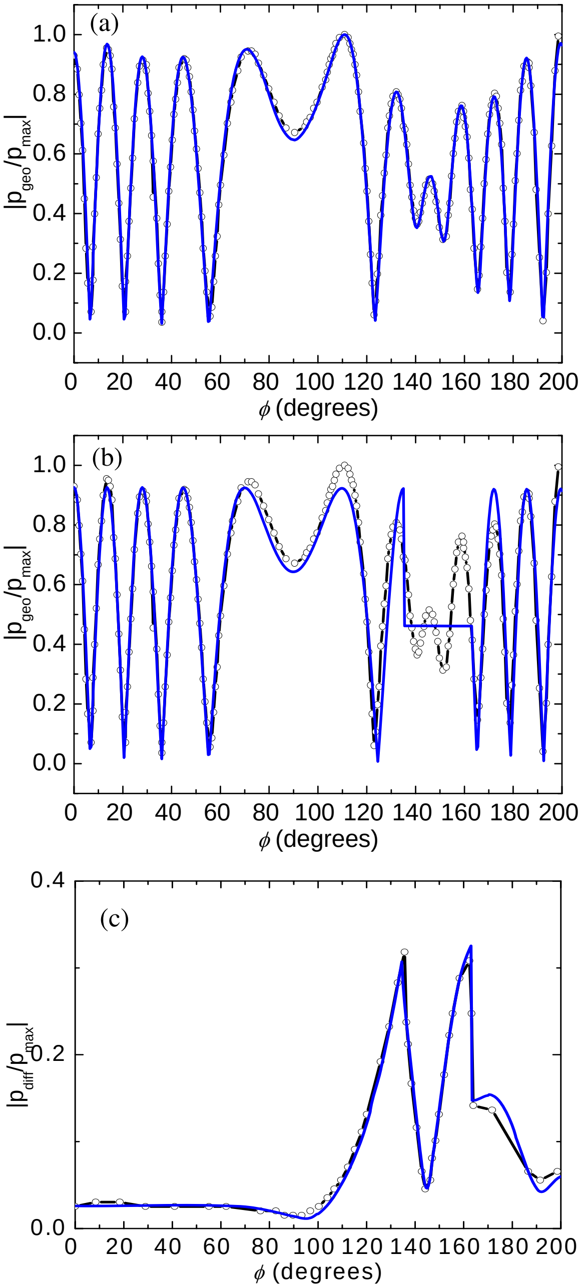

Fig. 4.6. Pressure distribution around the step discontinuity. (a) Total pressure, (b) pressure by geometrical acoustics, (c) diffracted pressure. —○—, Zhang's result [41]; ——, PBTM with UTD.

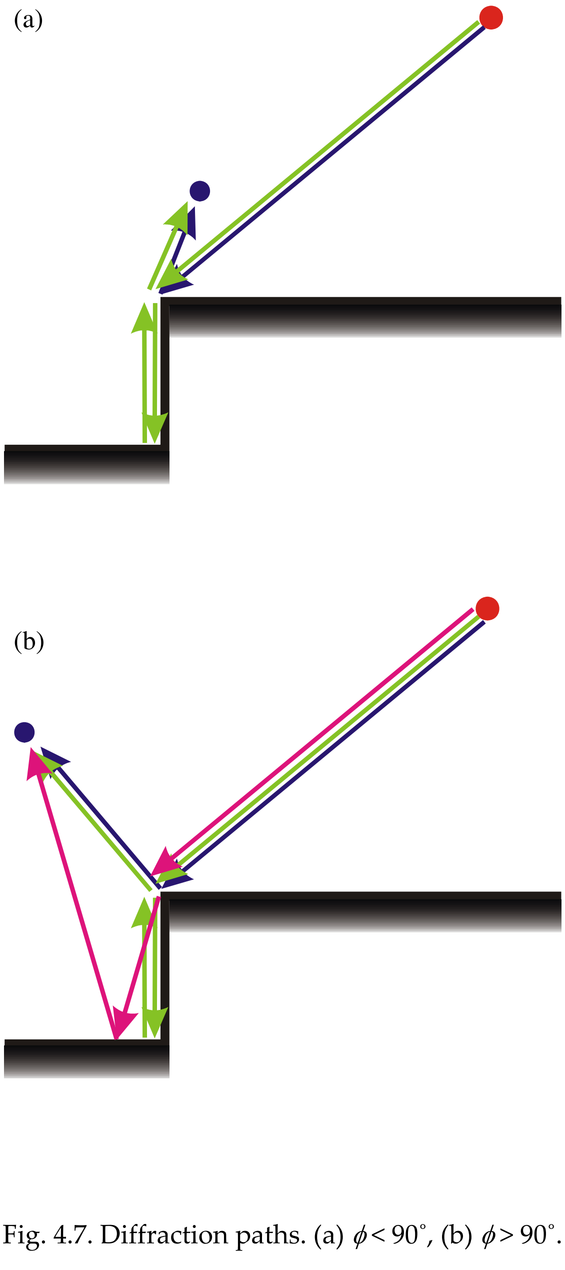

Fig. 4.7. Diffraction paths. (a) $\phi < 90^\circ$, (b) $\phi > 90^\circ$.

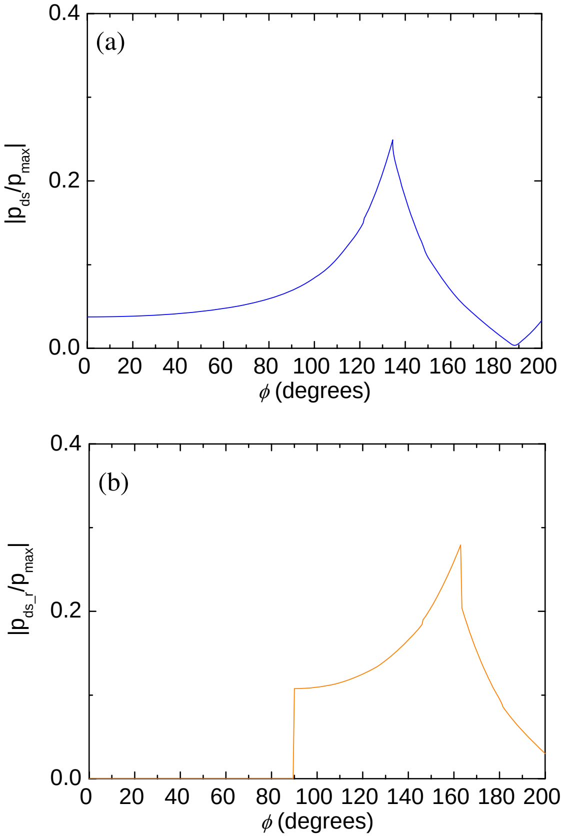

Fig. 4.8. Singly diffracted pressure distribution. (a) Singly diffracted, (b) reflection after single diffraction.

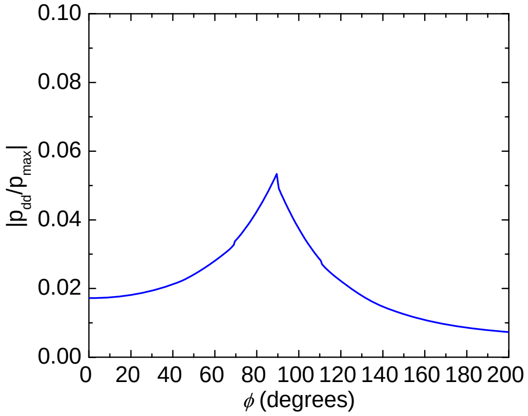

Fig. 4.9. Doubly diffracted pressure distribution.

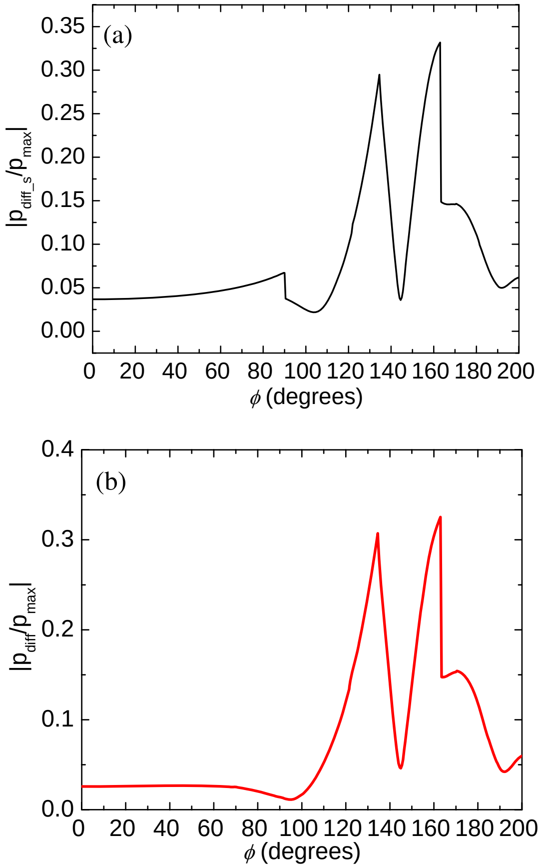

Fig. 4.10. Diffracted pressure distribution. (a) Single diffraction only, (b) overall diffraction.

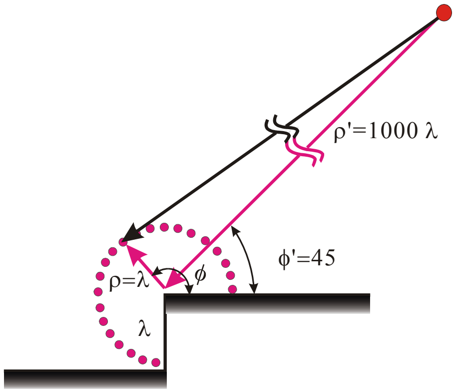

Fig. 4.11. Diffraction model to examine the diffraction near the shadow boundary.

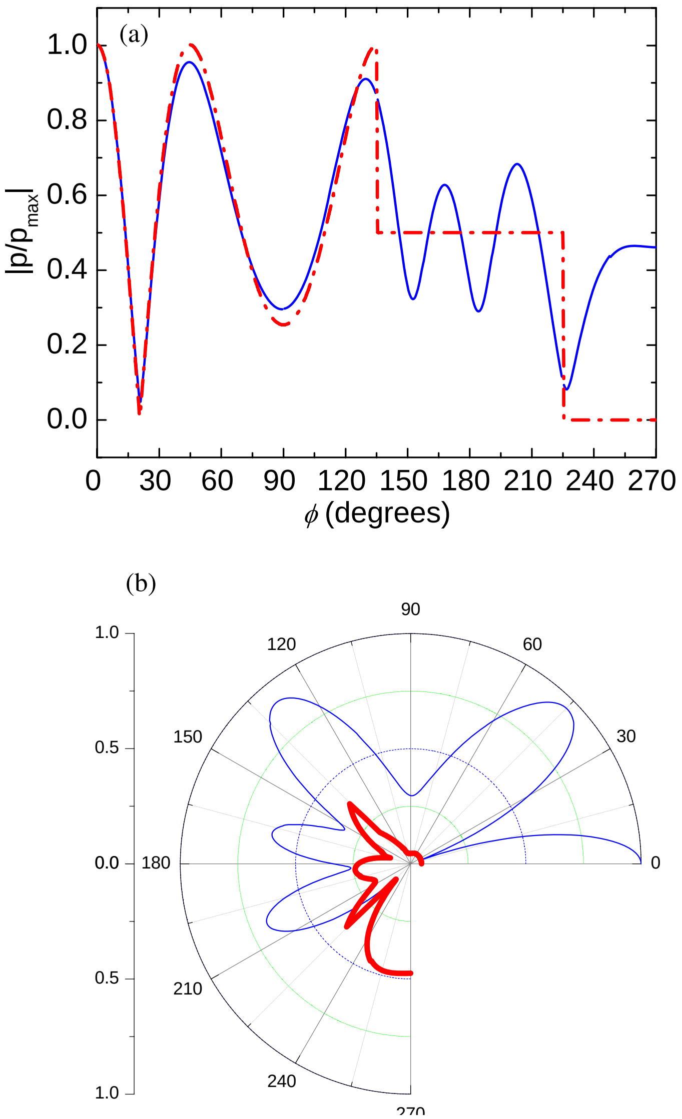

Fig. 4.12. Comparisons of calculated pressure field. (a) A comparison of total pressure between conventional PBTM and PBTM with UTD, (b) a comparison between total pressure and diffracted pressure in the polar coordinate by the PBTM with UTD. –•–, Conventional PBTM; ——, PBTM with UTD; ▬,diffraction pattern.

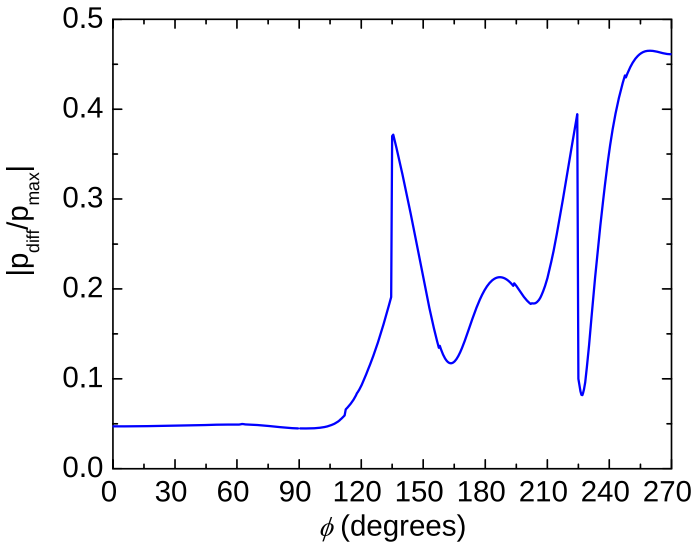

Fig. 4.13. Diffracted pressure field.

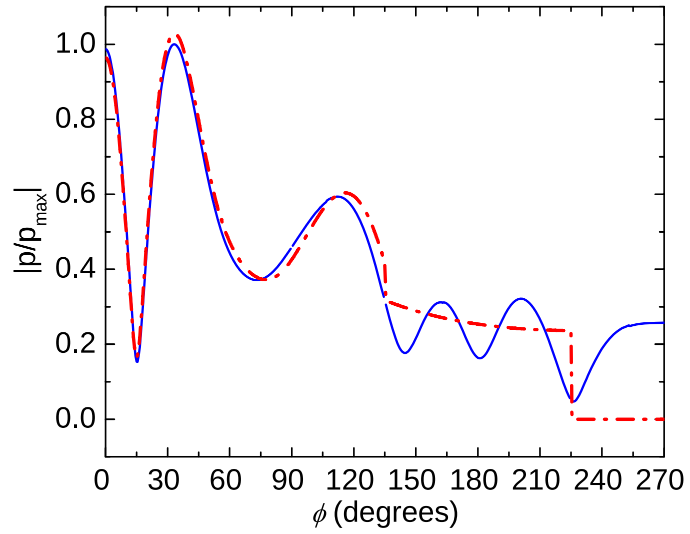

Fig. 4.14. Calculated pressure field for the spherical wave ($\rho'=2\lambda$). –•– , Conventional PBTM; ——, PBTM with UTD.

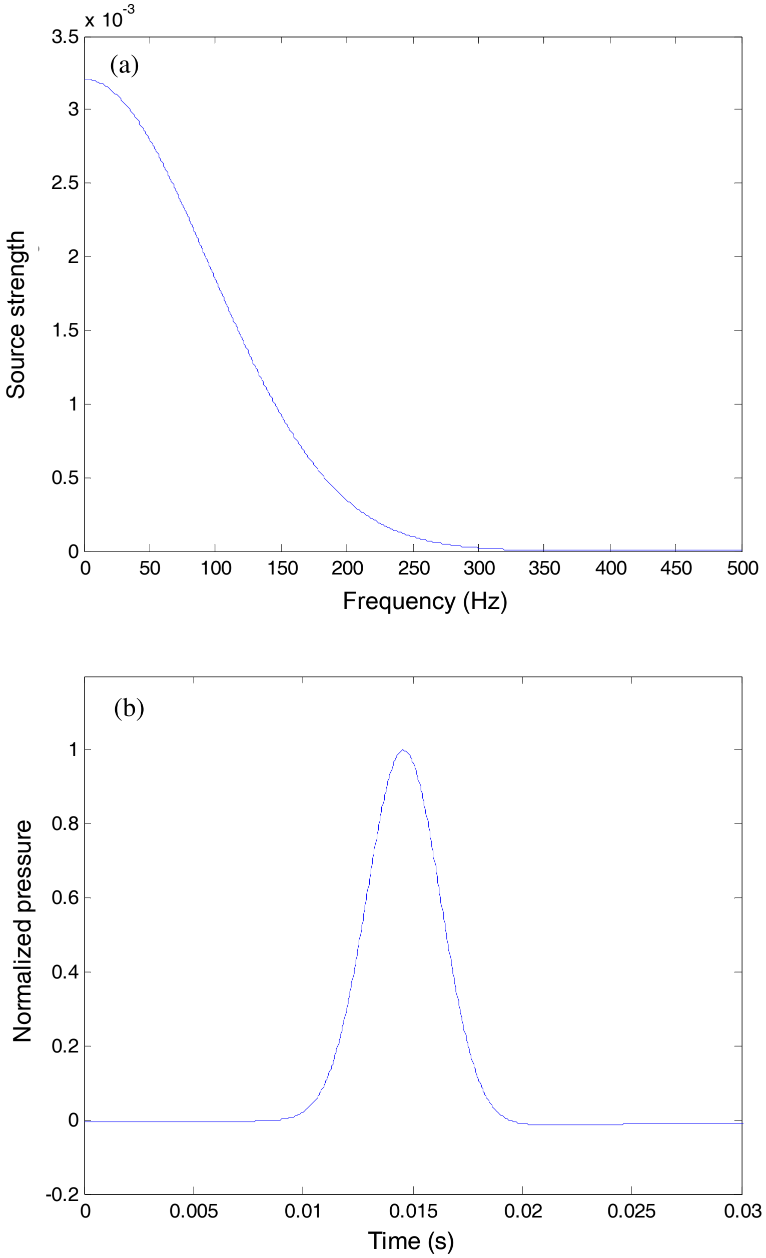

Fig. 4.15. Frequency and time domain representation of the Gabor pulse centered at 30 Hz. (a) Frequency domain, (b) time domain representation.

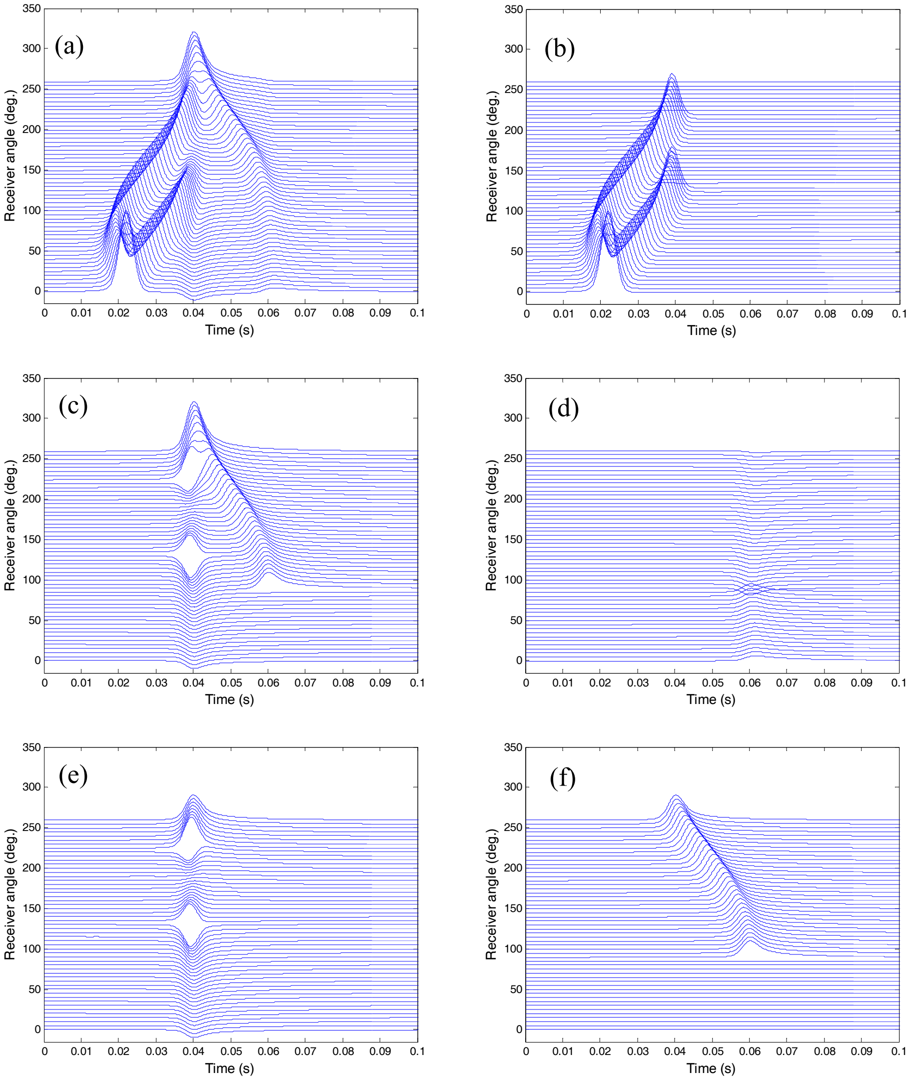

Fig. 4.16. Time domain response of diffraction model in Fig. 4.13. (a) Total response, (b) geometrical acoustics field, (c) family of single diffraction, (d) double diffraction, (e) single diffraction from the upper corner, (f) reflection after the single diffraction when $\phi \geq 90^\circ$.

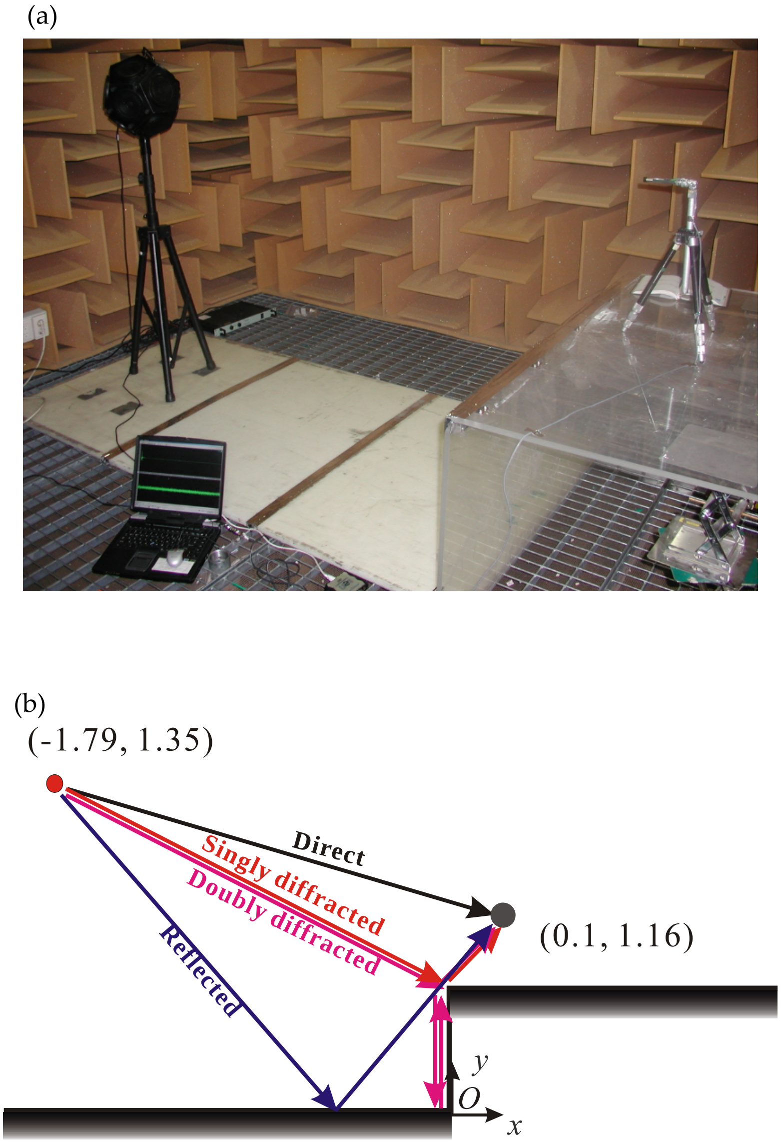

Fig. 4.17. Measurement setup and schematic drawing of the diffraction model. (a) Photo, (b) schematic drawing.

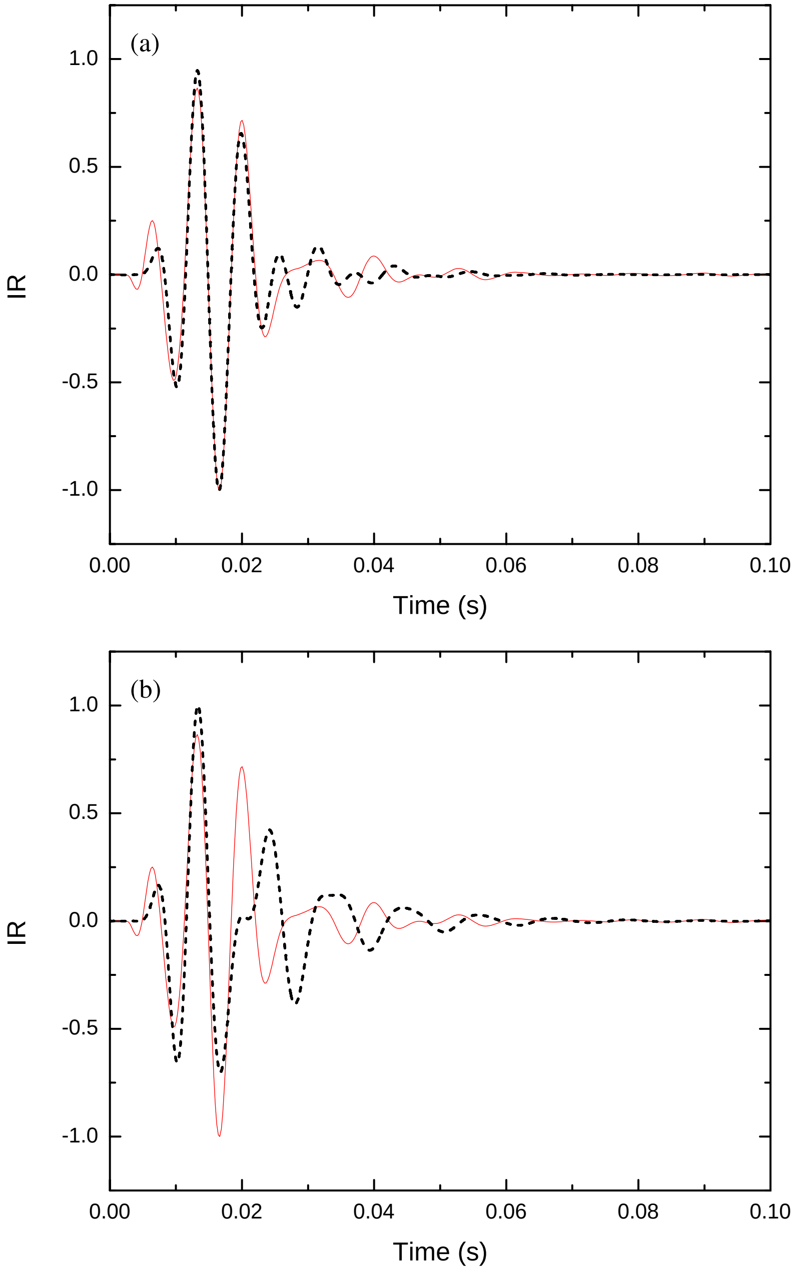

Fig. 4.18. Comparisons of impulse responses in 125 Hz octave band. (a) Diffraction included, (b) diffraction neglected. —, Measurement; - - -, PBTM with UTD.

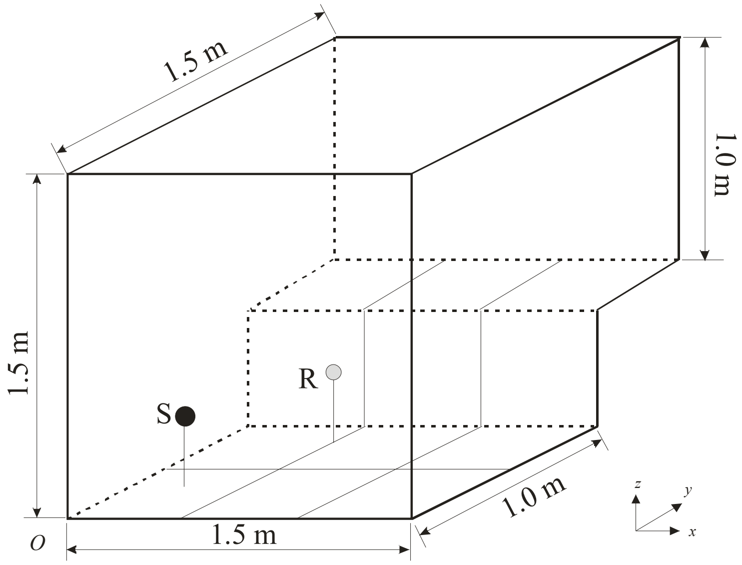

Fig. 4.19. Room model with diffracting edge.

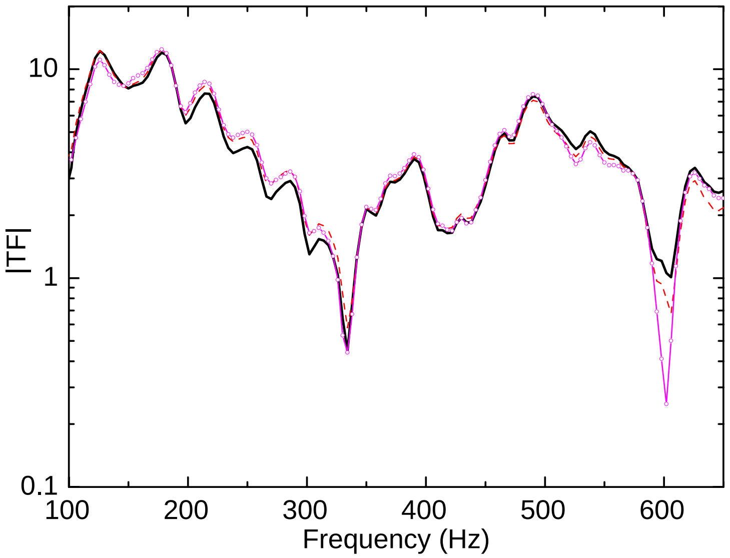

Fig. 4.20. A comparison of transfer functions according to the diffraction order at R1. ——, Without diffraction; - - - - -, diffraction order of 5; —○—, diffraction order of 7.

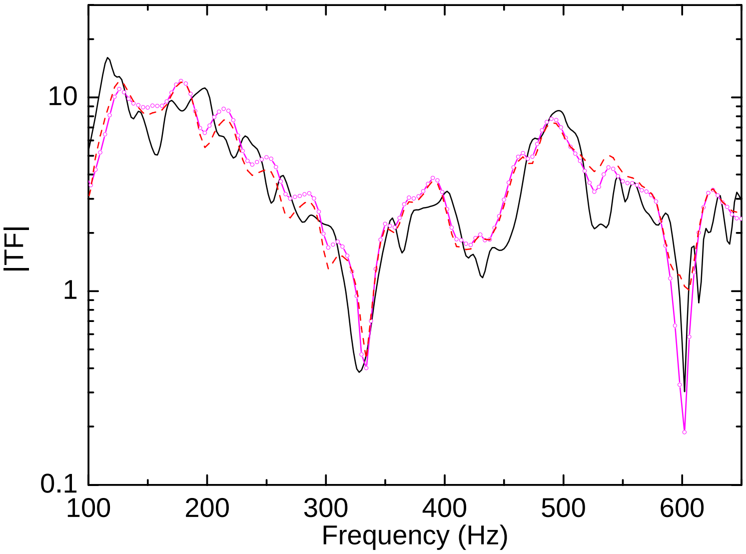

Fig. 4.21. A Comparison of transfer functions between BEM and PBTM. ▬, BEM; - - - -, diffraction neglected; —○— diffraction order of 7.

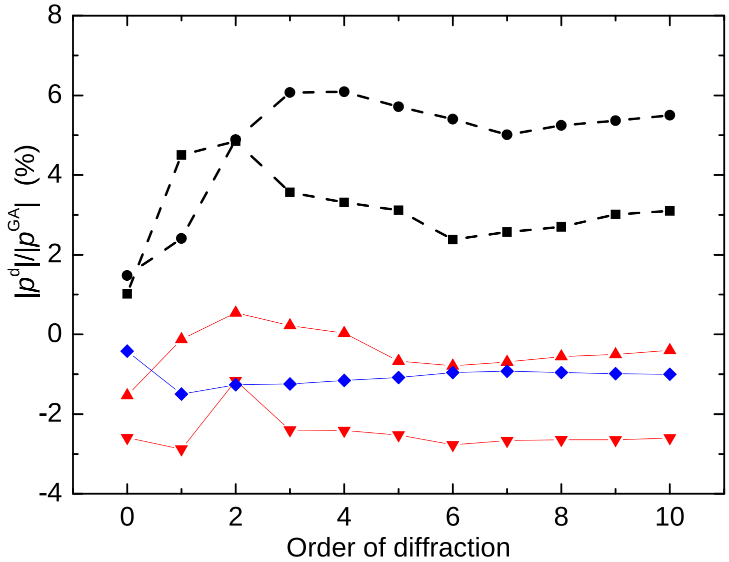

Fig. 4.22. Convergence test as a function of order of diffraction. —■—, 125 Hz octave band; —●—, 250 Hz octave band; —▲—, 500 Hz octave band; —▼—, 1 kHz octave band; —◆—, 2 kHz octave band.

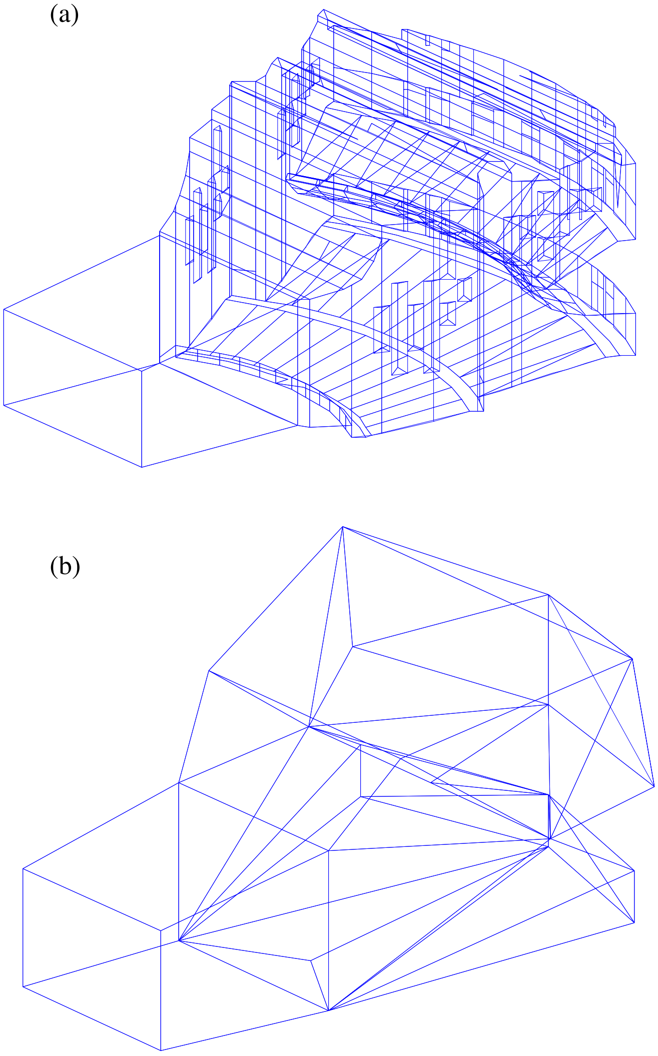

Fig. 4.23. Concert hall model. The absorption coefficients are specified in Table 4.1. (a) Detailed model, (b) simplified model.

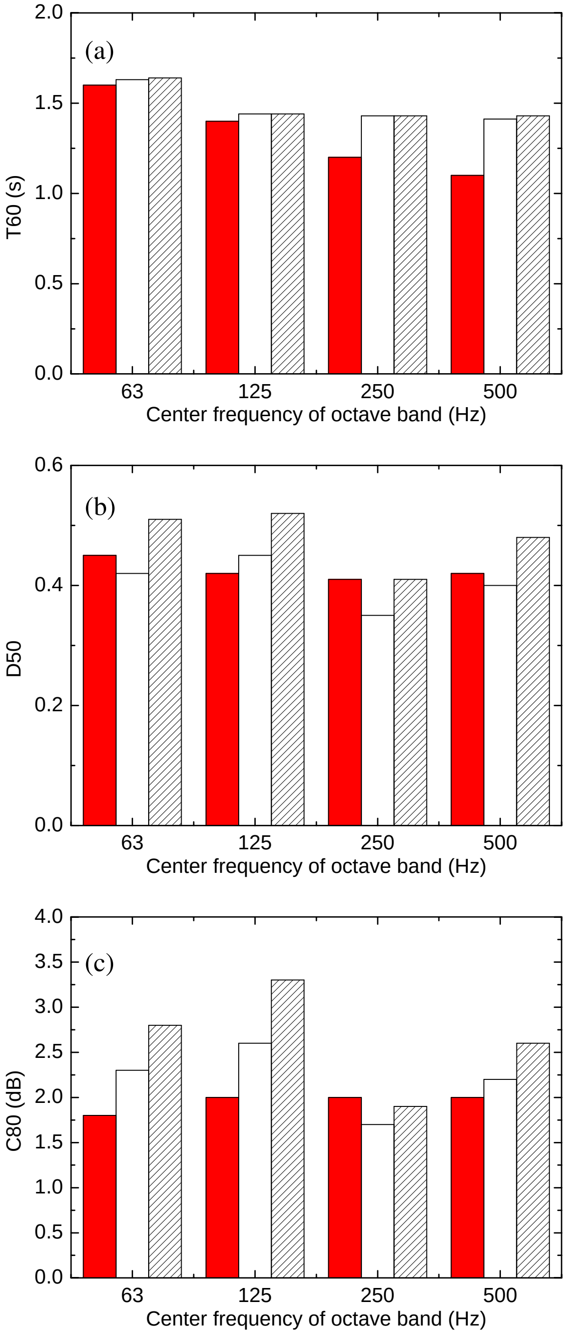

Fig. 4.24. Comparisons of acoustic parameters. (a) Reverberation time, (b) Definition, (c) Clarity. 🟥Measurement; ☐, PBTM with UTD; ▨, PBTM.

5. CONCLUSIONS AND FURTHER SUGGESTIONS

The consideration of wall reflection and diffraction in the phased beam tracing technique has been discussed to validate the present method as a mid frequency predictor in the architectural acoustics field. The main study has been focused on the improvement of precision of the present method. The phased beam tracing method, which is originated from the particle property but modified in order to explain the wave nature of the sound, has been employed in the analysis, design, diagnosis and refinement of a space.

Reflection coefficient employed in the simulation was investigated. Approximate angle-dependent/independent reflection coefficients were tested. The PBTM shows a good agreement with the measurement especially in the early part of impulse response and at mid frequency. The merit of representing the negative real part was discussed for angle-dependent reflection coefficient. Several test room models for the calculation of a transfer function, an impulse response, and acoustic measures demonstrated a good possibility for the mid frequency predictor. The calculation parameters were thoroughly investigated. The number of beams and the frequency resolution were proved to be the most important parameters in the analysis and consequently the guidelines were suggested for these parameters. The new method of binaural simulation for the PBTM was suggested. The peculiar feature of frequency domain calculation of the PBTM gives advantages in the binaural simulation. Particularity in the early part of the impulse response at mid frequency, the binaural simulation result shows an excellent correspondence with the measurement in the application of a conference room.

The diffraction phenomenon was accounted for in the PBTM by the aid of the uniform theory of diffraction for the low frequency simulation. The diffraction of edge, which is the topmost problem in an enclosed space, was tested. The simulated results by combining the PBTM with UTD agreed well with the previous research. Besides, the measurement in an anechoic chamber agreed better with the combined method than the ordinary PBTM in 125 Hz octave band. An actual concert hall was simulated by the PBTM with UTD and the results are compared with measurement in terms of acoustic parameters averaged over several receiver locations.

According to the result of PBTM in an enclosed space, the PBTM can be a mid-frequency method bridging the gap between the low frequency method and high frequency method for the room acoustic simulation. Furthermore, when a proper technique such as uniform theory of diffraction is integrated into, the present method can even deal with the low frequency range, which has been considered as the typical territory for the wave based methods for a long time. The capability of calculating a room transfer function enables this method to be used in the analysis, design, diagnosis and refinement of a space. Because the applicable frequency range was extended to low-to-mid frequency, the small-to-medium sized room can be dealt with, vise versa. Therefore a small space like vehicle cabin and aircraft cabin can be dealt with by the present method as well as a large performance space such as concert hall and theater. Besides, source identification technique based on the simulated acoustic transfer function can be applied when the noise source is located in an enclosed space. Nearfield acoustic holography based on the inverse BEM cannot be applied when the source is located in a room due to the increasing computational demands. The accurate characterization of the surface property is always essential for the improved precision. To apply this method in a practical situation, fast and efficient in-situ measurement technique for the reflection coefficient should be developed in the future.

REFERENCES

[1] A. Krokstad, S. Stroem and S. Soersdal, "Calculating the Acoustical Room Response by the Use of a Ray Tracing Technique," *Journal of Sound and Vibration* **8**, 118~125 (1968).

[2] A. Kulowski, "Algorithmic Representation of the Ray Tracing Technique," *Applied Acoustics* **18**, 449~469 (1985).

[3] P.-A. Forsberg, "Fully Discrete Ray Tracing," *Applied Acoustics* **18**, 393~397 (1985).

[4] M. R. Schroeder, "Digital Simulation of Sound Transmission in Reverberant Spaces," *Journal of the Acoustical Society of America* **47**, 424~431 (1970).

[5] J. H. Rindel, "The Use of Computer Modeling in Room Acoustics," *Journal of Vibroengineering* **3**, 219~224 (2002).

[6] D. Maercke and J. Martin, "The Prediction of Echograms and Impulse Responses within the Epidaure Software," *Applied Acoustics* **38**, 93~114 (1993).

[7] T. Lewers, "A Combined Beam Tracing and Radiant Exchange Computer-Model of Room Acoustics," *Applied Acoustics* **38**, 161~178 (1993).

[8] J. B. Allen and D. A. Berkley, "Image Method for Efficiently Simulating Small-Room Acoustics," *Journal of the Acoustical Society of America* **65**, 943~950 (1979).

[9] J. Borish, "Extension of the Image Model to Arbitrary Polyhedra," *Journal of the Acoustical Society of America* **75**, 1827~1836 (1984).

[10] H. Lee and B.-H. Lee, "An Efficient Algorithm for the Image Model Technique," *Applied Acoustics* **24**, 87~115 (1988).

[11] J. H. Rindel, "Modeling in Auditorium Acoustics - from Ripple Tank and Scale Model to Computer Simulation," *Revista de Acustica* **33**, 31~35 (2002).

[12] M. Vorlander, "Simulation of the Transient and Steady-State Sound Propagation in Rooms Using a New Combined Ray-Tracing/Image-Source Algorithm," *Journal of the Acoustical Society of America* **86**, 172~178 (1989).

[13] J. H. Rindel, "Computer Simulation Techniques for Acoustical Design of Rooms," *Acoustics Australia* **23**, 81~86 (1995).

[14] B.-I. Dalenback, "Catt-Acoustic: Image Source Modeling Augmented by Ray Tracing and Diffuse Reflections," *Applied Acoustics* **38**, 350 (1993).

[15] R. H. Lyon and R. G. DeJong, *Theory and Application of Statistical Energy Analysis* (Butterworth-Heinemann, Boston, 1995), pp. 42,146.

[16] R. H. Lyon and G. Maidanik, "Power Flow between Linearly Coupled Oscillators," *Journal of the Acoustical Society of America* **34**, 640~647 (1962).

[17] D. J. Nefske and S. H. Sung, "Power Flow Finite Element Analysis of Dynamic System: Basic Theory and Application to Beams," *Journal of Vibration, Acoustics, Stress, and Reliablity in Design, Transaction of American Society of Mechanical Engineers* **111**, 94~100 (1989).

[18] F. J. Fahy, *Sound and Structural Vibration: Radiation, Transmission and Response* (Academic Press, London, 1985), pp. 27, 35.

[19] M. R. Schroeder and H. Kuttruff, "On Frequency Response Curves in Rooms: Comparison of Experimental, Theoretical, and Monte Carlo Results for the Average Frequency Spacing between Maxima," *Journal of the Acoustical Society of America* **34**, 76~80 (1962).

[20] E. D. Geest and H. Patzold, "Comparison between Room Transmission Functions Calculated with a Boundary Element Method and a Ray Tracing Method Including

Phase," *Proceedings of Inter-Noise 96*, 3177~3180 (1996).

[21] H.-C. Shin and J.-G. Ih, "Acoustic Analysis of Interior Spaces by Using the Phased Geometric Acoustic Model," *Journal of the Acoustical Society of Korea* **17**, 54~61 (1998), (In Korean).

[22] Y. W. Lam, "Modelling Room Acoustics in Non-Concert Hall Settings," Proceedings of RADS 2004, CD-ROM (2004).

[23] A. Wareing and M. Hodgson, "Beam-Tracing Model for Predicting Sound Field in Rooms with Multilayer Bounding Surfaces," *Journal of the Acoustical Society of America* **118**, 2321~2331 (2005).

[24] S. M. Dance, J. P. Roberts and B. M. Shield, "Computer-Prediction of Sound Distribution in Enclosed Spaces Using an Interference Pressure Model," *Applied Acoustics* **44**, 53~65 (1995).

[25] J. S. Suh and P. A. Nelson, "Measurement of Transient Response of Rooms and Comparison with Geometrical Acoustic Models," *Journal of the Acoustical Society of America* **105**, 2304~2317 (1999).

[26] X. Y. Zeng, K. A. Chen and J. C. Sun, "Modeling the Sound Fields in Rooms with Multiple Sources Using a Hybrid Image Method Including Phase," *Acta Acustica united with Acustica* **88**, 88~92 (2002).

[27] H. Lehnert, "Systematic-Errors of the Ray-Tracing Algorithm," *Applied Acoustics* **38**, 207~221 (1993).

[28] L. N. Yang and B. M. Shield, "Development of a Ray Tracing Computer Model for the Prediction of the Sound Field in Long Enclosures," *Journal of Sound and Vibration* **229**, 133~146 (2000).

[29] X. Y. Zeng, K. A. Chen and J. C. Sun, "On the Accuracy of the Ray-Tracing Algorithms Based on Various Sound Receiver Models," *Applied Acoustics* **64**, 433~441 (2003).

[30] C. L. Christensen, *Odeon Room Acoustics Program* (ODEON A/S, 2003), p. 8-63.

[31] A. Farina, "Ramsete - a New Pyramid Tracer for Medium and Large Scale Acoustic Problems," *Proceedings of Euronoise 95*, 55~60 (1995).

[32] U. Stephenson and U. Kristiansen, "Pyramidal Beam Tracing and Time Dependent Radiosity," *Proceedings of ICA 95*, 657~659 (1995).

[33] I. A. Drumm and Y. W. Lam, "The Adaptive Beam-Tracing Algorithm," *Journal of the Acoustical Society of America* **107**, 1405~1412 (2000).

[34] N. Campo, P. Rissone and M. Toderi, "Adaptive Pyramid Tracing: A New Technique for Room Acoustics," *Applied Acoustics* **61**, 199~221 (2000).

[35] T. Funkhouser, N. Tsingos, I. Carlbom, G. Elko, M. Sondhi, J. E. West, G. Pingali, P. Min and A. Ngan, "A Beam Tracing Method for Interactive Architectural Acoustics," *Journal of the Acoustical Society of America* **115**, 739~756 (2004).

[36] M. A. Biot and I. Tolstoy, "Formulation of Wave Propagation in Infinite Media by Normal Coordinates with an Application to Diffraction," *Journal of the Acoustical Society of America* **29**, 381~391 (1957).

[37] H. Medwin, "Shadowing by Finite Noise Barrier," *Journal of the Acoustical Society of America* **69**, 1060~1064 (1981).

[38] M. Born and E. Wolf, *Principles of Optics* (Cambridge University Press, London, 1997), p. 417.

[39] N. Tsingos, T. Funkhouser, A. Ngan and I. Carlbom, "Modeling Acoustics in Virtual Environments Using the Uniform Theory of Diffraction," *Proceedings of ACM*

SIGGRAPH, CD-ROM (2001).

[40] U. P. Svensson and R. I. Fred, "An Analytic Secondary Source Model of Edge Diffraction Impulse Responses," *Journal of the Acoustical Society of America* **106**, 2331~2344 (1999).

[41] Q. Zhang, E. V. Jull and M. J. Yedlin, "Acoustic Pulse Diffraction by Step Discontinuities on a Plane," *Geophysics* **55**, 749~756 (1990).

[42] G. A. Suedan and E. V. Jull, "Scalar Beam Diffraction by a Wide Circular Aperture," *Journal of the Optical Society of America* **5**, 1629-1634 (1988).

[43] J. B. Keller, "Geometrical Theory of Diffraction," *Journal of the Optical Society of America* **52**, 116-130 (1962).

[44] J. P. Chambers and Y. H. Berthelot, "Time-Domain Experiments on the Diffraction of Sound by a Step Discontinuity," *Journal of the Acoustical Society of America* **96**, 1887~1891 (1994).

[45] R. D. Spence, "A Note on the Kirchhoff Approximation in Diffraction Theory," *Journal of the Acoustical Society of America* **21**, 98~100 (1949).

[46] A. D. Pierce, *Acoustics: An Introduction to Its Physical Principles and Applications* (Acoustical Society of America, New York, 1994), pp. 214, 293~294.

[47] A. D. Pierce, "Diffraction of Sound around Corners and over Wide Barriers," *Journal of the Acoustical Society of America* **55**, 941~955 (1974).

[48] R. G. Kouyoumjian and P. H. Pathak, "A Uniform Geometrical Theory of Diffraction for an Edge in a Perfectly Conducting Surface," *Proceedings of the IEEE* **62**, 1448-1461 (1974).

[49] E. D. Geest and R. Garcea, "Simulation of Room Transmission Functions Using a Triangular Beam Tracing Computer Model," *Workshop on applications of signal processing to audio and acoustics*, 3177~3180 (1995).

[50] A. M. Ondet and J. L. Barby, "Modeling of Sound Propagation in Fitted Workshops Using Ray Tracing," *Journal of the Acoustical Society of America* **85**, 787~796 (1989).

[51] K. M. Li and K. K. Iu, "Propagation of Sound in Long Enclosures," *Journal of the Acoustical Society of America* **116**, 2759~2770 (2004).

[52] P. M. Lam and K. M. Li, "The Predicted Reverberation Time in an Rectangular Long Enclosure," *Proceedings of Inter-Noise 2004*, CD-ROM (2004).

[53] H. Kuttruff, "Sound Fields in Small Rooms," *Proceedings of 15th AES*, 11~15 (1998).

[54] C.-H. Jeong and J.-G. Ih, "High Frequency Vibration Analysis of Curved Beam Structures by Using the Ray Tracing Method," *Proceedings of 8th RASD*, CD-ROM (2003).

[55] C. H. Jeong, *A Study on the High Frequency Vibration Analysis of Curved Beam Structures by Using the Ray Tracing Method*, Master Thesis, Department of the Mechanical Engineering, KAIST (2002), (In Korean).

[56] A. Farina, "Verification of the Accuracy of the Pyramid Tracing Algorithm by Comparison with Experiments of Objective Acoustic Parameters," *Proceedings of ICA 95*, 445~448 (1995).

[57] U. M. Stephenson, "Quantized Pyramidal Beam Tracing - a New Algorithm for Room Acoustics and Noise Immission Prognosis," *Acustica* **82**, 517-525 (1996).

[58] A. Kulowski, "Error Investigation for the Ray Tracing Technique," *Applied Acoustics* **15**, 263~274 (1982).

[59] J. S. Bendat, "Statistical Errors in Measurement of Coherence Functions and

Input/Output Quantities," *Journal of Sound and Vibration* **59**, 405~421 (1978).
[60] Y. Park, "Improved Estimation of Frequency Response Function," *International Journal of Analytical and Experimental Modal Analysis* **9**, 99~110 (1994).
[61] S.-H. Jang and J.-G. Ih, "Random Errors for an Improved Frequency Response Function Estimator," *Mechanical Systems and Signal Processing* **11**, 323~326 (1997).
[62] H. Kuttruff, *Room Acoustics* (Spon press, New York, 2000), p. 49.
[63] M. Tohyama, R. H. Lyon and T. Koike, "Phase Variabilities and Zeros in a Reverberant Transfer Function," *Journal of the Acoustical Society of America* **95**, 286~296 (1994).
[64] M. Tohyama and R. H. Lyon, "Zeros of a Transfer Function in a Multi-Degree-of-Freedom Vibrating System," *Journal of the Acoustical Society of America* **86**, 1854~1863 (1989).
[65] M. Toyama, H. Suzuki and Y. Ando, *The Nature and Technology of Acoustic Space* (Academic Press, Tokyo, 1995), Chapter 3.5.
[66] M. Tohyama, R. H. Lyon and T. Koike, "Reverberation Phase in a Room and Zeros in the Complex Frequency Plane," *Journal of the Acoustical Society of America* **89**, 1701~1707 (1991).
[67] M. R. Schroeder, "New Method of Measuring Reverberation Time," *Journal of the Acoustical Society of America* **37**, 409~412 (1965).
[68] Anon., ISO 3382-1 *Acoustics - Measurement of Room Acoustic Parameters - Part 1: Performance Spaces* (2005).
[69] Anon., ISO 18233 *Acoustics - Application of New Measurement Methods in Building and Room Acoustics* (2006).
[70] A. V. Oppenheim and R. W. Schafer, *Discrete-Time Signal Processing* (Prentice Hall, 1999), *p*. 583.
[71] J. W. S. Rayleigh, *The Theory of Sound* (Dover, New York, 1896), Secs. 270,278, 302.
[72] I. Rudnick, "The Propagation of an Acoustic Wave Along a Boundary," *Journal of the Acoustical Society of America* **19**, 348~356 (1947).
[73] U. Ingard, "On the Reflection of a Spherical Sound Wave from an Infinite Plane," *Journal of the Acoustical Society of America* **23**, 329~335 (1951).
[74] J. H. Rindel, "Modeling the Angle-Dependent Pressure Reflection Factor," *Applied Acoustics* **38**, 223~234 (1993).
[75] H. Sato, "On the Mechanism of Outdoor Noise Transmission through Walls and Windows," *Journal of the Acoustical Society of Japan* **29**, 509~516 (1973).
[76] K. Attenborough, "Review of Ground Effects on Outdoor Sound Propagation from Continuous Broadband Source," *Applied Acoustics* **24**, 289~319 (1988).
[77] S.-H. Jang and J.-G. Ih, "On the Multiple Microphone Method for Measuring in-Duct Acoustic Properties in the Presence of Mean Flow," *Journal of the Acoustical Society of America* **103**, 1520~1526 (1998).
[78] Anon., ISO 3382 *Acoustics - Measurement of Reverberation Time of Rooms with Reference to Other Acoustical Parameters* (1997).
[79] A. Loevstad and U. P. Svensson, "Diffracted Sound Field Form an Orchestra Pit," *Proceedings of RADS 2004*, (2004).
[80] C. I. Chessell, "Propagation of Noise Along a Finite Impedance Boundary," *Journal of the Acoustical Society of America* **62**, 825~834 (1977).
[81] T. F. W. Embleton, J. E. Piercy and N. Olson, "Outdoor Sound Propagation over

Ground of Finite Impedance," *Journal of the Acoustical Society of America* **59**, 267~277 (1976).

[82] A. R. Wenzel, "Propagation of Waves Along an Impedance Boundary," *Journal of the Acoustical Society of America* **55**, 956~963 (1974).

[83] J. H. Rindel, "Evaluation of Room Acoustic Qualities and Defects by Use of Auralization," *Proceedings of 148th meeting of the ASA*, 1pAA1 (2004).

[84] J. Blauert, *Spatial Hearing: The Psychophysics of Human Sound Localization* (The MIT Press, Cambridge, 1997), p. 372.

[85] H. Lehnert and J. Blauert, "Principles of Binaural Room Simulation," *Applied Acoustics* **36**, 259~291 (1992).

[86] U. P. Svensson, "Modelling Room Acoustics," *Proceedings of Baltic-Nordic Acoustical meeting*, i03 (2004).

[87] H. Kuttruff, "A Simple Iteration Scheme for the Computation of Decay Constant in Enclosures with Diffusely Reflecting Boundaries," *Journal of the Acoustical Society of America* **98**, 288-293 (1995).

[88] A. L. Bot and A. Bocquillet, "Comparison of an Integral Equation on Energy and the Ray-Tracing Technique in Room Acoustics," *Journal of the Acoustical Society of America* **108**, 1732~1740 (2000).

[89] R. N. Miles, "Sound Field in a Rectangular Enclosure with Diffusely Reflecting Boundaries," *Journal of Sound and Vibration* **92**, 203~226 (1997).

[90] A. W. Mills, "On the Minimum Audible Angle," *Journal of the Acoustical Society of America* **30**, 237~246 (1958).

[91] J. H. Rindel and C. L. Christensen, "Room Acoustic Simulation and Auralization - How Close Can We Get to the Real Room?," *Proceedings of WESPAC 8*, 1025J (2003).

[92] J. Martin and J. P. Vian, "Binaural Sound Simulation of Concert Halls by a Beam Tracing Method," *Proceedings of 13th ICA*, 253~256 (1989).

[93] J. Martin, D. V. Maercke and J.-P. Vian, "Binaural Simulation of Concert Halls: A New Approach for the Binaural Reverberation Process," *Journal of the Acoustical Society of America* **94**, 3255~3264 (1993).

[94] J.-P. Vian and J. Martin, "Binaural Room Acoustics Simulation: Practical Uses and Applications," *Applied Acoustics* **36**, 293~305 (1992).

[95] J. E. Summers, "Frequency-Dependent Models of Sound Field in Coupled-Room Concert Halls," *Proceedings of WESPAC 9*, CD-ROM (2006).

[96] K. Shin and Y. Park, "Measurement and Analysis of the near-Field Hrtf for Virtual Audio Enhancement," *Proceedings of Autumn Meeting of ASK*, 335-338 (2004), (In Korean).

[97] R. R. Torres, U. P. Svensson and M. Kleiner, "Computation of Edge Diffraction for More Accurate Room Acoustics Auralization," *Journal of the Acoustical Society of America* **109**, 600~610 (2001).

[98] T. Lokki, U. P. Svensson and L. Savioja, "An Efficient Auralization of Edge Diffraction," *Audio Engineering Society*, 166-171 (2002).

[99] U. P. Svensson, "Numerical Aspects of Edge Diffraction Impulse Response," *Proceedings of RADS 2004*, CD-ROM (2004).

[100] R. R. Torres, M. Kleinver and N. Xiang, "Evaluating Physical and Aural Accuracy in Computed Early Room Impulse Responses," *Proceedings of RADS 2004*, CD-ROM (2004).

[101] A. W. Trorey, "A Simple Theory for Seismic Diffractions," *Geophysics* **35**, 762-784

(1970).

[102] J. A. Fawcett, "Modeling of High-Frequency Scattering from Objects Using a Hybrid Kirchhoff/Diffraction Approach," *Journal of the Acoustical Society of America* **109**, 1312~1319 (2001).

[103] J. R. Berryhill, "Diffraction Response for Nonzero Separation of Source and Receiver," *Geophysics* **42**, 1158~1176 (1977).

[104] I. G. Leizer, "Applicability of the Methods of Geometric Acoustics for the Calculation of Sound Reflection from Plane Surface," *Soviet Physics - Acoustics* **12**, 180~184 (1966).

[105] E. Reboul, A. L. Bot and J. P. Liaudet, "Radiative Transfer Equation for Multiple Diffraction," *Journal of the Acoustical Society of America* **118**, 1326~13334 (2005).

[106] A. L. Bot, "Energy Exchange in Uncorrelated Ray Field of Vibroacoustics," *Journal of the Acoustical Society of America* **120**, 1194~1208 (2006).

[107] G. A. Suedan and E. V. Jull, "Beam Diffraction by Half Planes and Wedges: Uniform and Asymptotic Solutions," *Journal of Electromagnetic Waves and Applications* **3**, 17~26 (1989).

[108] A. J. Soares, A. J. Giarola and C. H. Conzalez, "Plane Wave Scattering by a Step Discontinuity in a Conducting Plane," *Proceedings of ISAE*, 235~240 (1985).

Appendix A. DISCUSSION REGARDING DUALITY OF SOUND

The present method of PBTM is the representative of the particle property, whereas the BEM [A1,A2] is the technique which emphasizes the wave property of the sound in acoustics. Except for the very simple application, the sound field is generally analyzed by discretizing boundary surfaces into tiny patches and the Kirchhoff-Helmholtz integral equation [A3,A4] is solved on the boundary of the domain. The Kirchhoff-Helmholtz integral equation is the most general solution of the radiation and scattering problems in acoustics, which represents the sound field by the monopole and dipole source distribution on a vibrating surface. The acoustic boundary element method based on the Kirchhoff-Helmholtz integral formulation has been used for a problem with irregularly shaped geometry which has no closed form solution in separable coordinate. For the exterior problem of infinite extent, the discretization can be limited to the finite boundary of the body by imposing the Sommerfeld radiation condition. In the indirect BEM, surface monopole strengths are calculated for expressing the acoustic field equivalent to that generated by the actual vibration surface the superposition integral is based on the idea that an array of monopole sources can be arranged to reproduce a velocity profile on the surface of the radiator. The Kirchhoff-Helmholtz integral equation is based on the linearized wave equation as follows:

$$\nabla^2 p(\mathbf{r},t) = \frac{1}{c_o^2}\frac{\partial^2 p(\mathbf{r},t)}{\partial t^2}, \tag{A.1}$$

where $p(\mathbf{r},t)$ is the acoustic pressure, $\mathbf{r}$ the field point. For a simple harmonic time dependence of angular frequency ω, the acoustic pressure is given by

$$p(\mathbf{r},t) = p(\mathbf{r})\exp(i\omega t). \tag{A.2}$$

Substitution of Eq. (A.2) into Eq.(A.1) yields the following Helmholtz equation:

$$\nabla^2 p(\mathbf{r}) + k^2 p(\mathbf{r}) = 0. \tag{A.3}$$

For the unbounded medium, the three-dimensional free-field Green function satisfies the wave equation as

$$\nabla^2 G(\mathbf{r},\mathbf{r}_o) + k^2 G(\mathbf{r},\mathbf{r}_o) = -4\pi\delta(\mathbf{r}-\mathbf{r}_o), \tag{A.4}$$

where $G(\mathbf{r},\mathbf{r}_o) = \exp(-jkR)/R$, $R = |\mathbf{r}-\mathbf{r}_o|$, and $\delta(\mathbf{r}-\mathbf{r}_o)$ is Dirac-delta function in three dimensional space. If the acoustic field is excited by a simple harmonic distributed surface $f(\mathbf{r})$, Helmholtz equation can be given by

$$\nabla^2 p(\mathbf{r}) + k^2 p(\mathbf{r}) = -f(\mathbf{r})\,. \tag{A.5}$$

When Eq. (A.4) and Eq. (A.5) are multiplied by $p(\mathbf{r})$ and $G(\mathbf{r},\mathbf{r}_o)$, respectively, the difference of two resultant equation is given by

$$G(\mathbf{r},\mathbf{r}_o)\nabla^2 p(\mathbf{r}) - p(\mathbf{r})\nabla^2 G(\mathbf{r},\mathbf{r}_o) = 4\pi p(\mathbf{r})\delta(\mathbf{r}-\mathbf{r}_o) - G(\mathbf{r},\mathbf{r}_o) f(\mathbf{r})\,. \tag{A.6}$$

The integration over the Volume, V, occupied by the medium as shown in Fig. A.1, the following equation is obtained

$$\int_V G(\mathbf{r},\mathbf{r}_o)\nabla^2 p(\mathbf{r}_o) - p(\mathbf{r}_o)\nabla^2 G(\mathbf{r},\mathbf{r}_o) dV = 4\pi \int_V p(\mathbf{r}_o)\delta(\mathbf{r}-\mathbf{r}_o) dV - \int_V G(\mathbf{r},\mathbf{r}_o) f(\mathbf{r}_o) dV\,\cdot \tag{A.7}$$

By virtue of the divergence theorem, the volume integral can be changed to the surface integral, as follows:

$$c(\mathbf{r})p(\mathbf{r}) = \int_{S_o} \left[p(\mathbf{r}_o)\frac{\partial G(\mathbf{r},\mathbf{r}_o)}{\partial n} - \frac{\partial p(\mathbf{r})}{\partial n} G(\mathbf{r},\mathbf{r}_o) \right] dS + \int_V G(\mathbf{r},\mathbf{r}_o) f(\mathbf{r}_o) dV\,, \tag{A.8}$$

where **r** is field point, $\mathbf{r}_o$ the surface point, the $\partial/\partial n$ the derivative in a direction normal to the surface as depicted in Fig. A.1, $c(\mathbf{r})$ the solid angle. The solid angle can be expressed as

$$c(\mathbf{r}) = \begin{cases} 4\pi & (r \in V, r \notin S_o) \\ 4\pi + \displaystyle\int_{S_o} \frac{\partial}{\partial n}\left(\frac{1}{R}\right) ds & (r \in V, r \in S_o) \\ 0 & (r \notin V, r \notin S_o) \end{cases} \cdot \tag{A.9}$$

The first term of the integrand of Eq. (A.8) can be rewritten as

$$\frac{\partial G(\mathbf{r},\mathbf{r}_o)}{\partial n} = -\left(\frac{1}{R} + ik\right)\frac{\exp(-jkR)}{R}\cos\theta, \tag{A.10}$$

where

$$\cos\theta = \frac{(\mathbf{r}-\mathbf{r}_o)\cdot n}{R}\,. \tag{A.11}$$

Conservation of momentum can be rewritten as

$$\frac{\partial p(\mathbf{r}_o)}{\partial n} = -j\omega\rho v(\mathbf{r}_o), \tag{A.12}$$

where $v(\mathbf{r}_o)$ is the normal velocity of surface point. Then the acoustic pressure at position **r** produced by the vibration of the surface S and the distributed source is given by

$$c(\mathbf{r})p(\mathbf{r}) = -\int_{S_o}\left[p(\mathbf{r}_o)\left(\frac{1}{R}+ik\right)\frac{\exp(-jkR)}{R}\cos\theta + j\omega\rho v(\mathbf{r}_o)\frac{\exp(-jkR)}{R}\right]dS \\ +\int_V G(\mathbf{r},\mathbf{r}_o)f(\mathbf{r}_o)dV. \tag{A.13}$$

The first integrand in Eq. (A.13) has the directivity of $\cos\theta$ and this means the dipole effect by the source pressure $p(\mathbf{r}_o)$. The second integrand represents the monopole effect by the surface normal velocity $v(\mathbf{r}_o)$. Figure A.2 depicts the procedure for simulating the sound field using the BEM in two steps. Figure A.2(a) depicts the calculation of surface pressure, $p(\mathbf{r}_o)$ and velocity, $v(\mathbf{r}_o)$ from the known source. The size of the circle distributed on the ceiling represents the strength of the source pressure and velocity, $p(\mathbf{r}_o)$ and $v(\mathbf{r}_o)$.

When the $p(\mathbf{r}_o)$ and $v(\mathbf{r}_o)$ are calculated, the field pressure is computed in terms of the incident sound and scattered sound; the incident sound is calculated directly from the source-receiver distance and the scattered sounds are estimated from the known surface pressure and velocity according to Eq. (A.13). It can be easily guessed that the points near the source strongly influence the scattered sound.

In the PBTM, the beams emitted from the source scan the sound field. Figure A.3 shows the conceptual drawing of the beam tracing. Similarly with BEM, the reflected beam can be considered as a newly generated beam emanating from the reflecting surface. The field pressure at the receiver is the summation of all contributions of hitting beams as follows:

$$p(\mathbf{r},t) = \sum_i p_i \frac{e^{-jkR_i}}{R_i}\cos\theta\,. \tag{A.14}$$

Here, the cosine function represents the major directivity of the beam which is determined by the Snell's law depending on the angle of incidence. Figure A.4 shows the analysis of two-dimensional sound field by PBTM. After the beam hits one local point on the ceiling, it is reflected. The reflected beam can be regarded as the newly generated beam from the surface which has a directivity of the reflected direction in Fig. A.4(a). There is only one path of detecting receiver among the reflected beams from the ceiling. It can be interpreted that only one point of the ceiling affects the pressure at the receiver point. It is completely contrast to the principle of the BEM; all the surface points should contribute in constructing a sound field.

In Fig. A.4(b), one shaded beam meets the ceiling and floor, successively, and detects the receiver. It can be said that the contribution of this beam implies not only the reflection on the ceiling but also the reflection on the floor. If one imagines more successive reflections, it can be said that all surface points contribute in constructing a sound field although it is very hard to quantify the contribution of each points.

According to the Figs. A.2 and A.4, one can find the similarity between the wave based method and geometrical acoustics method. The contribution of the fictitious sources on the surface can be interpreted as that of the reflected beams. Disregarding the diffraction from the corner, BEM and PBTM should perfectly agree each other as can be seen in Fig. 2.32.

Going into the mathematical equation, the first integrand in Eq. (A.13) has the similar form with Eq. (5.14). The first term interpreted as the effect of dipole (hereafter, dipole term), is related to the surface pressure, $p(\mathbf{r}_0)$, and certain directivity. Even though the term of $\left(\frac{1}{R}+ik\right)$ is not counted in the PBTM (see Eq. (A.14)), it can be concluded that the PBTM result is similar with the dipole effect of the boundary integral when the enough number of successive reflections is considered. It should be recalled that the iterative summation of the many reflections corresponds with the exact solution in Chapter 2.1.

In the PBTM, the beam at the starting point has an initial pressure as if the room is infinitely large (or anechoic condition). Then the summation of direct component and the successive reflections constitutes the sound field. Here lies the mystery, how the sound field is constructed by summing the direct sound under the assumption of infinitely large space and following reflections from the reflection points which are determined by the geometrical searching. In this regard, the bulk reaction might be one source of the error in the present method because it is already assumed that the reflection on the surface occurs at a point of reflection.

As frequency goes higher, the reflection becomes negligible due to high absorbing characteristics of surfaces and increasing air attenuation. Also when the room becomes large, the contribution of reflected sound gets smaller. The weakly reverberant field is a proper application for the PBTM, because the direct sound overwhelms the reflected sounds. The bigger the direct sound field, the better the PBTM works. In the abovementioned conditions, the PBTM result corresponds better to the solution of wave equation. The geometrical acoustics field is assumed to be the leading term of the series expanded solution of the wave equation. In either high frequency response or weakly reverberant room, the solution of the wave equation approaches the free field Green function and the other wave phenomena such as diffraction and interference become negligible. Consequently the geometrical acoustic field, which started under the assumption of infinitely large space, corresponds well with the solution of wave equation without adding the higher order terms. As the sound field gets small and reverberant, the additional difficulties arise; the characteristics of the reflection (in other words, boundary condition) should be precisely known. From the technical point of view, the additional calculation time is required for the steady-state pressure to be stabilized (for example, see the convergence check in Fig. 2.25). The wave based method can easily deal with the rigid boundary condition by assigning the surface velocity, $v(\mathbf{r}_o)=0$, but it is difficult to be realized by the PBTM. The rigid boundary condition needs more than millions of reflections, theoretically.

One of the evidence that the PBTM is similar with the dipole term is the directivity. The monopole term has the omni-directional directivity whereas the beam has a clear directivity pattern. It is absolutely opposite the Rayleigh integral equation [A5] which employs only monopole contributions assuming that the vibrating surface is *flat* and mounted on a *rigid baffle.* Rayleigh integral approximation is expressed as follows:

$$p(\mathbf{r},t)=\frac{j\omega\rho_o}{2\pi}e^{j\omega t}\int_{S_o}\frac{v_s(\mathbf{r}_o)\mathrm{e}^{-jkR}}{R}dS\,. \tag{A.15}$$

The PBTM result is compared with dipole term and monopole term in Fig. A.5. In Fig. A.5(a), the PBTM agrees quite well with the BEM result. Here, 8000 beams and 50 reflections were employed. In Fig A.5(b), the PBTM shows a good agreement with the dipole term except for the frequency range between 300 Hz and 350 Hz and near 430 Hz. According to Fig. A.5(c), the overall shapes are quite similar to each other, but the magnitude of the monopole term is much smaller than the PBTM result. In Figs. A.5(b) and A.5(c), the dipole term is always bigger than the monopole term. It is proved that the regular shaped room without any obstacle can be predicted by the PBTM, even though the size is quite small at low frequency below 100 Hz. It should be recalled that the Schroeder cutoff frequency of this room is 387 Hz. It means that the room is too small to apply the PBTM below 400 Hz. Because the room surfaces are quite reflective, the plane wave assumption at low frequency might cause some errors as discussed in Chapter 3.1.7. It can be concluded that the most important factor in estimating the transfer function is the acoustical properties of surfaces.

REFERENCES

[A1] A. F. Seybert, B. Soenarko, F. J. Rizzo and D. J. Shippy, "An Advanced Computation Method for Radiation and Scattering of Acoustic Waves in Three Dimensions," *Journal of the Acoustical Society of America* **77**, 362~368 (1985).

[A2] B.-K. Kim, *Reconstruction of Vibroacoustic Field from Measured Pressures Using the Boundary Element Method*, Ph. D. Dissertation, Department of Mechanical Engineering, KAIST (1997).

[A3] L. E. Kinsler, A. R. Frey, A. B. Coppens and J. V. Sanders, *Fundamentals of Acoustics* (John Wiley & Sons, New York, 2000), p. 431.

[A4] T. W. Wu, *Boundary Element Acoustics - Fundamentals and Computer Codes* (WIT Press, London, 2000), p. 11.

[A5] A. D. Pierce, *Acoustics: An Introduction to Its Physical Principles and Applications* (Acoustical Society of America, New York, 1994), 214.

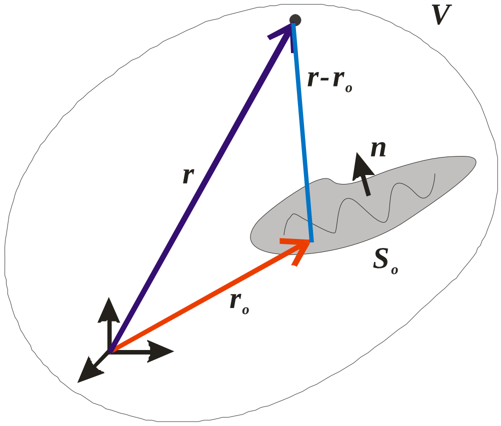

Fig. A.1. The conceptual diagram of boundary integration with arbitrary shaped vibrating surface.

(a)

Calculation of surface pressure and velocity

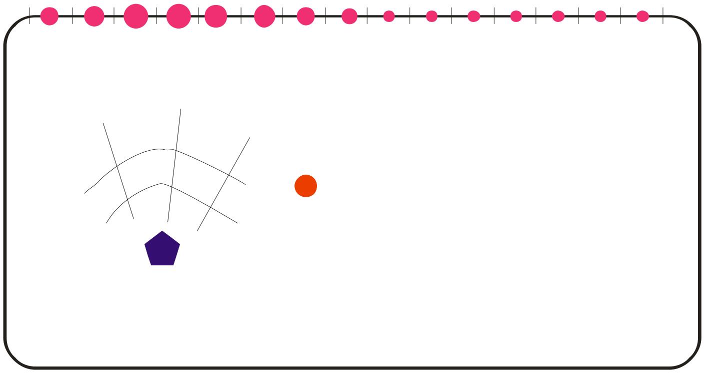

(b)

Calculation of scattered field pressure by the boundary integration in Eq. (A.13)

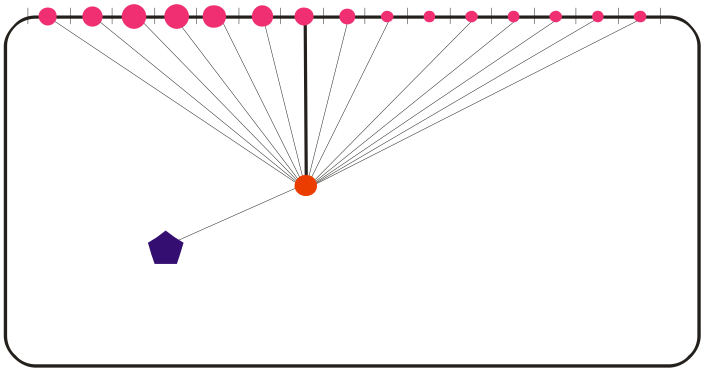

Fig. A.2. Procedure for the interior problem of BEM for two-dimensional sound field. (a) Calculation of surface pressure and velocity, (b) calculation of field pressure. The field pressure consists of incident pressure directly from the source and scattered pressures from the boundaries. ⬟ denotes the source and ● the receiver in a room. Size of the circle on the ceiling represents the strength of the surface pressure and velocity. The points near the source strongly influence the scattered sound.

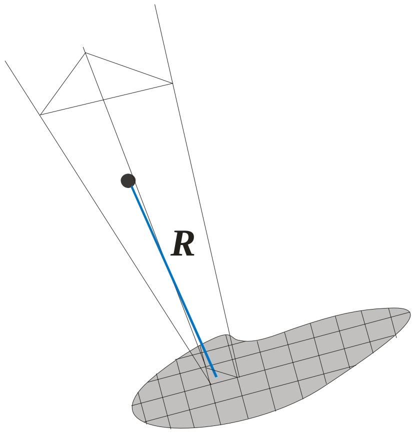

Fig. A.3. The conceptual diagram of beam tracing with arbitrary shaped vibrating surface.

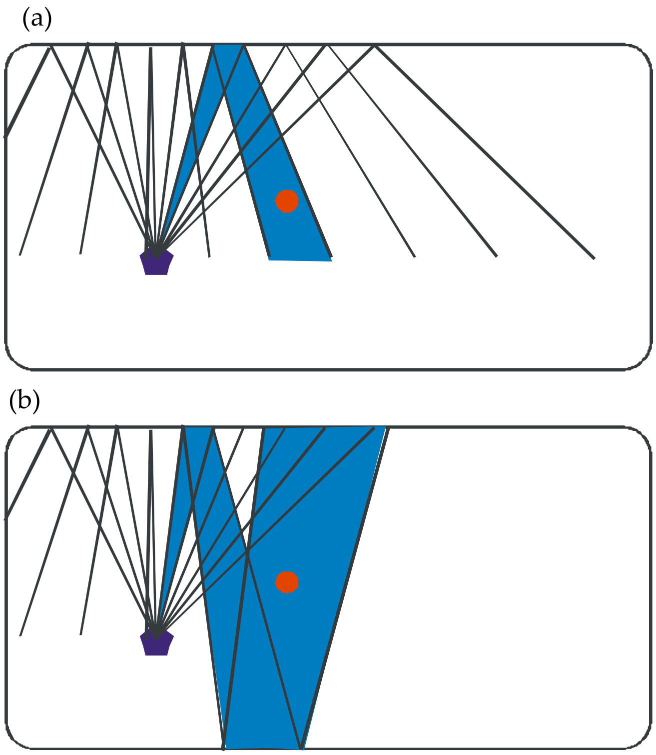

Fig. A.4. Analysis of enclosed sound field by PBTM for two-dimensional sound field. (a) Reflection path from the ceiling, (b) reflection path by hitting the ceiling and floor. ⬟ denotes the source and ● the receiver in a room.

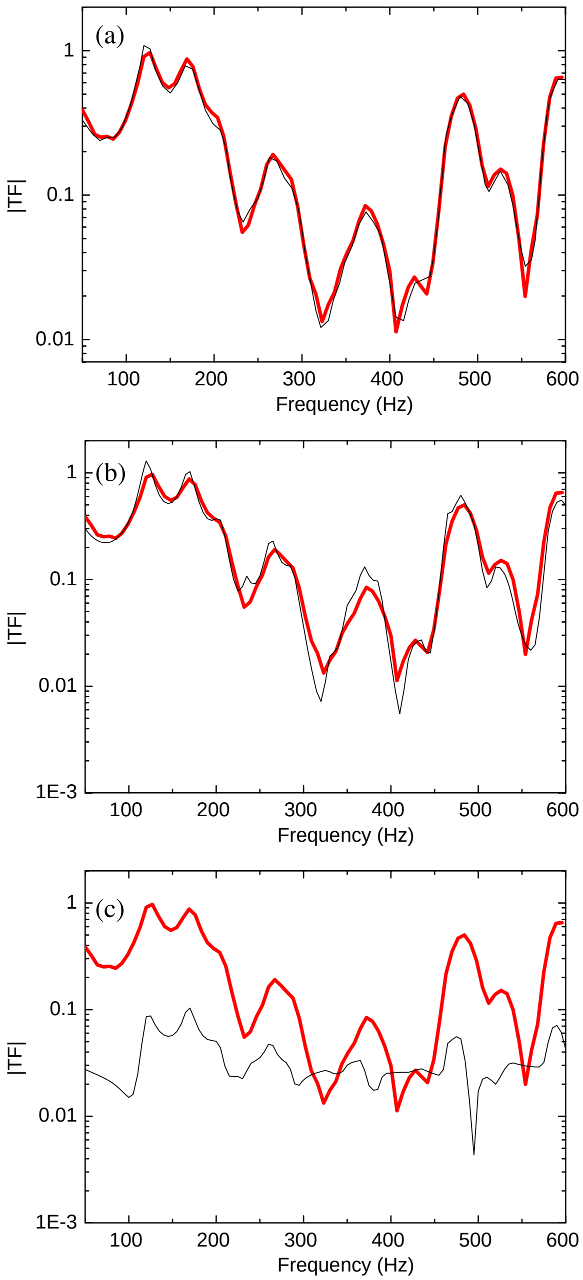

Fig. A.5. Comparison of TF between the PBTM and BEM. (a) Total TF, (b) dipole term, (c) monopole term. ▬, PBTM; ——, BEM.

Appendix. B. DIVISION OF SOURCE BASED ON THE CUBE

The usual way of dividing the source is based on the icosahedron to make each surface area of the beam more or less the same with equilateral triangles. For the evaluation, analysis and acoustic design of the sound field, the icosahedron source is quite enough. However for the modeling of the source, the source can have an arbitrary shape. In the first step, the cubic shaped source was suggested, because the general shape of the machinery can be simplified to a rectangular shaped. When the cubic source is introduced, each surface is divided into 4 isosceles triangles; the whole surface is divided into 24 isosceles triangles. One triangle can be divided into 4 sub-triangles, then the number of sections is $24\times n_s^2$. The comparison was made between the icosahedron and the cubic source. The Figure B.2 shows the comparison of TF for between the icosahedron and cubic source when n_s=2 (Fig. B.2(a)) and n_s=20 (Fig. B.2(b)) for cubic shaped room with 1.5 m edge. The source and receiver location is (0.30, 0.20, 0.10) and (1.00, 1.20, 1.45), respectively. The surface impedance is $4150+4150j$ (rayl), irrespective of frequencies. When the enough number of beams is employed, the performance of the simulation is as good as that by using the icosahedron source model.

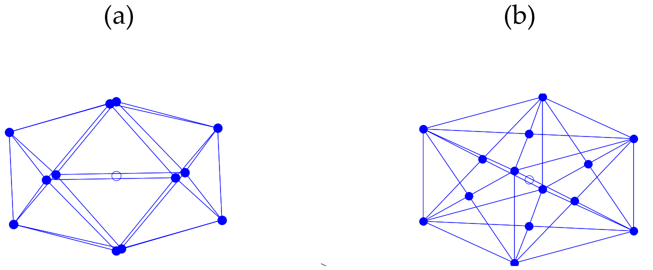

Fig. B.1. Source models. (a) Icosahedron model, (b) cubic model.

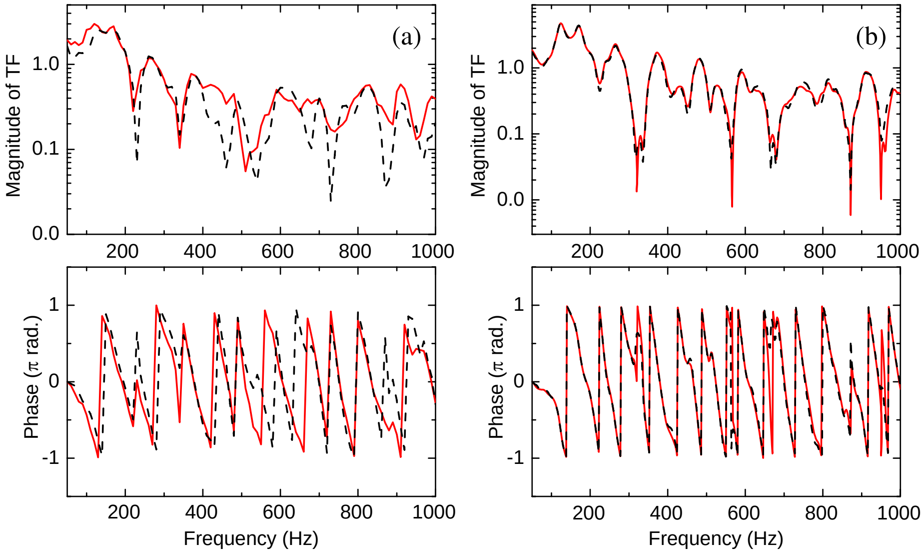

Fig. B.2. Comparisons between the icosahedron source and cubic source. (a) n_s=2 (b) n_s=20. ━━━, Cubic source; – – –, icosahedron source.

Appendix C. CALCULATED ACOUSTIC MEAUSRES

Early decay time (EDT) Early decay time is time taken for the SPL to fall 60 dB over the first 10 dB of the decay (from 0 dB to 10 dB). It is correlated with subjective reverberation during running speech and music. It should be the same as RT in the perfectly diffuse field, but it is smaller than the RT, in general.

Reverberation time (RT, T60, T30, T20) Reverberation time denote the time taken for the SPL to fall 60 dB. RT is the general term including T60, T30, T20, etc. T60 is the time duration of the sound decay from -5 dB to -65 dB. T30 and T20 are the equivalent decaying times of 60 dB calculated from -5 dB to -35 dB and from -5 dB to -25 dB.

Clarity factor (C) The clarity factor (C50, C80), expressed in decibels, is the ratio of the early energy (0-50/80 ms) to the late (reverberant) energy (50/80 ms-∞)the time duration.

$$C_{50} = 10\log\left(\frac{E_{0-50ms}}{E_{50ms-\infty}}\right), C_{80} = 10\log\left(\frac{E_{0-80ms}}{E_{80ms-\infty}}\right) \tag{C.1}$$

Definition, Distinctness (Deutlichkeit) Ratio (D) The definition or distinctness ratio (D) is the ratio of the sound in the first 50 ms after arrival of the direct sound to the total sound arriving. It is usually expressed as a percentage and is determined from the impulse response. It means the early to total sound energy ratio

$$D50 = \frac{\int_0^{50ms} p^2(t)dt}{\int_0^{\infty} p^2(t)dt} \tag{C.2}$$

Center time (Ts) Time of centre of gravity of the squared impulse response.

$$T_s = \frac{\int_0^{\infty} t \cdot p^2(t)dt}{\int_0^{\infty} p^2(t)dt} \tag{C.3}$$

Appendix D. FURTHER STUDY ON THE REFLECTION

A Single Surface

A single surface, which was placed in the anechoic chamber shown in Fig. D.1 was tested. The source and receiver are located at (1.65 m, 2.4 m, 1.5 m) and (3.15 m, 2.4 m, 1.5 m), respectively. Also in this simulation, two approximate reflection coefficients are involved and compared with the measurement data. A good agreement on the frequency response function was found in Fig. D.2 between the PBTM employing complex reflection coefficient and measurement, while the frequency response by the PBTM with real positive reflection coefficient was a bit shifted to the high frequency. The peaks in the magnitude response were originated from the constructive interference between direct sound and reflected sound from the surface. Provided that the material is acoustically hard, there is no phased shift on the reflection at the surface. This assumption enables us to estimate the locations of peak by considering only the difference of two path lengths between the direct and reflected sound. Because the path length difference, Δr, is 1.85 m long, the peaks would occur at the multiples of 185 Hz as shown in blue dotted symbols in case of real reflection coefficient. When the complex reflection coefficient is employed in the calculation, the location of peaks will be changed because of the phase shift on the surface. On the other hand, the phase response is hardly influenced by the reflection coefficient. The steady-state pressure in this case can be expressed as follows:

$$p(\omega) = \frac{p_o}{a_{dir}} e^{\left(-jka_{dir}\right)} + \frac{p_o}{a_{refl}} e^{\left(-jka_{refl}\right)} r\left(\theta\right), \tag{D.1}$$

where p_o denotes the initial pressure (Pa) at the source position and a_{dir} and a_{refl} the traveling distances of direct and reflected sound (m), respectively, and $r(\theta)$ the reflection coefficient for the angle of incidence θ. The resulting pressure consists of the direct pressure and the pressure of the first order reflection. When the distance ratio κ between the reflected path and direct path is introduced, the equation can be changed as follows:

$$p(\omega) = \frac{p_o}{a_{dir}} e^{\left(-jka_{dir}\right)} \left(1 + \frac{1}{\kappa} e^{\left(-jk(\kappa-1)a_{dir}\right)} r\left(\theta\right)\right). \tag{D.2}$$

From the Eq. (D.2), the amplitude and phase angle can be expressed as follows:

$$\left|p(\omega)\right| = \left|\frac{p_o}{a_{dir}}\right| \left|\left(1 + \frac{1}{\kappa} e^{\left(-jk(\kappa-1)a_{dir}\right)} r\left(\theta\right)\right)\right|, \tag{D.3a}$$

$$\angle p(\omega) = \angle e^{\left(-jka_{dir}\right)} + \angle\left(1 + \frac{1}{\kappa} e^{\left(-jk(\kappa-1)a_{dir}\right)} r\left(\theta\right)\right). \tag{D.3b}$$

If the κ goes to infinity, the second term of the amplitude in Eq. (D.3a) becomes unity due to 1/ κ, thus the magnitude is simply converged to the value of $\left|\frac{p_o}{a_{dir}}\right|$. It is obvious that the phase angle becomes $\angle e^{\left(-j\hat{k}a_{dir}\right)}$, as κ increases. In Fig. D.2, the phase spectrum with real reflection coefficient shows identical spectrum with others, while the amplitude shows difference with measurement. The phase angle is composed of two terms; phase angle of the direct sound, $\angle e^{\left(-j\hat{k}a_{dir}\right)}$ and that of reflection, $\angle\left(1 + \frac{1}{\kappa} e^{\left(-j\hat{k}(\kappa-1)a_{dir}\right)} r\left(\theta\right)\right)$. The first term can vary freely from –π to + π. The phase angle of the second term is restricted by the factor of κ and $r(\theta)$. The extreme case is when both $r(\theta)$ and κ are equal to unity, e.g., rigid wall, then the possible maximum and minimum phase angles are ± $\pi/4$, respectively, when $e^{\left(-j\hat{k}(\kappa-1)a_{dir}\right)} = \pm i$. This value is quite smaller than the phase angle of the direct sound. As the $r(\theta)$ decreases or κ increases, the phase angle of the reflected sound becomes smaller. In the other word, the contribution of the first direct term becomes dominant, when the soft wall is involved or the receiver and source are quite far from the surface. Figure D.3 shows the frequency response functions with changing κ. As can be seen in Figs. D.3(b)~ D.3(d), the phase spectra using the real reflection coefficient shows a good agreement with the result using the complex reflection coefficient. Roughly, if the single surface is employed in the simulation, κ value larger than 1.5 can guarantee the accurate phase spectrum using the real reflection coefficient. Thus the suggested region for the real reflection coefficient is out side the ellipse as shown in Fig. D.4.

A comparison of impulse response was displayed in Fig. D.5. The measured impulse response and calculated impulse response using the complex reflection coefficient are almost identical to each other.

A Cubic Box

In this example, one simple cubic shaped room in Fig. D.6 was chosen to compare the transfer function with BEM. The length of the edge is 1.5 *m* and source and receiver are located in (0.3 m, 0.3 m, 0.3 m) and (1.2 m, 1.2 m, 1.2 m), respectively. Normal specific impedance and BEM result are quoted from the Shin's work [83] to compare with the simulation result. Normal specific impedance of the single surface is assumed to 4150+4150*j* (*rayl*). The corresponding absorption coefficient is 0.2 and the Schroeder cutoff frequency of this room was 389 Hz.

Calculated transfer functions are shown in Figs. D.7 and D.8. The PBTM result using the complex reflection coefficient shows a good agreement with that of the BEM, whereas the PBTM using r_θ^d shows a little shifted peak positions and different phase plot. The 1-D simulation was conducted for the model in Fig. D.9. The distance between two parallel infinite panels is 10 m, when the source and receiver is located at (2 m, 0, 0) and (4 m, 0, 0). Then magnitude of the reflection coefficients are fixed to 0.8 and the phase of the reflection coefficient, β, is changed from -45° to 45°, expressed as r=0.8exp($j\beta$). In Fig D.10, the transfer function employing the complex reflection coefficient having 45° phase angle was shifted to the high frequency whereas the transfer function involving negative phase angle was shifted to the low frequency. Figure D.11 shows the trajectory of convergence of pressure in the complex domain when the real reflection coefficient and complex reflection coefficient are involved. Figure D.11(a) shows the convergence of the pressure at 0 Hz for real reflection coefficient. As can be seen, the pressure is decreasing along the real axis. But when the phase angle of the surface impedance becomes positive, the trajectory for the convergence was found in the first quadrant while the trajectory is spiraling in the fourth quadrant for the negative phase angle. This trajectory yields the frequency shift in the transfer function. Because the phase angle of surface impedance in the simple box model is 45° (Z_w=4150+4150j), the transfer function using the real reflection coefficient is shifted to the low frequency range. For most of the porous material, the imaginary part of the impedance changes from negative to positive value (for example, see Fig. 3.6/Figs. 8, 15, 23, 24 in reference [25]). This means that the transfer function at mid frequencies would be shifted to the high frequency when the approximated real reflection coefficient is employed. This result reveals that the frequency shift in the transfer function can be compensated by the average phase of the reflection coefficient in the frequency range of interest.

According to this result, it was proved that if one knows the reflection characteristics of surfaces, the phased geometrical acoustics method can predict the low frequency quite accurately. Similarly to the one-dimensional case in Chapter 2.1, the simple three-dimensional sound field can be analyzed by the particle property, even though there is a scanning error and wave phenomena occurs. It should be reminded that the Schroeder cutoff frequency of this room was 389 Hz. Even the frequency range of interest is much below the Schroeder cutoff frequency, the sound field can be interpreted by the PBTM, provided that the boundary conditions are exactly characterized.

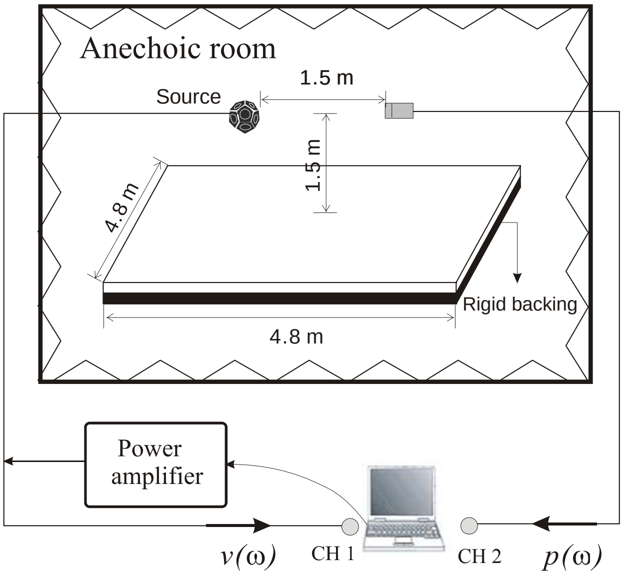

Fig. D.1. A single surface model . A plastic foam patch was located in the semi-anechoic chamber.

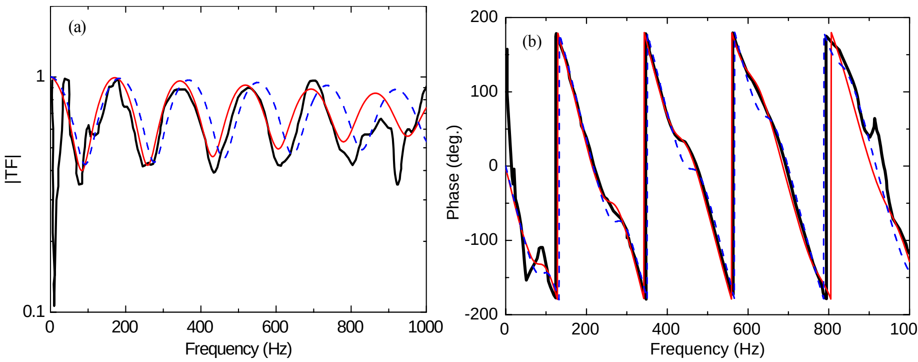

Fig. D.2. A Comparison of measured and calculated FRF at the receiver over the single surface in an anechoic chamber: (a) Magnitude; (b) phase. ▬, Measurement [25]; —, PBTM using complex reflection coefficient; - - -, PBTM using real reflection coefficient.

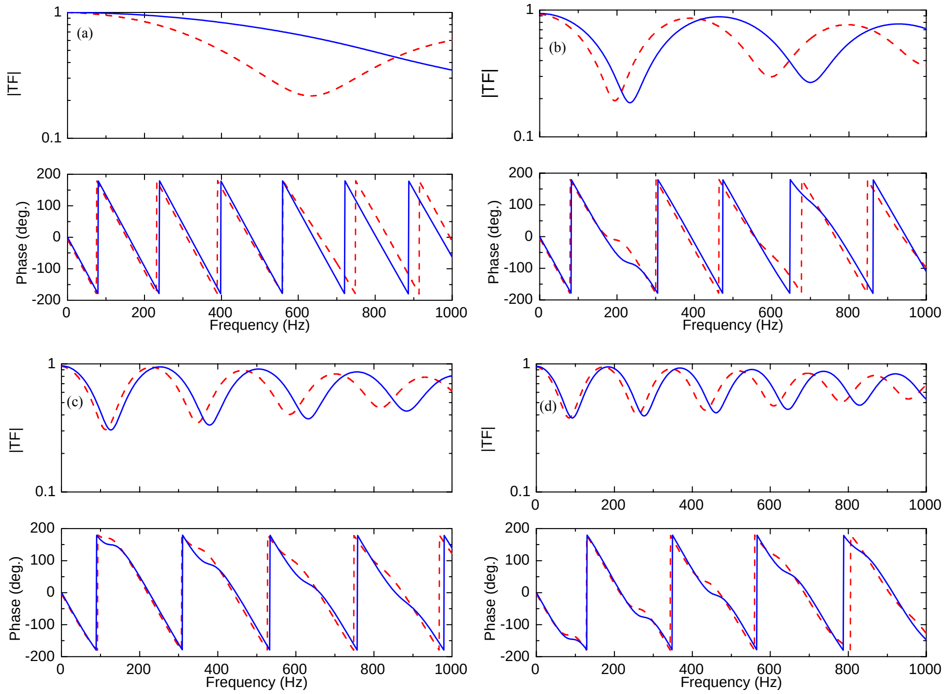

Fig. D.3. Comparisons of FRF varying the distance ratio κ. (a) κ=1.07, (b) κ=1.39, (c) κ=1.84, (d) κ=2.24. - - -, Real reflection coefficient; —, complex reflection coefficient.

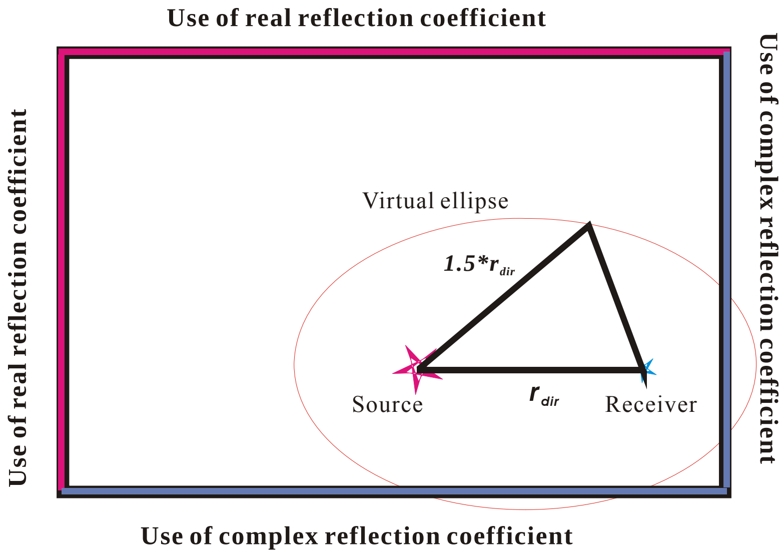

Fig. D.4. Condition for the use of real reflection coefficient. Surfaces outside the virtual ellipse are accepted to assign a real reflection coefficient.

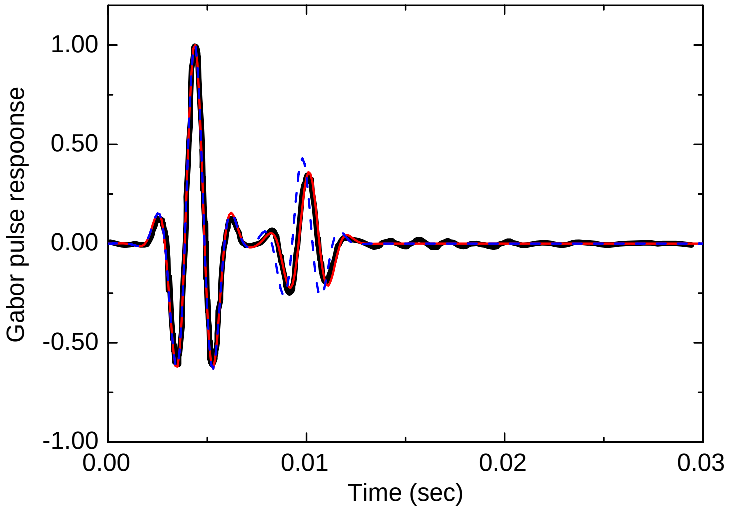

Fig. D.5. Comparison of measured and calculated IR at the receiver over the single surface in an anechoic chamber. ▬▬▬, Measurement [13]; – – –, PBTM using r_d^θ. – – –, PBTM using r_i^θ. Measurement and PBTM employing complex reflection coefficient agree perfectly, so they are overlapped.

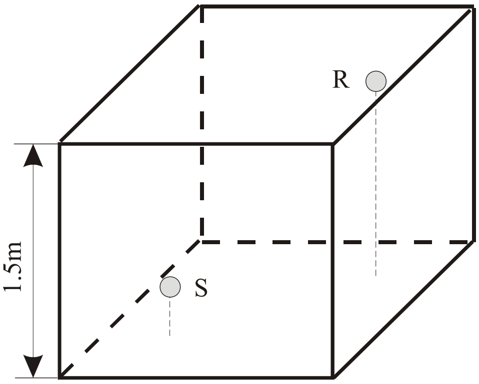

Fig. D.6. Cubic enclosure model for simulating the transfer function by PBTM [83].

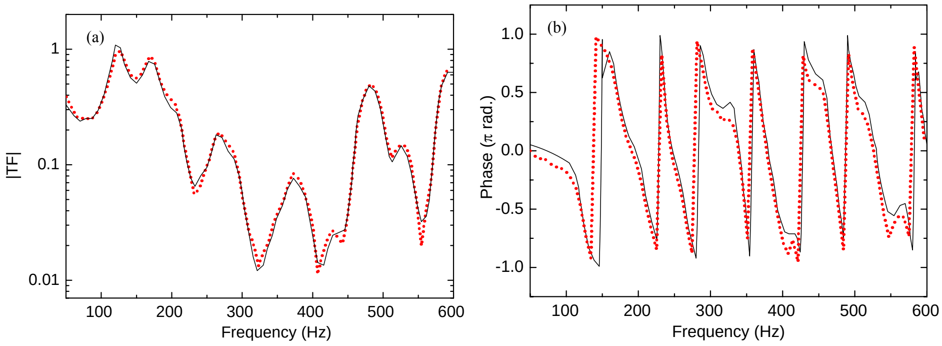

Fig. D.7. A comparison of the TF between source and receiver position. (a) Magnitude, (b) phase. - - - - - PBTM with 8000 beams using complex reflection coefficient; ———, BEM.

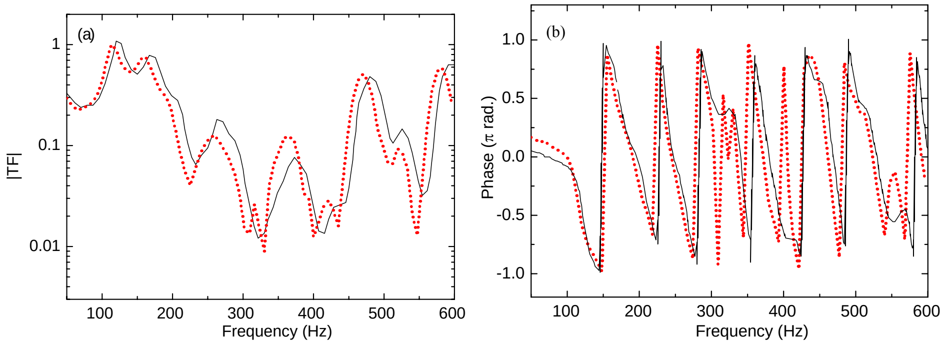

Fig. D.8. A comparison of the TF between source and receiver position. (a) Magnitude, (b) phase. - - - - - PBTM with 8000 beams using r_θ^i; ———, BEM.

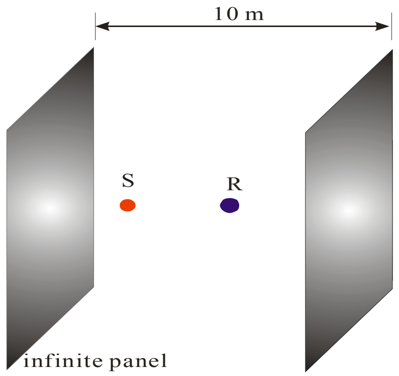

Fig. D.9. 1-D simulation model for the interference between two infinitely large panels.

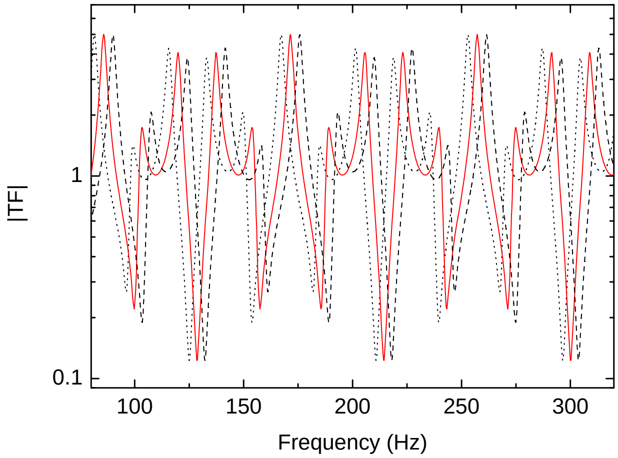

Fig. D.10. A comparison of the magnitude of transfer function employing *r*=0.8exp(*jβ*). ▪ ▪ ▪ ▪ ▪, *β*=–45°; ▬▬▬, *β*=0°; — — —, *β*=45°.

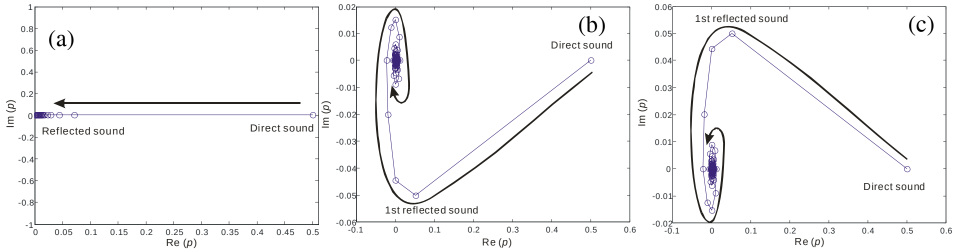

Fig. D.11. Trajectory of convergence in a complex pressure domain. (a) *β*=0°, (b) *β*=-45°, (c) *β*=45°.

SUMMARY IN KOREAN

위상 빔 추적법을 이용한 실내 음향 예측에 있어서 벽면 반사와 회절의 고려

실내 음향 예측 기법인 기하 음향학 방법은 에너지를 변수로 해석하기 때문에 음파의 위상 정보가 중요하지 않은 고주파수 대역이나 큰 공간의 해석에 주로 적용되었다. 반면 저주파수 대역과 작은 공간의 해석은 공간과 시간을 이산화한 후 수치적으로 파동방정식을 풀어내는 음향 유한 요소법, 음향 경계 요소법, 유한 차분법 등이 주로 사용된다. 고주파수 대역에서는 구조의 형상 및 재료의 작은 변화에도 응답이 크게 달라지는 불확실성이 증가하고 모드들이 서로 중첩되므로 각 모드를 정확히 예측하는 파동 기반 방법들은 적절하지 않다. 저주파수와 고주파수 사이의 중주파수 대역의 실내 음향 예측에 있어서 기하 음향학 방법을 기반으로 음파의 파동성을 고려하는 방법이 제안되었으며 이 방법이 바로 위상이 고려된 기하음향학 방법이다. 위상이 고려된 기하 음향학 방법은 기존의 에너지 해석이 아닌 위상을 고려한 음압을 해석하기 때문에 간섭 현상을 모사할 수 있으므로 중저주파수까지 적용 가능하다. 본 논문은 위상이 고려된 기하음향학 방법들 중 하나인 위상 빔 추적법을 이용한 실내 음향 예측에 있어서 벽면의 반사와 회절을 고려한 연구로, 중주파수 해석의 정확성을 높일 수 있는 방법과 저주파수 대역으로 적용 가능성에 대하여 주로 연구되었다.

위상 빔 추적법의 적용시 계산 변수들, 빔의 개수, 반사 횟수, 주파수 분해능, 샘플링 주파수 등의 선정을 연구하였다. 이들 중 가장 중요한 변수는 빔의 개수와 반사 회수, 주파수 분해능으로 빔의 개수와 반사 회수는 빔 추적시 탐색 오차와 관련이 있으며, 주파수 분해능은 공간의 특성 및 음원과 수음점의 위치에 대한 주파수 영역 정보와 관계가 있다. 요구되는 정확성에 따른 계산 변수들의 선정에 대한 연구가 수행되었다.

현재까지 기하 음향학 방법에서 주로 사용되었던 경계면의 흡음률은 주파수 평균된 값이고, 벽면에 충돌한 음파의 에너지 감소만을 나타내므로, 간섭등이 지배적인 중주파수 예측에 적합한 물리량이 아니다. 하지만 모든 벽면에 대하여 표면 임피던스와 같은 음향 특성을 측정하는 것은 불가능하므로 실용적인 음압 반사 계수가 필요하다. Rindel에 의해 제안된 입사각 종속 반사 계수는 기존의 입사각 독립 반사 계수에 비하여 중주파수 음파의 거동을 잘 나타낼수 있으며, 실제 방에 적용한 결과 측정치와 잘

일치하였다. 입사각 종속 반사 계수는 음의 실수값을 가질 수 있으므로 음파의 상쇠 간섭을 설명할수 있는 장점이 있으며, 이러한 음의 실수값을 가지는 조건에 대하여 연구되었다. 음압 반사 계수를 이용하여 음압 충격 응답, 주파수 응답 함수, 그리고 공간의 음질을 평가할수 있는 객관적인 음질 계수들이 계산되었다. 객관적인 음질 평가 방법과 더불어 실제 공간에 사람이 위치하였을 때 음악 및 소리가 어떻게 들리는지를 미리 들어볼수 있는 새로운 가청화 방법이 제안되었다. 기존의 가청화 방법은 시간영역에서 음의 도달시간과 그 시간에서의 에너지 정보를 랜덤 위상을 가정하여 예측하는 반면, 제안된 방법은 주파수 영역에서 머리 전달 함수와 대합 (convolution)이 빠르며 각 반사의 위상을 정확히 고려할 수 있는 장점을 가지고 있다. KAIST의 세미나실에 대한 예측 결과는 실험 결과와 잘 일치하며 이 기법은 향후 모든 위상 기하 음향학 방법에 대하여 적용될 수 있다.

위상 빔 추적법은 직진하는 빔을 이용하여 공간을 탐색하기 때문에 회절 현상을 고려하지 못하는 단점이 있다. 본 연구에서는 기하 회절 이론의 한 방법인 균일 회절 이론을 적용하여 회절을 고려한 위상 빔 추적법을 개발하였다. 균일 회절 이론은 다른 회절 이론들과 비교하여 빠르고 날카로운 모서리에서도 정확하며, 불연속적인 반사 및 그늘 경계면에서도 발산하지 않는다. 이러한 균일 회절 이론을 위상 빔 추적법에 병합하여 평면파/구형파에 대한 계단 모형과 회절 모서리가 있는 방을 공간 영역과 시간 영역에서 해석하였다. 공간과 시간 영역의 모의 실험 결과에서 기존의 문제점이었던 음압의 불연속 문제가 보정되었으며, 무향실에서의 실험 결과와 잘 일치하였다. 최종적으로 실제 존재하는 콘서트홀을 예측한 결과와 실험 결과를 비교하였다.

위상 빔 추적법은 음파의 입자성을 강조한 기하 음향학을 기반으로 하여 소리의 파동성을 고려한 방법으로, 소리의 파동성만을 고려한 경계 요소법과 중-저주파수에서 결과가 잘 일치한다. 이는 소리의 이중성, 즉 입자성과 파동성 어느 성질을 이용하더라도 소리의 거동에 대하여 같은 결과를 도출할 수 있다는 것을 의미하며, 입자성을 강조하는 위상 빔 추적법을 이용하여 중-저주파수 해석도 가능함을 암시하고 있다. 이러한 위상 기하음향학 방법을 이용하여 적절한 접근 방법이 부재한 중주파수 대역을 빠르고 정확하게 해석할 수 있으며, 고주파수와 큰 공간의 실내 음향의 해석뿐만 아니라 차나 비행기의 실내 내부와 같은 작은 공간에 대하여 위상 기하 음향학 방법을 적용하여 해석할 수 있다.

CURRICULUM VITAE

PERSONAL INFORMATION

Name	Cheol-Ho Jeong (정철호; 鄭哲浩)
Date/Place of Birth	February 15, 1979 / Jeonju, Korea
Sex/Age	Male / 28 Years
Marriage/Family	Single
Nationality	Korea

MAJOR FIELD AND CURRENT RESEARCH INTERESTS

Major Field	Acoustics (Noise and Vibration Control)
Research Interests	Structural Acoustics Theoretical and Experimental Modeling of Vibro-acoustic Fields and Sources Architectural Acoustics Room Acoustics

EDUCATION

Mar. 2002 - Aug. 2007	Ph. D. in Mechanical Engineering, Korea Advanced Institute of Science and Technology (KAIST), Daejeon, Korea; Professor Jeong-Guon Ih, Advisor; Professor Jens H. Rindel, Co-advisor; Thesis Title = "*Consideration of Wall Reflection and Diffraction in the Room Acoustic Prediction Using the Phased Beam Tracing Method*"
Mar. 2000 - Feb. 2002	M.S. in Mechanical Engineering, Korea Advanced Institute of Science and Technology (KAIST), Daejeon, Korea; Professor Jeong-Guon Ih, Advisor; Thesis Title = "*A Study on the High Frequency Vibration Analysis of Curved Beam Structures by Using the Ray Tracing Method*"
Mar. 1996 - Feb. 2000	B.S. in Mechanical Engineering, Korea Advanced Institute of Science and Technology (KAIST), Korea.

EMPLOYMENT

July 1996 - August 1996

Internship Program, CAE Center, Samsung Advanced Institute of Technology (SAIT), Kiheung, Korea.

March 2002 ~ December 2005

Educational Assistant in the Department of Mechanical Engineering, Korea Advanced Institute of Science and Technology (KAIST), Daejeon, Korea.

2002. Spring semester: Applied Electronics
2002. Fall semester: Applied Electronics
2003. Spring semester: Mechanical Vibration
2003. Fall semester: Regular Seminar for Mechanical Engineers
2004. Spring semester: Random Data
2004. Fall semester: Assistant in the Department Office
2005. Spring semester: Guest Researcher in DTU
2005. Fall semester: Noise Control

December 2004 ~ June 2005

Guest researcher in Acoustic Technology, Oersted/DTU, Technical University of Denmark, Denmark.

AWARDS

(1) *Best Thesis Award in Mechanical Engineering*, Department of Mechanical Engineering, KAIST, February 15, 2002. (Valedictorian; An Honor Graduate)

(2) *Best Presentation Award in the meeting of Acoustical Society of Korea*, 2003. Paper title = "*Evaluation of Coupling Loss Factors for the Scale Model of KOMPSAT-II* "

(3) *Best Presentation Award in the meeting of Acoustical Society of Korea*, 2005. Paper title = "*Phased Beam Tracing Method Using the Reflection Coefficient Calculated from the Absorption Coefficient*"

(4) *Best Presentation Award in the meeting of Acoustical Society of Korea*, 2007. Paper title = "*Errors in the Low to Mid Frequency Prediction Using the Phased*

Beam Tracing Method"

(5) *ICA-ASA Young Scientist Grant, International Commission for Acoustics,* 2007. Paper title = "*Introduction and Applications of Phased Beam Tracing Method: Can We Interpret Low Frequency Response by the Particle Property?*"

PUBLICATION

A. Thesis

A1. M. S. THESIS: A Study on the High Frequency Vibration Analysis of Curved Beam Structures by Using the Ray Tracing Method, February 2002, KAIST, Korea.

A2. Ph. D. THESIS: Consideration of Wall Reflection and Diffraction in the Room Acoustic Prediction Using the Phased Beam Tracing Method, August 2007, KAIST, Korea.

B. International Journals: (국제전문학술지)

B1. C.-H. Jeong, J.-G. Ih, J. H. Rindel, "An Approximate Treatment of Reflection coefficient in the Phased Beam Tracing Method for the Simulation of Enclosed Sound Fields at Medium Frequencies," Accepted for publication in Applied Acoustics 2007.

B2. C.-H. Jeong, J.-G. Ih, "A Note on the Proper Frequency Resolution for the reverberation time of the room transfer function," Submitted to Applied Acoustics 2007.

C. Domestic Journals: (국내 전문 학술지)

C1. C.-H. Jeong, J.-G. Ih, C.-H. Yeon and C.-H. Haan, "Prediction of the Acoustic Performance of a Music Hall Considering the Radiation Characteristics of Korean Traditional Music Sources (국악 음원의 방사특성을 고려한 국악원의 음향 성능 예측)," Journal of the Acoustical Society of Korea (한국음향학회지), vol.23, no.2, pp.146-161, February 2004, Seoul.

C2. C.-H. Haan, W. Lee and C.-H. Jeong "Investigation of the Acoustic Performance of Music Halls Using Measured Radiation Characteristics of the Korean Traditional Musical Instruments (국악기의 음향 방사

특성에 따른 국악당의 음향 성능 조사)," Journal of the Acoustical Society of Korea (한국음향학회지), vol. 24, no.8, pp.469-480, November 2005, Seoul.

D. International Conferences: (국제전문학술회의발표)

D1. C.-H. Jeong and J.-G. Ih, "High Frequency Vibration Analysis of Curved Beam Structures by Using the Ray Tracing Method," Proc. of the 8th RASD, CD-ROM, July 2003, Southampton, UK.

D2. C.-H. Jeong, J.-G. Ih, C.-H. Yeon, and C.-H. Haan, "Modeling of Sound Fields Considering the Acoustical Characteristics of Korean Traditional Musical Instruments," Proc. of the Inter-Noise 2003, CD-ROM, August 2003, Seogwipo, Korea.

D3. C.-H. Jeong and J.-G. Ih, "Effect of Modal Overlap Factor on the Ray Tracing Analysis of the Curved Beam Structure," Proc. of the 146th ASA Meeting, October 2003, Austin, USA.

D4. J.-G. Ih, C.-H. Jeong and J. H. Rindel, "A Study on the Phased Beam Tracing Technique for the Acoustic Simulation of an Enclosure," Proc. of the ASJ Joint Meeting of Architectural Acoustics and Musical Acoustics, February 2006, Hamamatsu, Japan (Invited).

D5. C.-H. Jeong, J.-G. Ih and J. H. Rindel, "A Study on the Characteristics of Phased Beam Tracing Method for the Acoustic Simulation of an Enclosure at Mid Frequencies," Proc. of the WESPAC IX, June 2006, Seoul, Korea (Invited).

D6. C.-H. Jeong and J.-G. Ih, "Binaural simulation in an enclosure using the phased beam tracing," Proc. of the 4th Joint Meeting of the Acoustical Society of America and the Acoustical Society of Japan, December 2006, Honolulu, USA.

D7. C.-H. Jeong, W.-H. Cho, J.-G. Ih, S.-H. Shin and J.-K. Ryoo, "Objective evaluation of engine noise quality with the change of engine oil" Proc. of the Inter-Noise 2006, December 2006, Honolulu, USA.

D8. C.-H. Jeong, J.-G. Ih, "Implementation of the Uniform Theory of Diffraction in the Phased Beam Tracing Method" Proc. of the ICSV14, July 2007, Cairns, Australia.

D9. C.-H. Jeong, J.-G. Ih, "Introduction and Applications of Phased Beam Tracing Method: Can We Interpret Low Frequency Response by the Particle Property?" Proc. of the ICA 2007, September 2007, Madrid, Spain.

D10. J.-G. Ih, S.-W. Jang, C.-H. Jeong, "A Study on the Sound Quality Evaluation Model of the Air Cleaner" Proc. of the ASME, IMECE, November 2007, Seattle, USA.

E. Domestic Conferences: (국내전문학술회의발표)

E1. C.-H. Jeong and J.-G. Ih, “High frequency vibration analysis of single curved beam using the ray tracing method (레이 추적 기법을 이용한 단일 곡보의 고주파수 진동 해석),” Proc. of the Autumn Meeting of the KSNVE, pp.90-95, November 2001, Yongpyong.

E2. C.-H. Jeong and J.-G. Ih, "High Frequency Vibration Analysis of Connected Curved Beam Structures (음선 추적에 의한 연결된 곡보 구조의 고주파수 진동해석)," Proc. of the Summer Meeting of the ASK, pp.477-480, July 2002, Changwon.

E3. C.-H. Jeong, J.-G. Ih, S.-M. Moon, and H.-B. Kim, “Vibro-acoustic Analysis of Simplified Satellite Model by Using the Statistical Energy Analysis Technique (단순화된 위성체의 통계적 에너지 해석법을 이용한 음향-진동 연성 해석),” Proc. of the Autumn Meeting of the KSNVE, CD-Rom, Nov. 2002, Seoul.

E4. S.-H. Shin, C.-H. Jeong, J.-G. Ih, C.-H. Yeon, and C.-H. Haan, "A Study on the Radiation Characteristics of Korean Traditional Musical Sources (국악 음원의 음향 방사 특성에 관한 연구)," Proc. of the Summer Meeting of the ASK, pp.489-492, July 2003, Mokpo.

E5. C.-H. Jeong, J.-G. Ih, and H.-B. Kim, "Evaluation of Coupling Loss Factors for the Scale Model of KOMPSAT-II (KOMPSAT-II Scale 모델의 실험적 연성 손실 인자 산출)," Proc. of the Autumn Meeting of the ASK, pp.239-242, October 2003, Kyoungju. (*Best Presentation Award Winner*)

E6. C.-H. Jeong, Y.-I. Kwon, S.-H.Shin and J.-G. Ih, "A Comparison between Predicted and Measured Acoustic Characteristics of Jeonmin Catholic

Church (전민동 성당의 음향 특성에 관한 모의 실험 및 측정 결과 비교)," Proc. of the Spring Meeting of the ASK, pp.241-244, May 2004, Tongyoung.

E7. C.-H. Jeong, H.-W. Chang, J.-G. Ih, C.-H. Yeon and C.-H. Haan, "An Experimental Study on the Radiation Characteristics of the Korean Traditional Musical Instruments (국악기의 음향 방사 특성 조사 연구)," Proc. of the Autumn Meeting of the ASK, pp. 551-554, November 2004, Hoingseong.

E8. C.-H. Jeong, J.-G. Ih, Y.-K. Kim and H.-B. Kim "An Application Example of SEA for KOMPSAT-1 Satellite Model (KOMPSAT-1 위성구조체에 대한SEA 적용사례 및 측정 결과 비교)," Proc. of the Autumn Meeting of the ASK, pp. 211-214, November 2004, Hoingseong.

E9. C.-H. Jeong, J.-G. Ih and J. H. Rindel "Phased Beam Tracing Method Using the Reflection Coefficient Calculated from the Absorption Coefficient (흡음계수로부터 계산된 반사 계수를 이용한 위상이 고려된 빔 추적법)," Proc. of the Autumn Meeting of the ASK, pp. 325-328, November 2005, Hoingseong. (*Best Presentation Award Winner*)

E10. C.-H. Jeong and J.-G. Ih "On the proper selection of frequency resolution of the room transfer function by using the phased beam tracing method (위상이 고려된 빔 추적법을 이용한 실내전달함수의 주파수 분해능 선정에 관하여)," Proc. of the Autumn Meeting of the ASK, pp. 421-424, November 2006, Daegu.

E11. C.-H. Jeong, S-I. Kim, J.-G. Ih, E.-J. Hong, W.-S. Kim and H.-S. Lee "Vibro-acoustic analysis for the reduction of HDD noise (HDD 소음 저감을 위한 음향/진동 분석)," Proc. of the Autumn Meeting of the KSNVE, CD-ROM, November 2006, Hwasoon.

E12. C.-H. Jeong, J.-G. Ih "Errors in the Low to Mid Frequency Prediction by Using the Phased Beam Tracing Method (위상이 고려된 빔 추적법을 이용한 중저주파수 예측의 오차)," Proc. of the Spring Meeting of the ASK, pp. 215-218, May 2007, Seoul. (*Best Presentation Award Winner*)